

Contents

1	What controls the initiation and development of non-precipitating shallow cumulus clouds in an idealised model framework?	2
1.1	Generating shallow convective clouds in LES using localised surface fluxes	2
1.1.1	Motivation	2
1.1.2	Choosing localised flux parameters	4
1.1.3	Results - Single_C	5
1.1.4	Flux sensitivities	8
1.1.5	Multi Flux - Experimental Design	13
1.1.6	Results - Multi_REF	15
1.1.7	Summary	32
1.2	Below cloud: Boundary-layer controls on convective cloud development	33
1.2.1	Motivation	33
1.2.2	Method	37
1.2.3	Results	40
1.2.4	Conclusions	69
1.3	Above cloud: The effect of convectively-generated gravity waves on cloud initiation and development	70
1.3.1	Motivation	70
1.3.2	Visualisation of gravity waves	71
1.3.3	Wave period	74
1.3.4	Convectively generated waves	77
1.3.5	Gravity wave phase controls on cloud development	78
1.3.6	Further analysis using idealised LES simulations	86
1.3.7	Discussion	86
	Bibliography	87

Chapter 1

What controls the initiation and development of non-precipitating shallow cumulus clouds in an idealised model framework?

1.1 Generating shallow convective clouds in LES using localised surface fluxes

1.1.1 Motivation

The previous chapter explored the process of using homogeneous surface heat fluxes to produce a large population of convective clouds. This chapter will use heterogeneous surface fluxes to produce shallow convective clouds in isolation, whose dynamics and interactions with neighbouring clouds are easier to analyse. These heterogeneous or ‘localised’ surface fluxes are defined in such a way as to approximately reproduce the main properties of representative cloud C_{hom} from the previous chapter. The behaviour of clouds resulting from multiple localised surface fluxes is then compared, investigating their interactions with the atmospheric boundary layer, the free environment and each other.

Heterogeneous surface fluxes have been used in LES studies in many previous studies to produce convective clouds (e.g. van Heerwaarden and Guerau de Arellano, 2008; Kang and Bryan, 2011; Rieck et al., 2014). The size and amplitude of these fluxes influence the development of the convective boundary layer (CBL) and, in turn, cloud initiation and development. For example, Kang and Bryan

(2011) demonstrated that convective clouds initiate earlier as the amplitude of the surface flux increases, or as a surface becomes wetter. van Heerwaarden and Guerau de Arellano (2008) showed that warmer surface patches are favourable for cloud formation, and that resulting thermals are more able to penetrate inversions than thermals generated by homogeneous surface fluxes. Rieck et al. (2014) showed that the size of convective clouds scales with the size of the localised flux, rather than the boundary layer height.

Previous studies have demonstrated the impact of localised surface fluxes on the thermodynamic variation within the CBL. For example, Kang and Bryan (2011) showed that heterogeneous surface fluxes result in a wider distribution of boundary layer height and lifting condensation level. van Heerwaarden and Guerau de Arellano (2008) demonstrated that warm surface patches resulted in higher time-averaged relative humidity values at the top of the CBL compared to using homogeneous fluxes.

Multiple studies have found that heterogeneous surface forcing results in the formation of organised meso-scale circulations in the CBL (e.g. Kang and Bryan, 2011; Patton et al., 2005; Rieck et al., 2014). Additionally, Patton et al. (2005) discovered that the scale and dynamics of such circulations depend on the relative size of the surface heterogeneity to the boundary layer height. These meso-scale circulations are important for advecting moisture through the boundary layer (van Heerwaarden and Guerau de Arellano, 2008), as well as providing localised regions of increased vertical velocity where the outflow of multiple circulations collide which leads to accelerated cloud development (Rieck et al., 2014).

Heterogeneous surface fluxes and localised variations in CBL thermodynamic properties are known to influence cloud initiation. For example, as the amplitude of heterogeneous surface forcing increases, convection initiation occurs sooner (Kang and Bryan, 2011). Kang and Bryan (2011) also discovered that relatively wet surfaces increase the boundary layer buoyancy and result in more energetic eddies, which produce convective clouds earlier than over comparatively dry surfaces. van Heerwaarden and Guerau de Arellano (2008) found that warm surface patches aid in cloud formation by inducing mesoscale circulations which advect moisture directly over the warm patch and increase the relative humidity. Hirsch et al. (2017) found that variation in CBL humidity, generated through turbulence and convection, can influence cloud initiation - they showed that convective clouds may initiate even in situations where the predicted lifting condensation level is significantly higher than the base of the atmospheric inversion, due to pockets of high relative humidity air near the middle of the boundary layer.

Rieck et al. (2014) demonstrated that the transition from shallow to deep convection and the onset of precipitation is accelerated over heterogeneous surfaces. This is caused by the advection of moisture via boundary layer meso-scale circulations, which act to invigorate convection as a result of increased buoyancy. They also noted that while previous research suggests that the size of convective clouds over homogeneous surfaces scales with the height of the CBL, the same is not true over clouds forming over heterogeneous surfaces. Rieck et al. (2014) demonstrated that the ability of convective clouds to grow deeper is enhanced in environments with heterogeneous, rather than homogeneous, surface fluxes.

Chapter overview

The structure of this chapter is as follows. Section 1.1.2 outlines the methodology by which the localised flux parameters of radius, amplitude and duration are chosen. Section 1.1.3 presents preliminary results, and fine-tunes the flux parameters based upon these. Section 1.1.4 explores the sensitivity of cloud development to these three flux parameters. The chapter then proceeds to the multi-flux simulation Multi_REF. Section 1.1.5 outlines the experimental design, and Section 1.1.6 presents the results. The results are split into three sections: general cloud evolution (in terms of average cloud properties); average profiles, conditionally sampled over the cloud core, shell and environment; and in-cloud thermodynamic and kinematic variability. Note that a comprehensive description of all model runs can be found in Table ??, Appendix A.

1.1.2 Choosing localised flux parameters

The experimental design here is almost identical to that described in Section ??, with the exception of the domain size which is reduced to 4km in all directions. At the end of the spinup period, localised circular sensible and latent heat fluxes are applied at the surface to produce a single localised cloud ‘ C_{loc} ’, while the background sensible heat flux of 50 Wm^{-2} continues outside of this area. The localised surface fluxes are centered at $x = 2\text{km}$ and $y = 2\text{km}$ at the centre of the domain. The method for specifying an appropriate flux radius, amplitude and duration is outlined here.

Since the moist static energy transport of C_{hom} is $2.6 \times 10^{11} \text{ J}$, the moist static energy of C_{loc} should approximately equal this value. Mathematically, the moist static energy transport E_T of the localised flux is defined as

$$E_T = A \times M \times D, \quad (1.1)$$

where A is flux area in m^2 , M is the flux amplitude in W m^{-2} and D is the flux duration in seconds. Both the sensible and latent heat flux amplitudes are set equal to 200 W m^{-2} as before, which leaves the area and duration of the fluxes as unknowns.

The average cloud base area a of C_{hom} is 82784 m^2 ; however, this does not take into account the fact that heat fluxes from outside this area also feed into the cloud base of C_{hom} .

A representative flux area a^* is found by dividing a by the domain-average cloud-base cloud core fraction from the homogeneous heat flux simulation, which has a value of 0.2. The equation $a^* = \pi r^2$, where r is the radius of a circle, then yields

$$\pi r^2 = \frac{82784}{0.2}. \quad (1.2)$$

The radii of the localised fluxes (r) should therefore equal approximately 363m. For simplicity, this is rounded down to 350m, which gives an area of $\approx 3.8 \times 10^5 \text{ m}^2$. Substituting the values for flux area and amplitude into Equation 1.1 indicates that the fluxes should be prescribed for a total of 28 minutes in order to transport a comparative amount of moist static energy as C_{hom} .

1.1.3 Results - Single_C

Figure 1.1 shows the evolution of cloud C_{hom} (black, dashed line) versus the cloud resulting from the localised flux described in Section 1.1.2 ('First Guess', faded coloured lines). The localised cloud forms earlier and persists longer than C_{hom} , as well as exhibiting a significantly larger liquid water content. The evolution of the localised cloud would be expected to approximately match that of C_{hom} if the following conditions were all true:

1. C_{hom} experienced no interaction with the surrounding ensemble of clouds;
2. C_{hom} did not modify the environment in any significant way, so that C_{loc} encounters the same environmental conditions as C_{hom} ;
3. The evolution of both boundary layers are identical.

In reality, at least one of these conditions has proved to be false, resulting in the significantly different evolution of C_{hom} and the localised cloud. It is not particularly important to perfectly replicate C_{hom} using localised fluxes, rather it is desirable to approximately replicate its behaviour and energy transport. The localised fluxes are therefore modified to produce a cloud that more closely resembles C_{hom} . The final parameters for the localised heat fluxes are then

- Location: $x = 2\text{km}$, $y = 2\text{km}$, $z = 0\text{km}$
- Radius: 350m
- Amplitude: $\text{SHF} = \text{LHF} = 200 \text{ Wm}^{-2}$
- Duration: 600s.

This simulation is henceforth referred to as simulation Single_C, where C denotes the fact that the fluxes are located in the centre of the domain. After the localised fluxes have run for 10 minutes, the surface fluxes reduce back to their background values of $\text{SHF} = 50 \text{ Wm}^{-2}$ and $\text{LHF} = 0 \text{ Wm}^{-2}$. The evolution of the final cloud C_{loc} is given by the solid coloured lines in Figure 1.1, which is shown to resemble C_{hom} much more closely than before. These localised fluxes provide a total $E_T = 9.2 \times 10^{10} \text{ J}$.

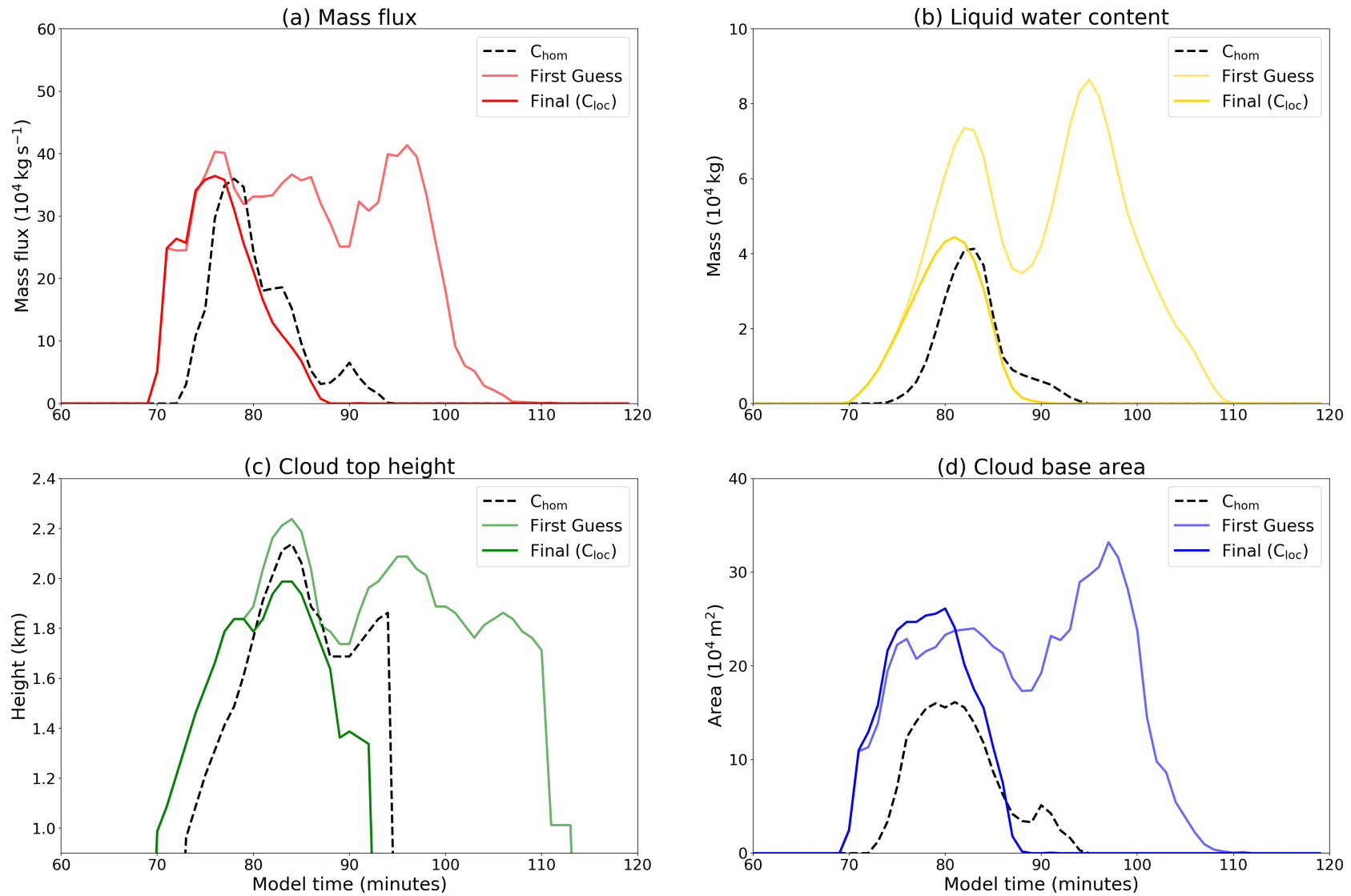


Figure 1.1: Timeseries of (a) cloud base mass flux (in kg s^{-1}), (b) total liquid water (in kg), (c) cloud top height (in km), and (d) cloud base area (in m^2) for: C_{hom} (black dashed line), first attempt at a localised cloud (faded coloured lines) and final localised cloud C_{loc} (solid coloured lines).

Figure 1.2(a) shows the vertical structure of C_{loc} at 80 minutes, the approximate time of maximum cloud base mass flux. The cloud structure is asymmetrical due to the turbulent boundary layer, and the highest values of liquid water (around 1 g kg^{-1}) are present near the cloud top. Figure 1.2(b) shows the corresponding time frame of liquid water path, which provides a visual of C_{loc} 's horizontal structure. The liquid water path of C_{loc} is much greater than the surrounding shallow clouds, and shows that the cloud is approximately 1km wide.

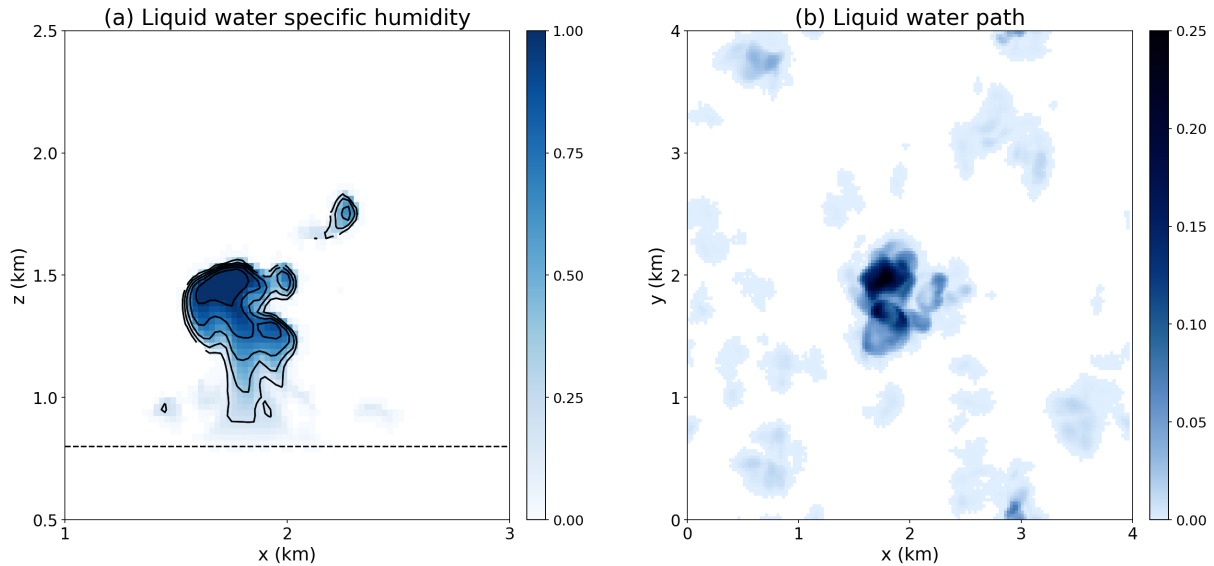


Figure 1.2: Results from the *Single_C* simulation taken at 80 minutes. Panel (a) is a vertical cross-section through $y = 2 \text{ km}$, showing liquid water specific humidity in g kg^{-1} ; contours are shown every 0.2 g kg^{-1} . The black solid line at the surface indicates the position of the localised surface fluxes from ten minutes prior, and the horizontal black dashed line is the level of cloud base. Panel (b) is the liquid water path in kg m^{-2} .

1.1.4 Flux sensitivities

With the parameters for a localised heat flux finalised, it is useful to know the effect of systematically varying the radius r , amplitude m and duration d of these heat fluxes on cloud development. Each parameter is adjusted by $\pm 20\%$ to give the following (bold indicates original flux values):

- Radius: $r = 280, \mathbf{350}, 420 \text{ m}$
- Amplitude: $m = 160, \mathbf{200}, 240 \text{ W m}^{-2}$
- Duration: $d = 480, \mathbf{600}, 720 \text{ s.}$

Figures 1.3, 1.4 and 1.5 show the variation in cloud properties with varying flux radius, amplitude and duration.

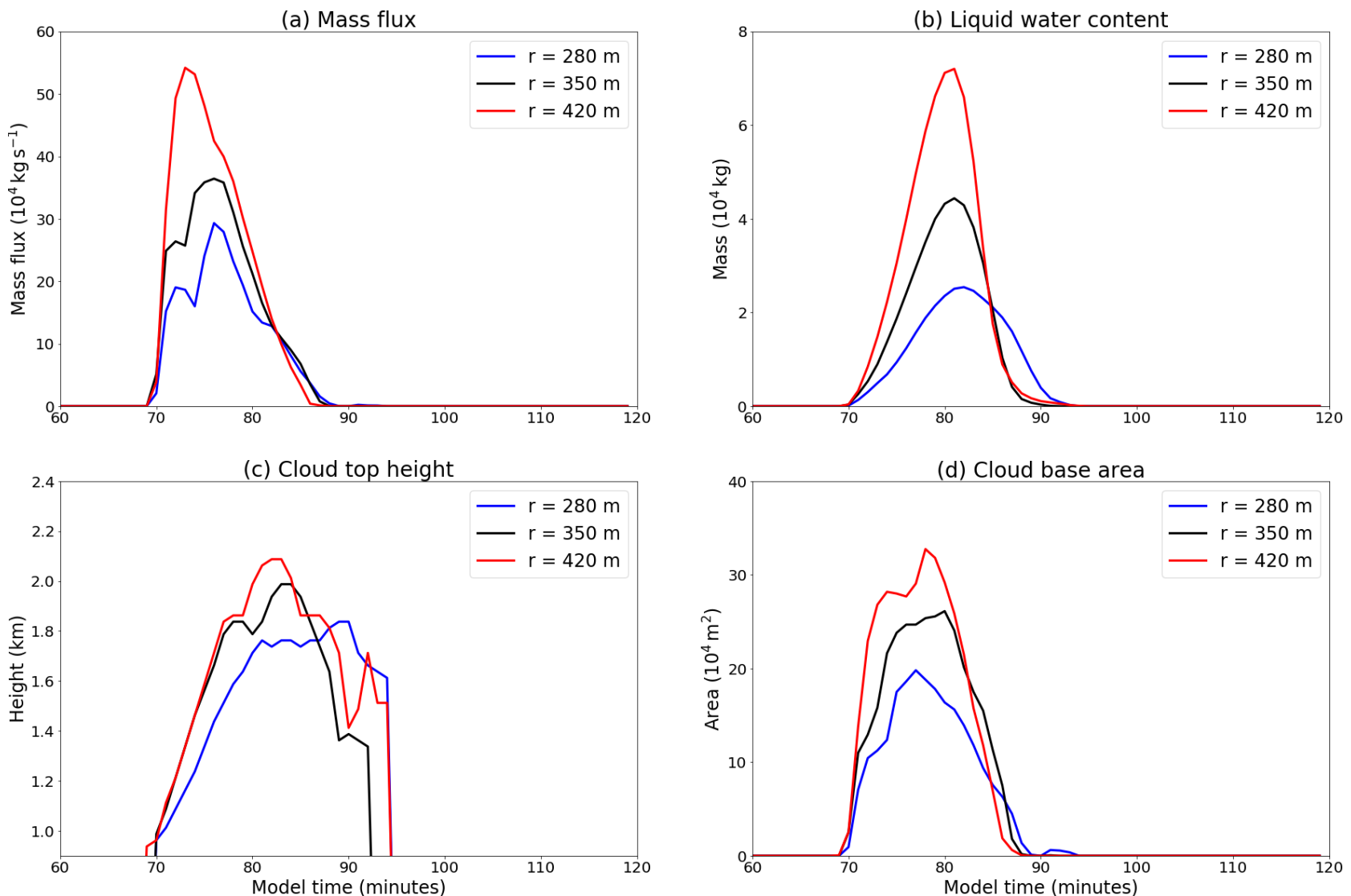


Figure 1.3: Sensitivity of cloud evolution to varying flux radius. Figure shows timeseries of (a) cloud base mass flux (in kg s^{-1}), (b) total liquid water (in kg), (c) cloud top height (in km) and (d) cloud base area (in m^2). The default curves for C_{loc} are shown as black lines, while an increase/decrease in flux radius are shown as red/blue lines respectively.

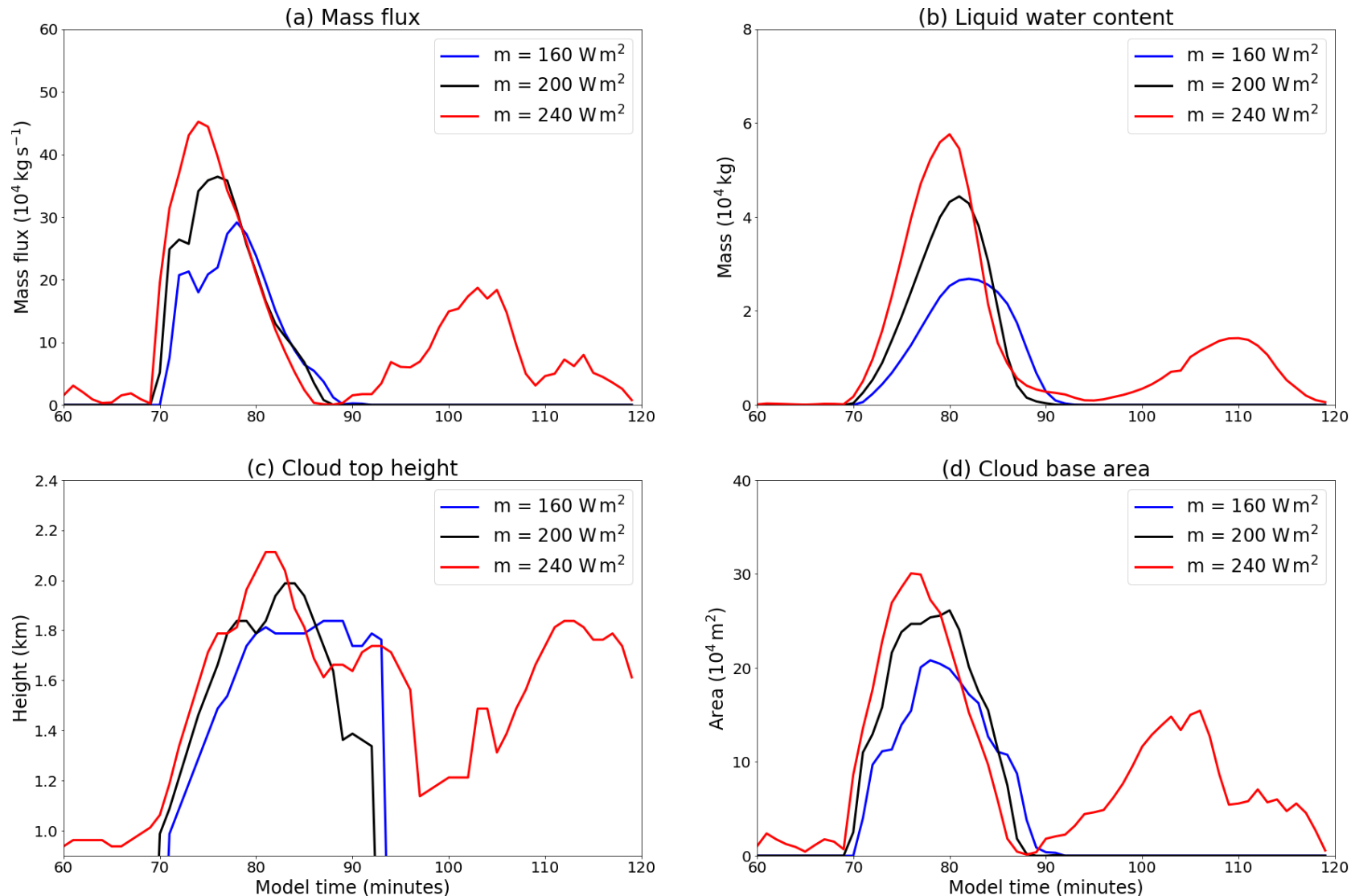


Figure 1.4: Sensitivity of cloud evolution to varying flux amplitude. Figure shows timeseries of (a) cloud base mass flux (in kg s^{-1}), (b) total liquid water (in kg), (c) cloud top height (in km) and (d) cloud base area (in m^2). The default curves for C_{loc} are shown as black lines, while an increase/decrease in flux intensity are shown as red/blue lines respectively.

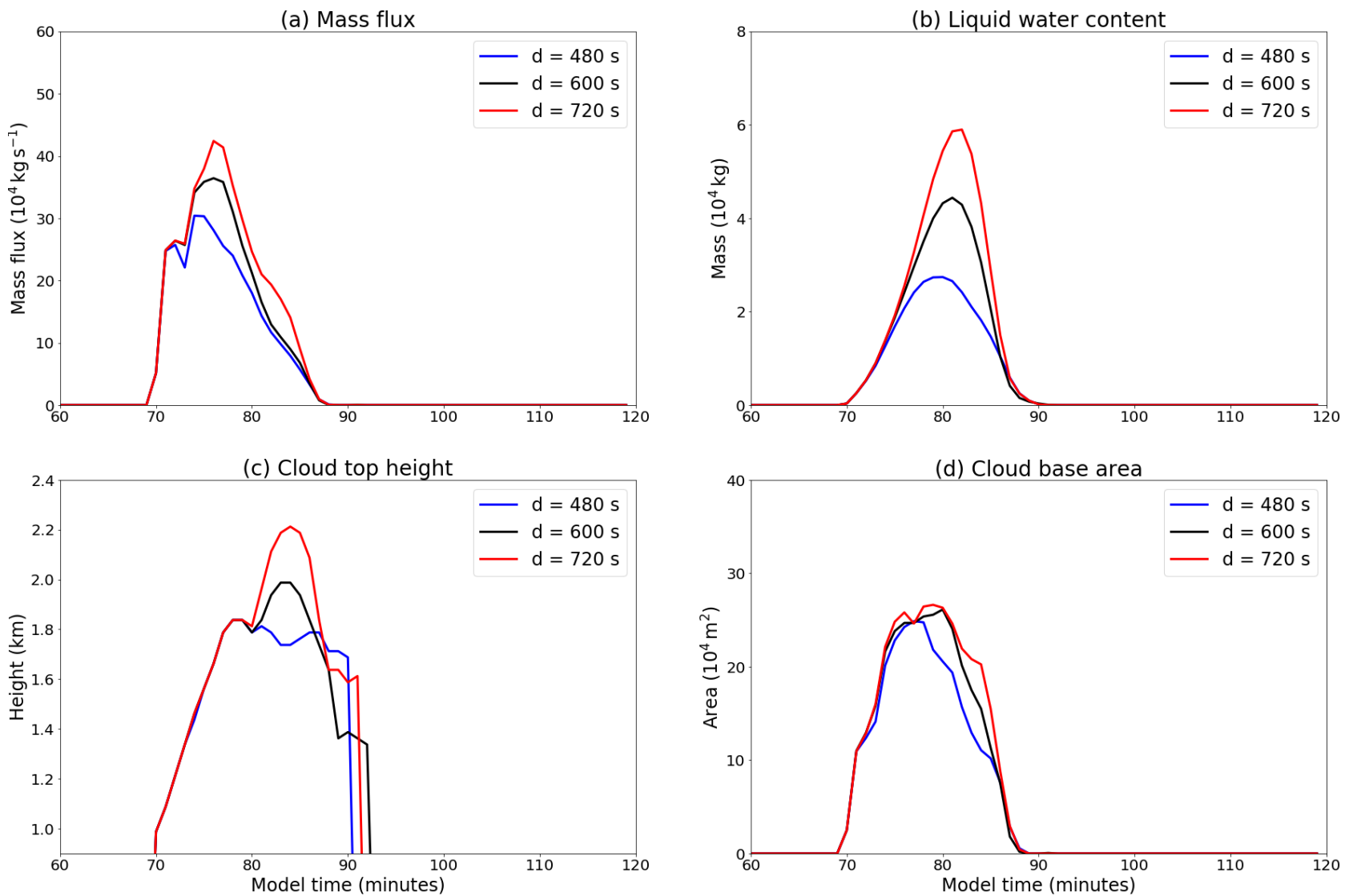


Figure 1.5: Sensitivity of cloud evolution to varying flux duration. Figure shows timeseries of (a) cloud base mass flux (in kg s^{-1}), (b) total liquid water (in kg), (c) cloud top height (in km) and (d) maximum cloud base area (in m^2). The default curves for C_{loc} are shown as black lines, while an increase/decrease in flux duration are shown as red/blue lines respectively.

Figure 1.3 shows that larger flux radii results in wider and deeper clouds that transport more mass. This can partly be explained by the fact that the entrainment rate of wider clouds is slower than narrower clouds, therefore protecting the cloud core from erosion for a longer time and allowing the cloud to grow higher. This can lead to a positive feedback mechanism, as deeper clouds release more latent heat which enables them to rise further. Wider clouds can transport more mass vertically as the mass flux scales with cloud base area. Cloud lifetime does not appear to be particularly sensitive to flux radius.

Figure 1.4 reveals that, similarly to Figure 1.3, an increase in flux amplitude also results in wider and deeper clouds that transport more mass. This can be explained by the fact that larger amplitudes initially produce more energetic thermals, and provide additional water vapour that, when condensed, is an extra source of latent heat. There is some additional complexity however - the largest flux amplitude results in a cloud that experiences a resurgence after around 90 minutes. This regenerated cloud develops in a markedly different location to the first (not shown), which implies it may be the result of indirect effects. This behaviour of cloud resurgence is investigated later in Chapter 1.3. As in Figure 1.3, varying the flux amplitude has little effect on cloud lifetime.

Figure 1.5 shows that increasing the duration of sensible and latent heat fluxes again produces wider and deeper clouds that transport more mass vertically, which is to be expected as larger amounts of energy are fed into the domain. All three curves initially evolve identically, but begin to diverge after 70 minutes as the time at which the fluxes are turned off is staggered. The cloud lifetime does not appear to be constrained by either flux duration, flux radius or amplitude, suggesting that cloud lifetime is determined primarily by the atmospheric profile rather than the surface forcing.

1.1.5 Multi Flux - Experimental Design

Now that the parameters of a single localised flux have been decided upon, it is possible to explore the evolution of a group of clouds that are forced identically using multiple localised surface fluxes. If the resulting thermals rise through a homogeneous boundary layer, it is expected that the clouds will develop in an identical manner; however in this simulation, the boundary layer is perturbed prior to flux initiation in order to develop a realistic turbulent environment. The rest of this chapter will analyse the extent to which the turbulent boundary layer influences the development of the clouds.

The experimental design during the first 60 minutes of simulation is identical to that of the Single_C simulation described earlier. After the 60 minute spinup period, four circular regions of increased sensible and latent heat flux are applied at the surface, one in each quadrant of the domain. The amplitude, radius and duration of these fluxes are identical to those described in Section 1.1.3. The centre coordinates of the four circular patches are:

- $x = 1 \text{ km}$, $y = 1 \text{ km}$ (Bottom Left quadrant),
- $x = 1 \text{ km}$, $y = 3 \text{ km}$ (Top Left quadrant),
- $x = 3 \text{ km}$, $y = 1 \text{ km}$ (Bottom Right quadrant), and
- $x = 3 \text{ km}$, $y = 3 \text{ km}$ (Top Right quadrant),

and are spaced evenly apart in both horizontal directions. A schematic of this setup is shown in Figure 1.6. The patches of increased heat flux continue for 10 minutes, after which they are switched off; the homogeneous sensible heat flux of 50 W m^{-2} continues throughout the simulation outside of the circular patches. This simulation is henceforth referred to as Multi_REF.

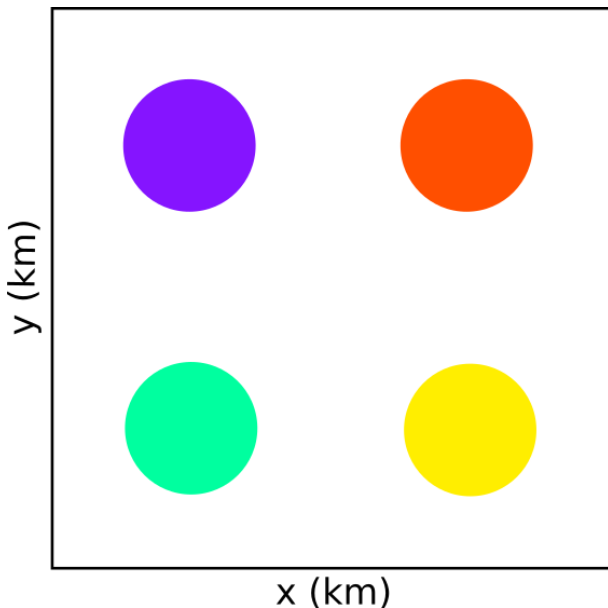


Figure 1.6: A schematic showing a plan view of the Multi_REF domain surface at 60 minutes into the simulation. Four circular regions of increased sensible and latent heat flux are located in each quadrant of the domain: Top Left (purple), Top Right (red), Bottom Left (green) and Bottom Right (yellow), with their centres positioned at (x,y) km = $(1,3)$, $(3,3)$, $(1,1)$ and $(3,1)$ respectively.

1.1.6 Results - Multi_REF

Cloud evolution

Figure 1.7 shows the cloud field 15 minutes after the initiation of the circular patches. This time frame was chosen as it corresponds approximately with the time of maximum mass flux by the four main clouds. The four clouds with the largest mass transport are shown in panel (d) - there is one in each domain quadrant, and they appear to correlate approximately with the location of the circular patches. The cloud in the top right quadrant at first glance appears to be much larger than the other three, with a greater amount of liquid water and a wider, more buoyant core. Hereafter, these clouds are referred to as Clouds TL, TR, BL and BR, named after their respective quadrants.

Figure 1.8 confirms that Cloud TR is significantly larger than the other three in terms of its cloud base mass flux, liquid water content, cloud top height and cloud base area. All four clouds follow a similar pattern of growth and decay, peaking at approximately 75 minutes and decaying around 90 minutes. An interesting feature is that Cloud TR experiences a short regeneration after this time, as evidenced by a prominent second peak in panels (a) and (d) between 90 and 110 minutes. The sudden drop in Cloud TR's cloud top height at 100 minutes is due to the final high, wispy fragments of the first cloud evaporating, which are then succeeded by a developing secondary cloud. Clouds TL, BL and BR exhibit an overall similar evolution in terms of width, height and strength (mass flux).

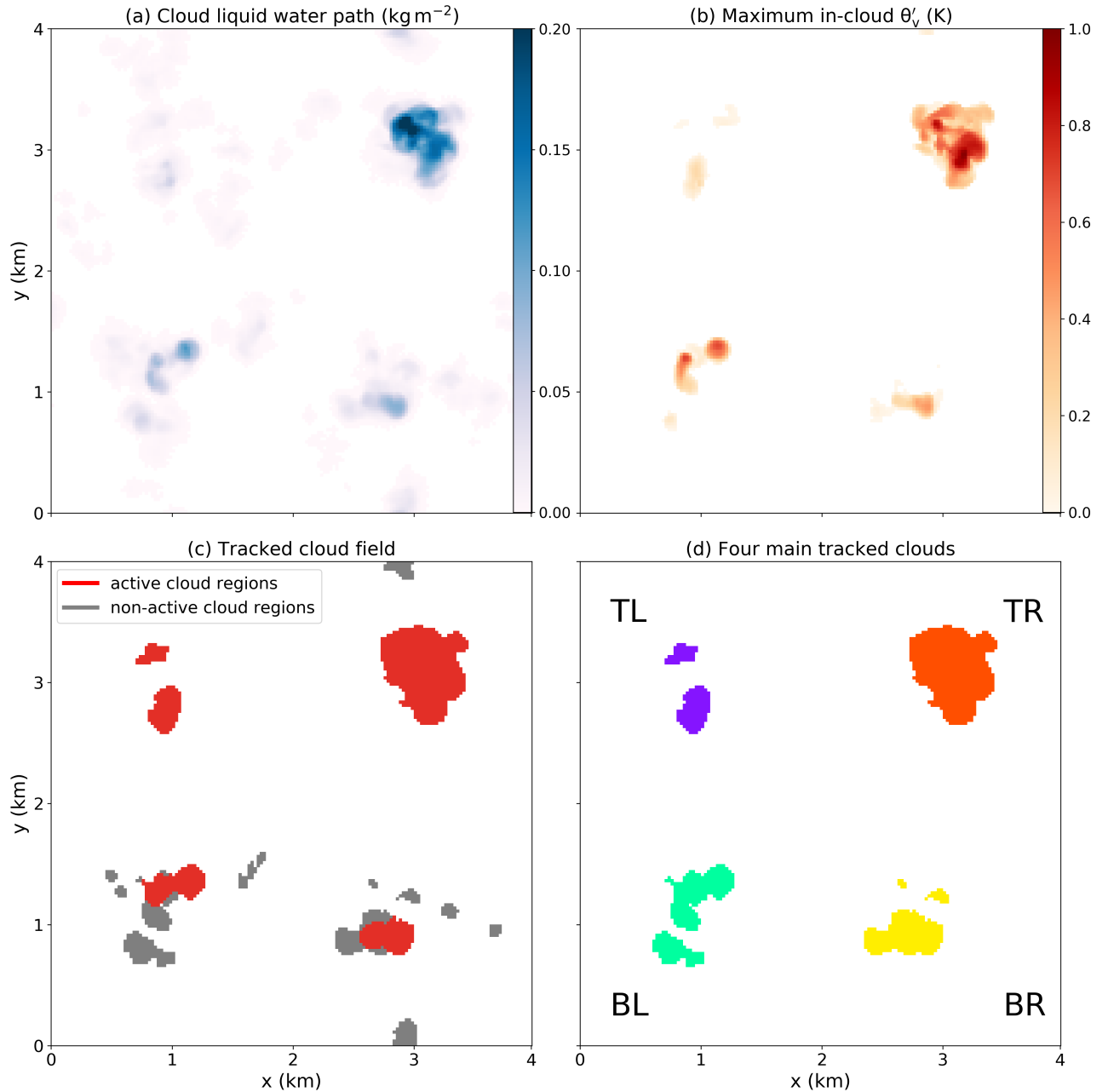


Figure 1.7: Cloud field properties from the multi flux simulation at 75 minutes into the simulation showing (a) cloud liquid water path, (b) maximum in-cloud values of θ_v perturbation from the horizontal mean, highlighting areas of positive buoyancy, (c) the tracked cloud field, with active cloud regions in red and non-active cloud regions in grey, and (d) the four largest clouds produced during the simulation, one in each quadrant and colour coded to match their input fluxes.

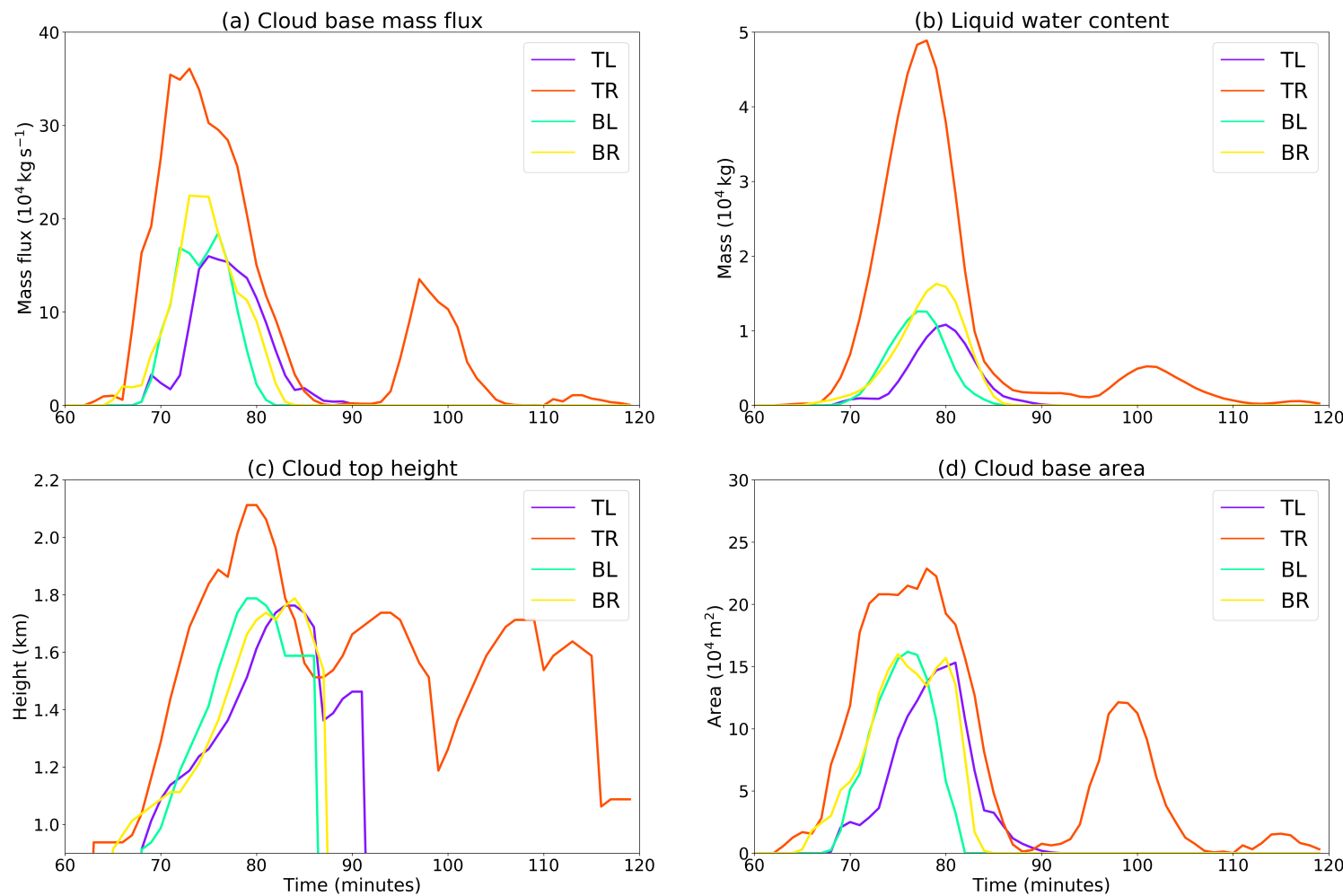


Figure 1.8: Evolution of (a) cloud base mass flux, (b) liquid water content, (c) cloud top height and (d) cloud base area between 60 and 120 minutes for clouds TL, TR, BL and BR. Cloud base mass flux and cloud base area here are defined using grid cells at cloud base with positive liquid water specific humidity and vertical velocity.

The maximum cloud base mass flux of Cloud TR is significantly larger than the other three, approximately double that of Cloud TL. Since the mass flux is a product of both cloud area and vertical velocity, one or both of these factors could be responsible for the large difference in mass flux. Figure 1.9 explores the behaviour of these two properties for clouds TR and TL. The average cloud base vertical velocity does not vary much between the two clouds, however there is a significant different in cloud base area, which suggests that the difference in mass flux between clouds TL and TR is primarily driven by the difference in cloud base area.

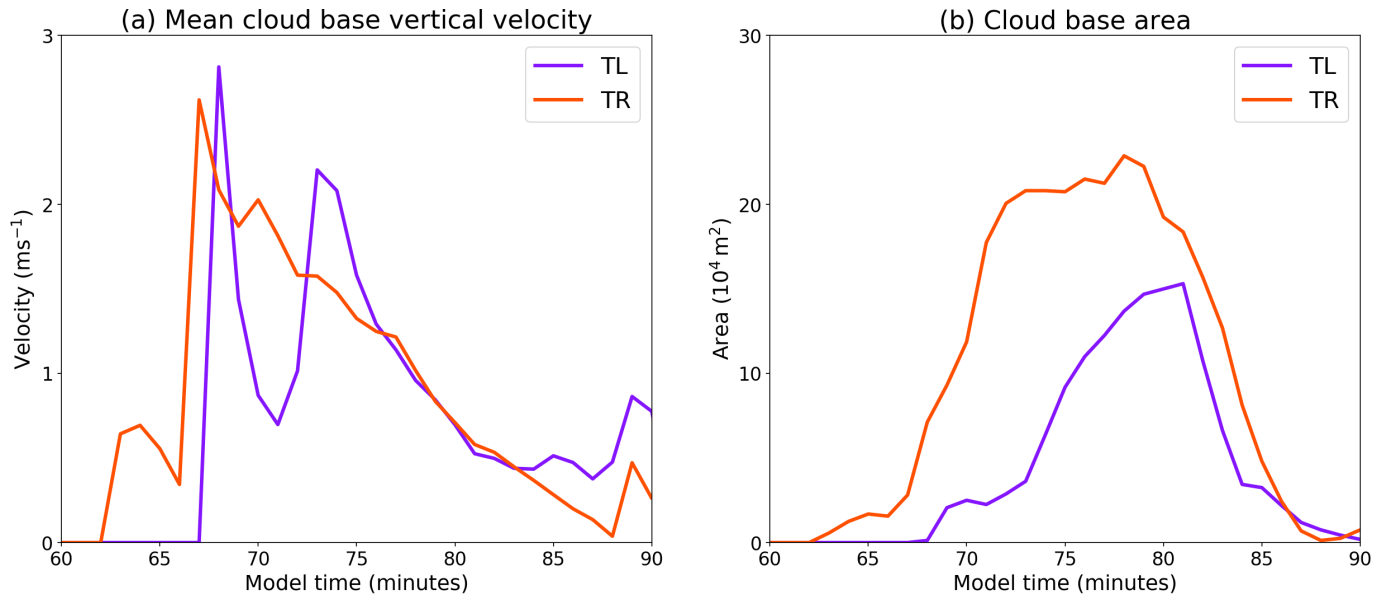


Figure 1.9: Evolution of (a) mean cloud base vertical velocity (in m s^{-1}) and (b) cloud base area (in m^2) for clouds TL (purple) and TR (red).

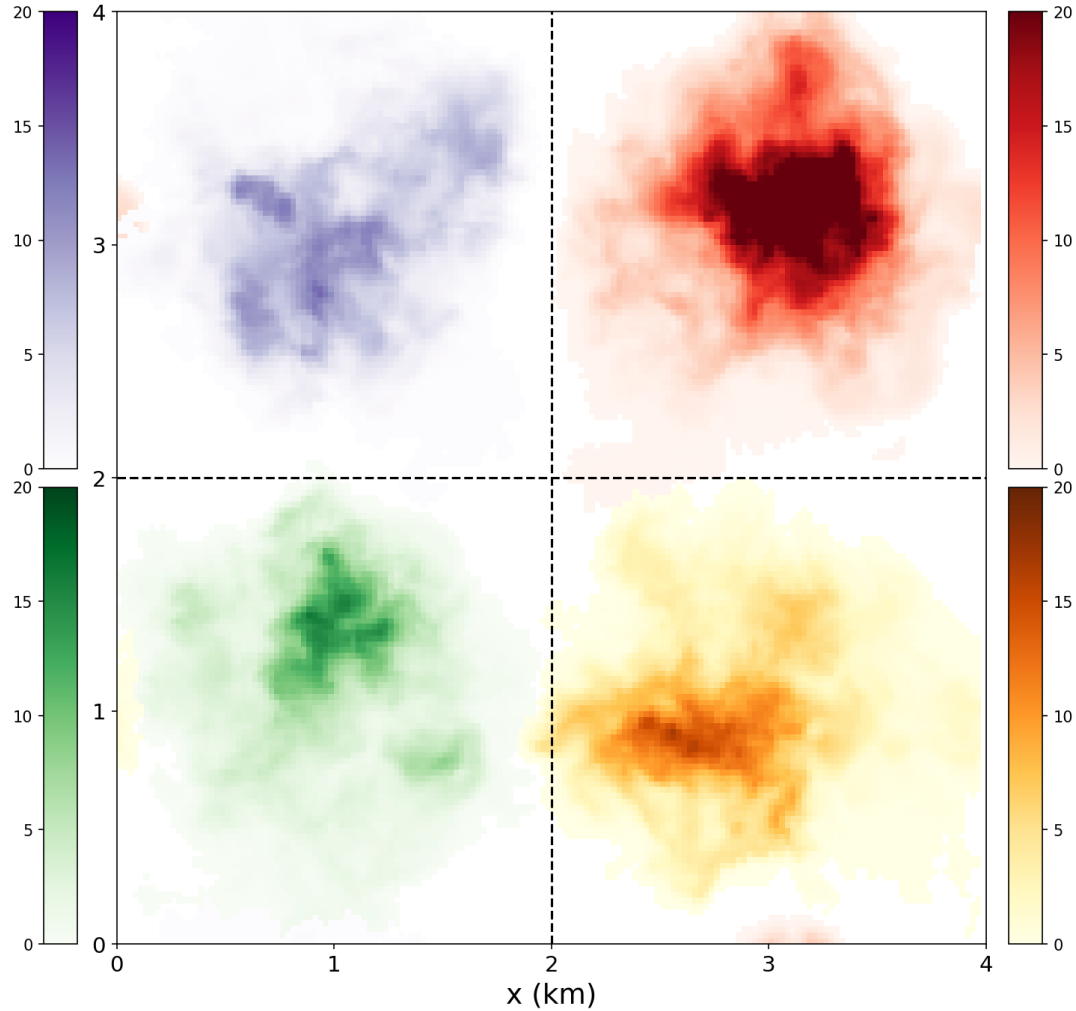


Figure 1.10: Integrated tracer concentration at 90 minutes from simulation Multi_REF. The tracer in each quadrant is given a different colour: purple (top left), red (top right), green (bottom left) and yellow/orange (bottom right).

Mixing between quadrants

It is important to assess the extent of thermodynamical interaction between the four quadrants. Four dimensionless surface tracer fluxes with values scaled to $1.0 \text{ m}^{-2} \text{ s}^{-1}$ are initialised in simulation Multi_REF, that scale in time and space with the four circular patches of increased sensible and latent heat fluxes. These tracers track the location of the four thermals and eventual clouds over time. Figure 1.10 shows the integrated concentration of these tracer fluxes 90 minutes into the simulation. It is clear that even by the time the clouds are decaying, there has been very little mixing between the quadrants, which means that direct thermodynamical interaction between the four clouds may be considered irrelevant for the rest of the analysis.

Atmospheric profiles

Differences in cloud evolution can also be assessed by considering the vertical structure of the cloud. In particular, the cloud core and shell can be analysed as separate structures, the definition of which are discussed in this section.

In Section ??, the purity tracer is reset to zero outside of a cloud at each timestep. It would therefore seem logical to use a threshold of $p = 0$ in order to distinguish regions of cloud from the environment. Figure 1.11(a) shows a cross-section of purity concentration p along the transect $y = 3000\text{m}$ at 75 minutes into the simulation. The boundary layer and Cloud TR are easily identifiable as regions of high p concentration, with p decreasing to zero above the boundary layer and with distance from all clouds. Various masks for thresholds of p are then applied, with the results shown in panels (b), (c) and (d).

A mask for grid cells with $p = 0$ is applied in panel (b). It would be sensible to assume that all grid cells outside the boundary layer and cloud field would be masked in this case; however, some grid cells with very small values of p are still retained using this threshold. Different masks are then applied in panels (c) and (d), using thresholds of $p < 0.1$ and $p < 0.001$ respectively: these masks give near-identical results, and provide a much cleaner, defined boundary between cloud and environment.

Figure 1.12 shows a cumulative probability density function (PDF) of $\log(p)$ in the cloud layer between 70-75 minutes. Values of $\log(p) = 0$ correspond to grid cells with pristine boundary layer air. There is a rapid transition for $-1 < \log(p) < 0$ as purity concentration rapidly decreases due to mixing with the environment. There is a comparatively stable zone for $-3 < \log(p) < -1$, in which the gradient of the slope becomes less steep. Since Figure 1.12 shows the cumulative PDF, this stable zone indicates a region in which low values of p are well separated from higher values, and therefore is useful in determining a boundary between cloud and non-cloud. A threshold value of $\log(p) = -3$ (i.e. $p = 10^{-3}$) is chosen for this boundary. The gradient becomes steep again for $\log(p) < -3$ and approaches zero in the environment.

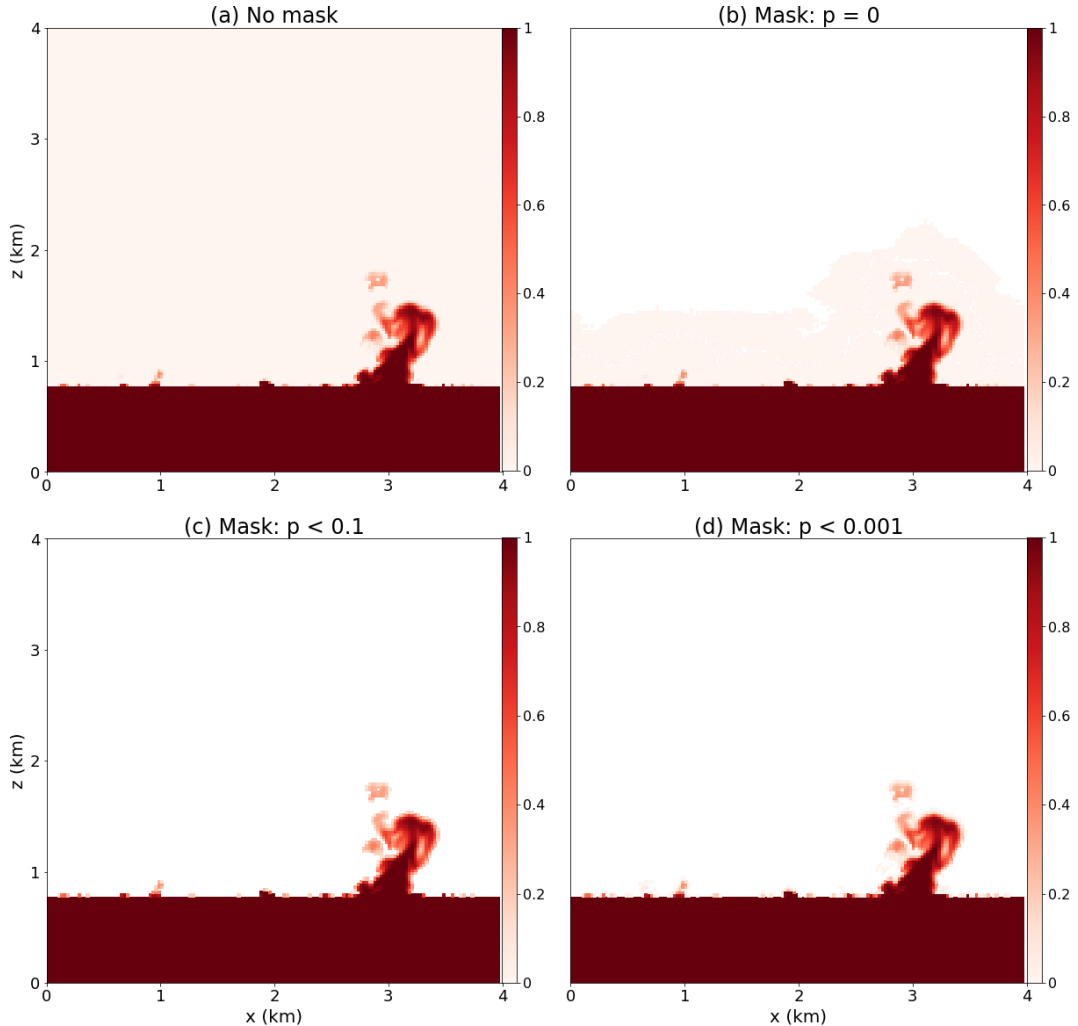


Figure 1.11: Cross-sections of purity tracer concentration p along $y = 3000\text{m}$ at 75 minutes into the Multi_REF simulation. White areas denote regions with zero purity concentration. Panel (a) shows p , and panels (b), (c) and (d) mask various thresholds of p .

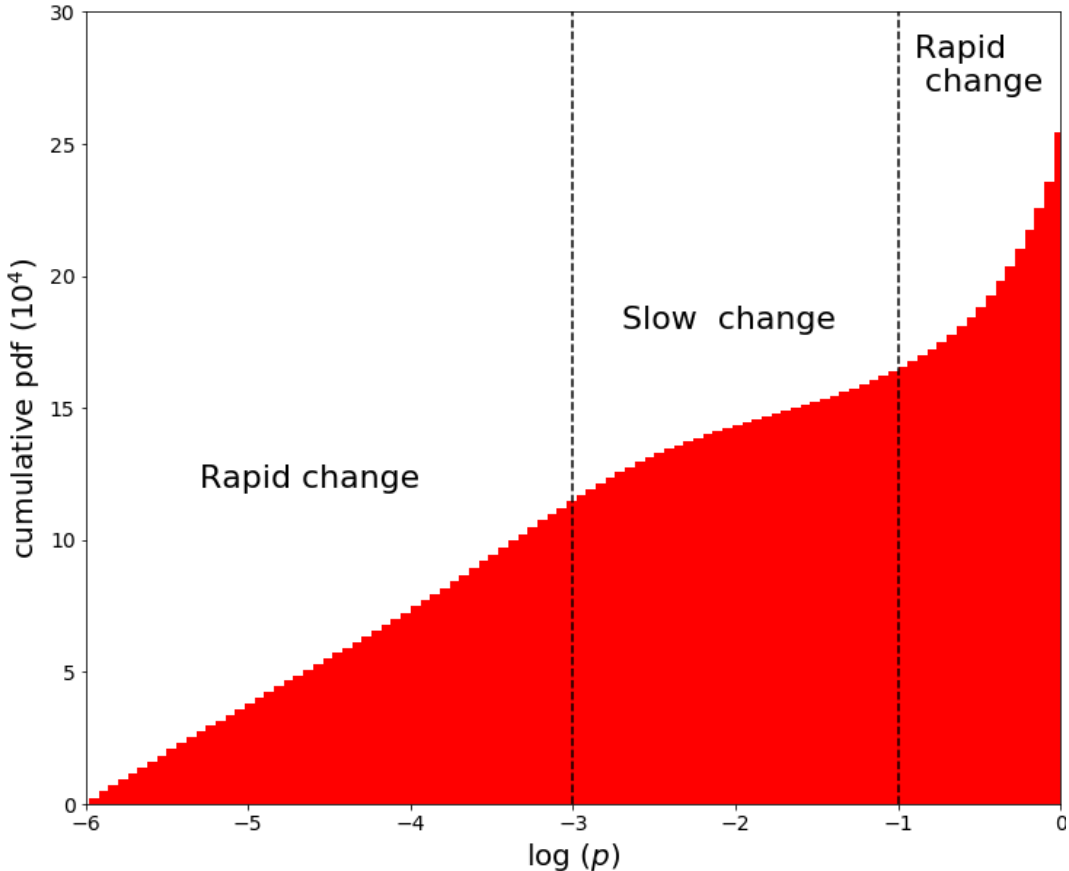


Figure 1.12: Cumulative PDF of $\log(p)$ in the cloud layer (between 800 and 2500m) between 70–75 minutes from the Multi_REF simulation. The number of bins used is 100, evenly spaced between $6 < \log(p) < 0$. The stable zone is shown between the vertical dashed lines for $-3 < \log(p) < -1$.

With a threshold chosen for purity concentration, regions corresponding to the environment, cloud core and shell can be defined. These regions are restricted to the cloud layer, i.e. above $z = 800\text{m}$, giving:

- Environment ($p \leq 10^{-3}$);
- Cloud core ($p > 10^{-3}$; $q_c > 10^{-5} \text{ kg kg}^{-1}$ and $w > 0.5 \text{ m s}^{-1}$); and
- Cloud shell ($p > 10^{-3}$; $q_c \leq 10^{-5} \text{ kg kg}^{-1}$ or $w \leq 0.5 \text{ m s}^{-1}$),

where p is purity tracer concentration, q_c is liquid water specific humidity and w is vertical velocity. Note that this definition of a cloud shell does not include regions where both $w \leq 0.5 \text{ m s}^{-1}$ and $q_c \leq 10^{-5} \text{ kg kg}^{-1}$.

Figure 1.13 is a visual snapshot of the moisture and vertical velocity in both the cloud core and shell regions. Note that the domain size here is reduced to show Cloud TR. In general, the cloud core is significantly moister and has

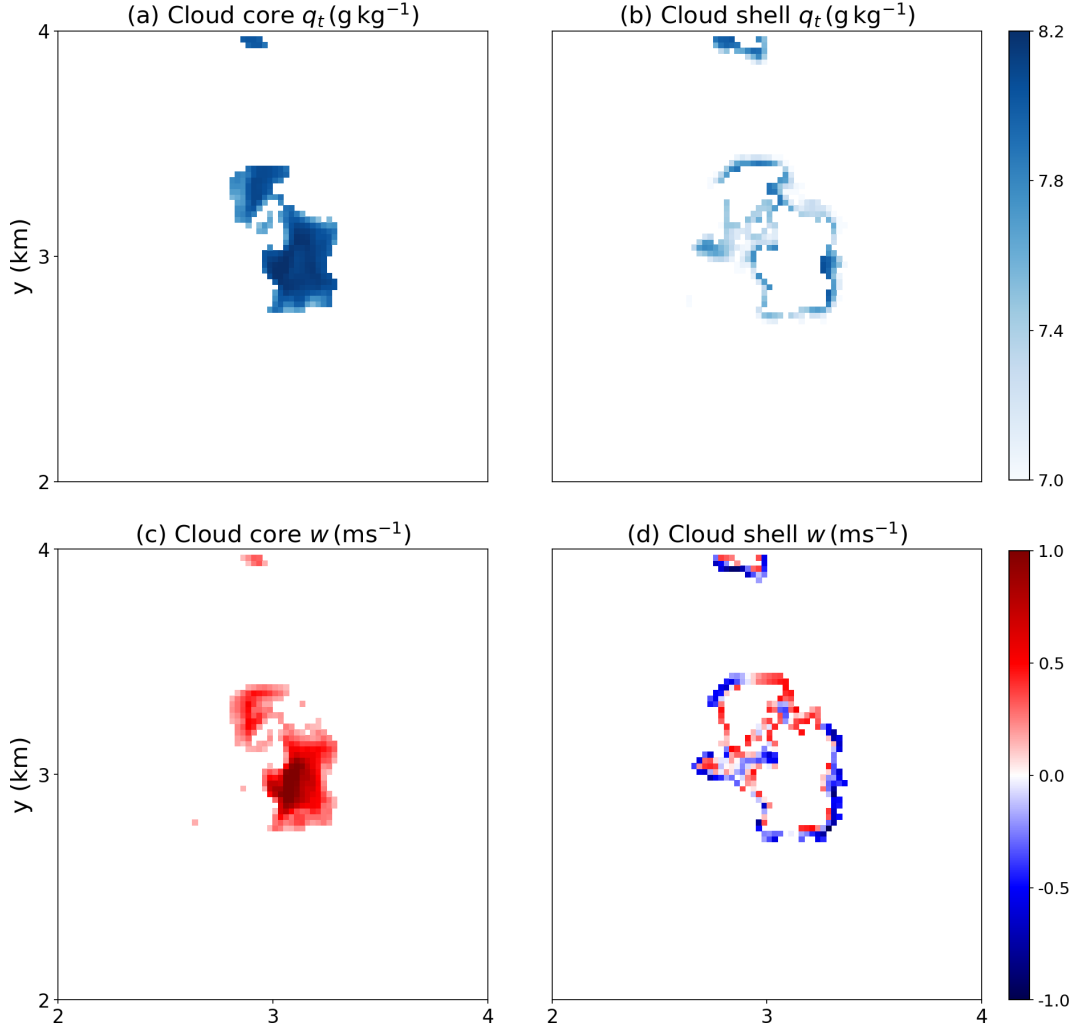


Figure 1.13: Cross sections along $z = 1\text{km}$ taken at 75 minutes into simulation Multi_REF, showing (top row) total specific humidity q_t (in g kg^{-1}) and (bottom row) vertical velocity w (in m s^{-1}). The cloud field is split into cloud core (left-hand column) and cloud shell (right-hand column).

greater vertical velocity than its shell. It may initially seem surprising that the cloud shell has grid boxes with positive vertical velocities, however this is possible when considering a single timeframe.

The evolution of average cloud core and shell properties with respect to horizontal domain mean is shown in Figure 1.14, during three phases of the cloud lifecycle. The middle column shows the peak phase of each cloud, defined as the mean time of maximum:

- cloud base mass flux
- liquid water content
- cloud top height
- cloud base area

The first and last columns are five minutes pre- and post- peak time, showing the growing and decaying phases respectively.

During the growing phase, cloud cores are consistently moister than their shells. Cloud cores and shells are both moister than the domain mean, as expected. Cloud core buoyancy is negative up to a height of around 1 km, indicating the presence of a convective inhibition (CIN) layer that air parcels must overcome using dynamic lifting only. Once air parcels generate enough momentum to overcome the CIN layer, they reach the level of free convection where they become positively buoyant and rise freely, as shown in panel (d). Cloud shell buoyancy is negative throughout the profile. In terms of mass flux, cloud cores are responsible for most of the upwards vertical transport; the cloud shell transports a small amount of mass upwards near cloud base, but on the whole generates a negative mass flux throughout the cloud layer. The thermodynamic profiles for both cloud cores and shells are extremely similar, however the mass flux profile for Cloud TR is significantly larger than the other three clouds at all levels.

During the peaking phase, cloud cores are still noticeably moister than their shells. The moisture content of both cores and shells decreases with height, partly due to turbulent mixing with the comparatively drier environment. All four clouds reach the level of neutral buoyancy (LNB) between 1.5-1.7 km; thereafter, cloud core buoyancy becomes negative and cloudy air is detrained, additionally explaining the decrease in total specific humidity. As before, there is little variation between the thermodynamic properties of each cloud, but there is still a noticeable difference in cloud core mass flux, with Cloud TR continuing to transport significantly more mass at all levels than the other three. The enhanced mass flux for Cloud TR could be due either to a larger fractional area or stronger

updrafts within the core region. Cloud TR continues to show a positive mass flux above the LNB, signifying an overshooting cloud top.

As each cloud begins to decay and detrain, the boundary between core and shell becomes diminished. This is evidenced by the solid and faded coloured lines becoming less distinguishable from each other in panels (c), (f) and (i). Each cloud begins to lose its region of positive buoyancy, and its positive mass flux is dramatically reduced.

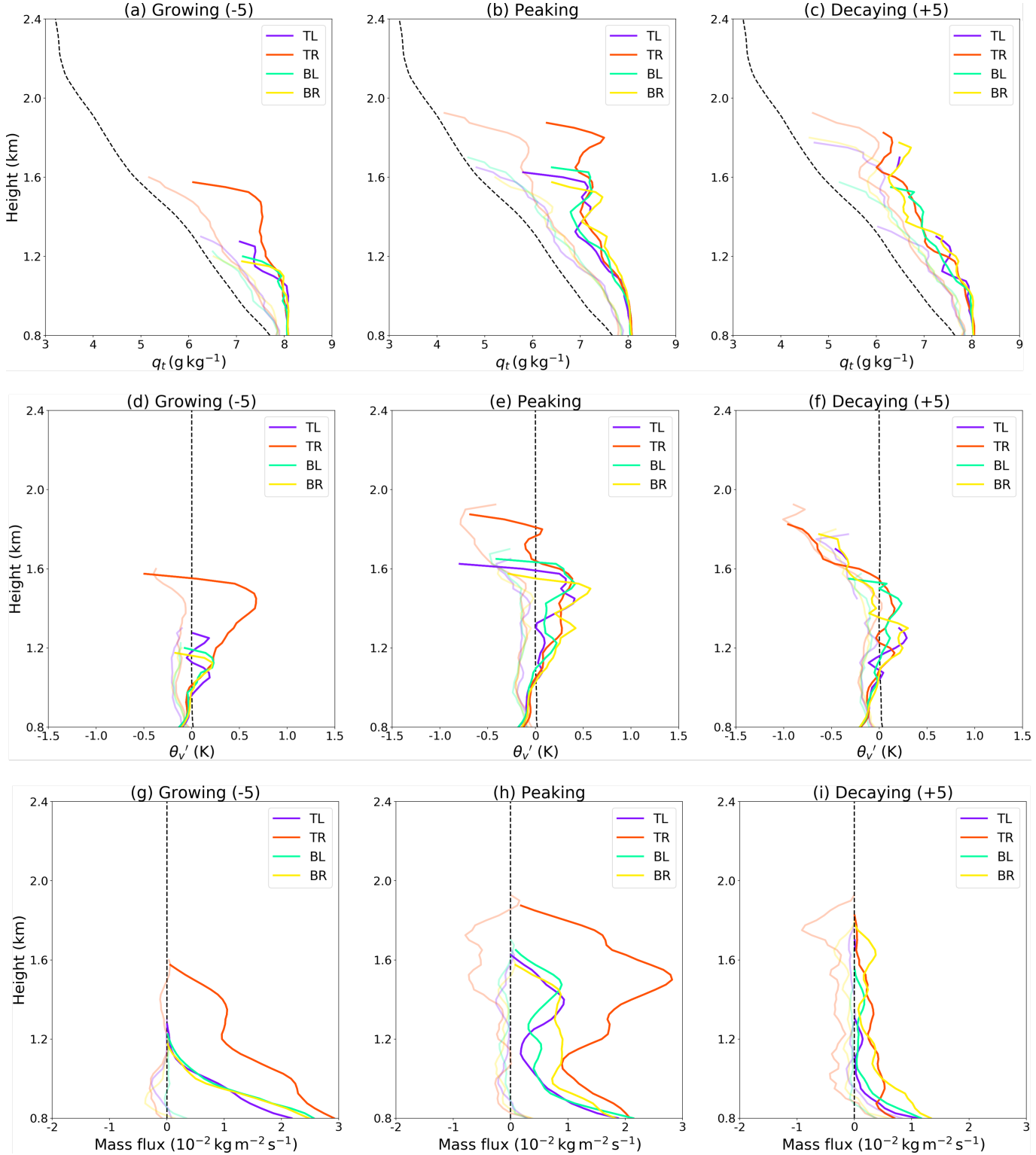


Figure 1.14: Evolution of cloud core and shell properties with respect to domain mean during three phases of the cloud lifecycle. The middle column shows the peaking phase of each cloud, defined as the time of maximum cloud base mass flux. The first and last columns are five minutes earlier and later, showing the growing and decaying phases respectively. The properties shown are: (top row) total specific humidity in g kg^{-1} , (middle row) buoyancy (defined as horizontal θ_v perturbation in K) and mass flux (in $\text{kg m}^{-2} \text{s}^{-1}$). Cloud core is depicted by solid colour lines, and cloud shell by faded colour lines. Domain mean values are depicted by black dashed lines.

In-cloud variability

The profiles in Figure 1.14 showed average differences between the four clouds. The profiles demonstrated a clear difference in cloud mass flux, and comparatively little difference in terms of cloud thermodynamic profiles. This next section will look at the variability within the clouds themselves rather than their average properties.

A measure of in-cloud variability is found by computing PDFs of total specific humidity, buoyancy and vertical velocity within both the cloud core and shell for each of the four clouds. The PDFs consider distributions between 60 and 90 model minutes, so as to capture the main lifecycle of each cloud. The cloud layer ranges between 800-2400m, a large region over which cloud properties would naturally be expected to vary significantly. Therefore cloud properties are considered over 200m intervals between 800-2400m, giving a total of 8 vertical levels.

A threshold is defined for which the number of grid points at each vertical level must exceed in order to be included in the PDF, to exclude fractionally small areas of cloud. The number of core (or shell) grid cells at a single level must be greater than 1 percent of the total core (or shell) grid cells integrated across cloud depth. This criteria results in data above 2000m being discarded in each quadrant, and data above 1800m being discarded for all quadrants except TR.

Figures 1.15, 1.16 and 1.17 are the distributions of specific humidity, buoyancy and vertical velocity. All distributions are normalised to account for changes in cloud volume, however cloud core volume at each level is noted in the legend for reference. Cloud core volume is always largest at cloud base and decreases with height, although it decreases at a much slower rate for Cloud TR.

Figure 1.15 confirms that cloud cores are moister than cloud shells at all levels. The distribution of q_t at cloud base is very narrow, with values remaining close to the adiabatic value of 8 g kg^{-1} . As height increases, average values of cloud core and shell q_t reduce, and their distributions broaden as drier environmental air is mixed in.

Figure 1.16 reveals that cloud core and shell buoyancy close to cloud base have similar distributions. With increasing height, the disparity between core and shell grows, as the core becomes more positive buoyancy and the shell becomes more negatively buoyant. As the LNB is approached around 1.5km, the positive buoyancy in the core reduces, as evidenced by the distribution moving towards more negative values as height continues to increase. Towards the top of the cloud,

the difference in cloud core and shell distributions becomes less pronounced as the boundary between both becomes eroded.

Finally, Figure 1.17 confirms that vertical velocity w is always positive in the cloud core, and is either negative or weakly positive in the cloud shell as expected. With increasing height, the cloud core initially experiences an increase in w , as observed by the gradual spreading of the tail. In contrast, the cloud shell experiences a relative decrease in w to counteract the stronger updrafts in the core. As the clouds approach the LNB, they decelerate, as evidenced by a decrease in cloud core w within the tail at near the top of the cloud.

The distributions of specific humidity, buoyancy and vertical velocity are fairly similar between the four quadrants. Any differences between the quadrants are most obvious at the level closest to cloud base (red line) where the moisture content, buoyancy and vertical velocity in the cloud core are on the slightly higher side. On the whole, the differences between distributions are small. This implies that the actual ‘makeup’ of the four clouds from the Multi_REF simulation is very similar, and the differences in cloud evolution are due almost entirely to differences in cloud size. The question that follows then is which mechanisms are responsible for the variations in cloud size?

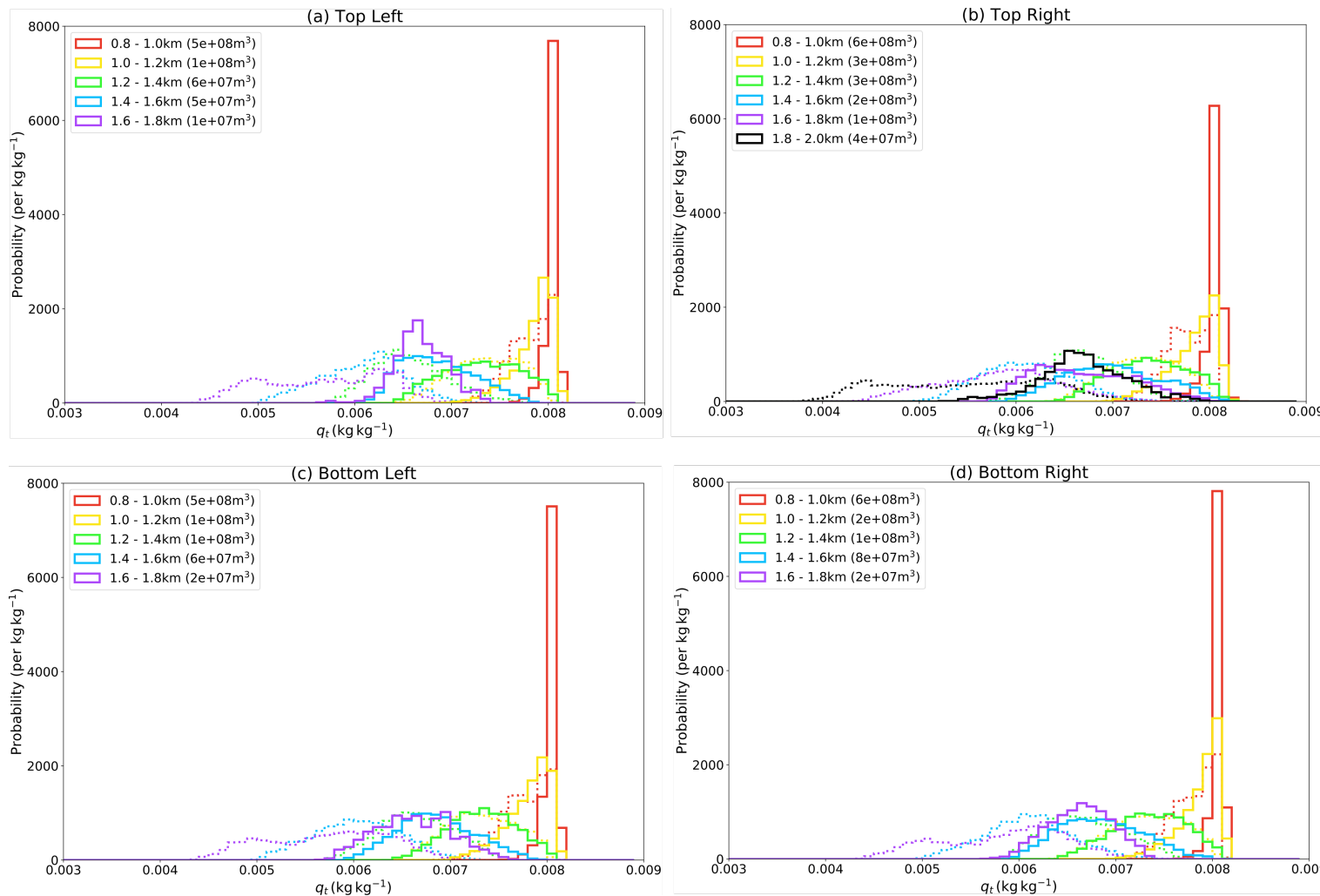


Figure 1.15: Probability density function of total specific humidity q_t (kg kg^{-1}) in each domain quadrant, separated into cloud core (solid lines) and shell (dotted lines). The bins are defined at regular intervals of 0.1 g kg^{-1} . The data are separated into vertical regions of 200m thickness, and the corresponding cloud core volume (in m^3) is shown in the legend.

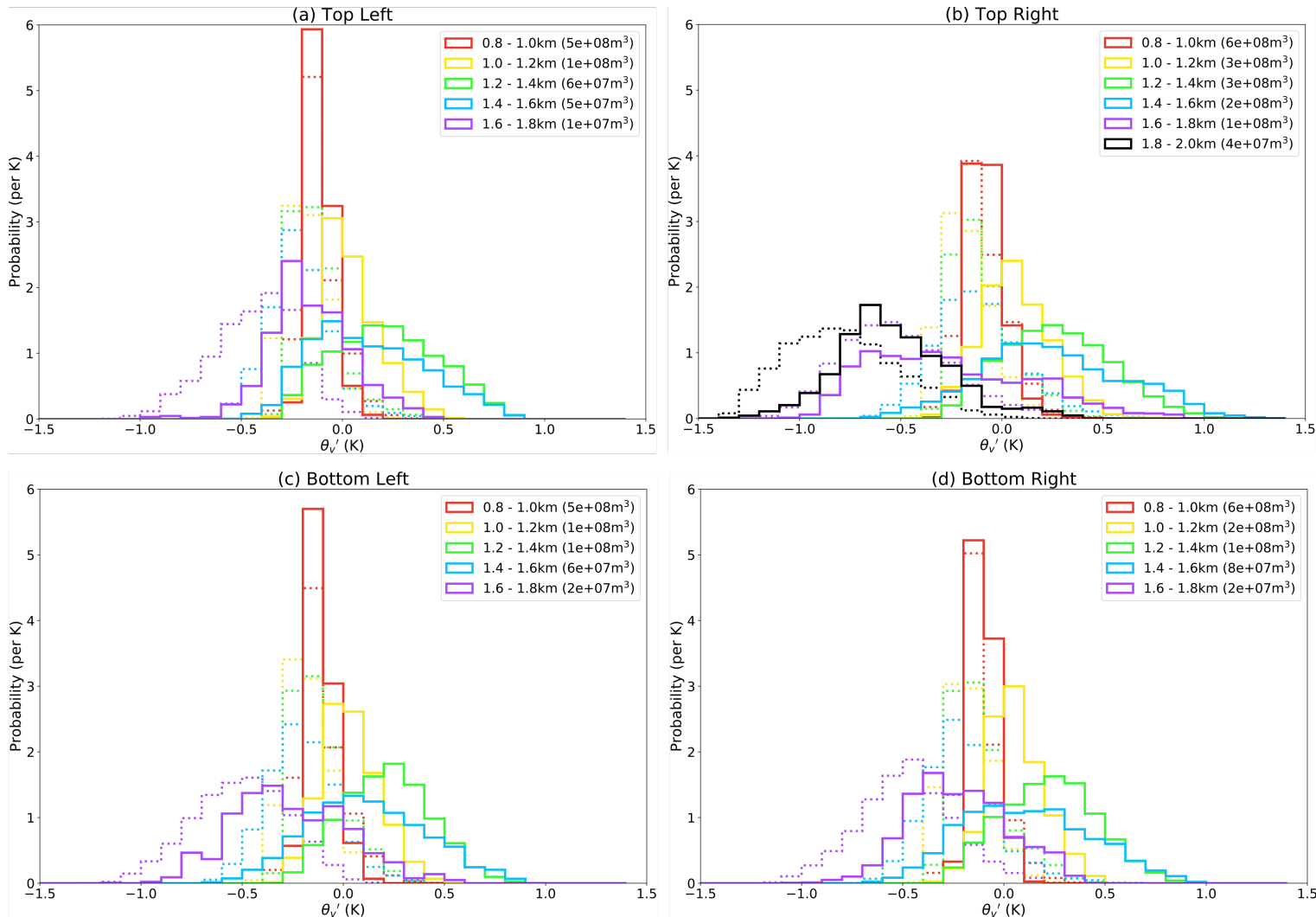


Figure 1.16: Probability density function of buoyancy θ_v' (K) in each domain quadrant, separated into cloud core (solid lines) and shell (dotted lines). The bins are defined at regular intervals of $0.1 K$. The data are separated into vertical regions of $200m$ thickness, and the corresponding cloud core volume (in m^3) is shown in the legend.

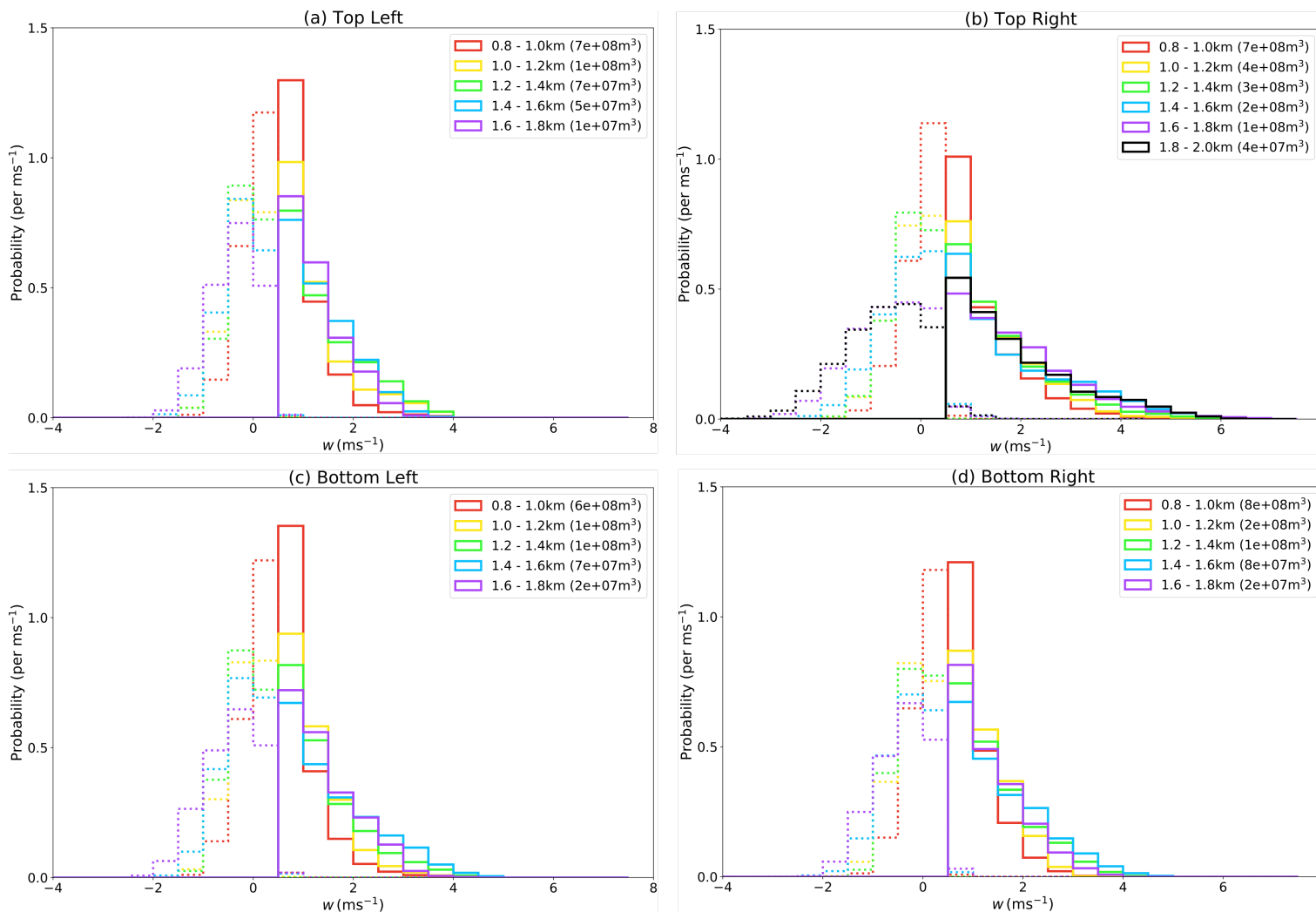


Figure 1.17: Probability density function of vertical velocity $w (\text{m s}^{-1})$ in each domain quadrant, separated into cloud core (solid lines) and shell (dotted lines). The bins are defined at regular intervals of 0.5 m s^{-1} . The data are separated into vertical regions of 200m thickness, and the corresponding cloud core volume (in m^3) is shown in the legend.

1.1.7 Summary

In this section, localised surface patches of sensible and latent heat flux are used to generate isolated convective clouds which grow and decay over a 30 minute period. The size of these clouds is sensitive to changes in the flux amplitude, duration, and particularly to changes in flux radius. The lifetime of a single cloud is unaffected by variations in the surface forcing parameters, appearing to be defined solely by the atmospheric profile.

In a turbulent convective boundary layer, the introduction of multiple identical localised surface fluxes may result in significant differences in convective cloud development, both in terms of the size and strength of convection and also in terms of the potential for cloud regeneration. Differences in cloud base mass flux appear to be driven primarily by changes in cloud base area rather than average updraft speeds at cloud base.

The boundary between convective clouds and their environment may be defined using a threshold of purity tracer concentration; the clouds themselves can be split into core and shell partitions using thresholds of both liquid water specific humidity and updraft speed. Average thermodynamic profiles in the cloud cores and shells do not vary significantly between the four clouds, however there is a notable difference in the cloud core mass flux profiles, which is significantly larger for Cloud TR. The contrast in mass flux may be driven by differences in cloud core fractional area and/or differences in core updraft strength. Despite the variation in the average mass flux profiles, the dynamic and thermodynamic variability within each of the four clouds is remarkably similar, suggesting that differences in cloud evolution are due almost entirely to differences in their size.

1.2 Below cloud: Boundary-layer controls on convective cloud development

1.2.1 Motivation

Causes of CBL variability

Section 1.1 concluded that the localised boundary layer variations observed at the end of model spinup in Multi_REF were the root cause of the differences in the development of the four identically-forced clouds. These fluctuations are the result of model spinup, a necessary step in creating a turbulent convective boundary layer (CBL). Turbulent eddies in the CBL generate fluctuations in the velocity field, as well as the moisture and temperature fields through advection. Couvreux et al. (2005) similarly found that despite using horizontally-homogeneous initial profiles and homogeneous surface forcing, random perturbations of potential temperature near the surface during spinup resulted in boundary layer sub-mesoscale water vapour variability, which they attributed to circulations in the CBL.

Figure 1.18 shows the horizontally-averaged thermodynamics at the end of model spinup, along with the variance. The variance of a field x , σ_x^2 , is defined as

$$\sigma_x^2 = \frac{\sum_{i=1}^n (\bar{x} - x_i)^2}{n} \quad (1.3)$$

where the overbar denotes a horizontal mean, and n is the number of grid points in the horizontal. Since n is identical at each vertical model level, the denominator in Equation 1.3 can be ignored leaving the numerator only. Figure 1.18 shows that the variance in q_v and θ is orders of magnitude smaller than the mean. This means that the variation in thermodynamics at the end of model spinup can be considered small, yet they still result in large differences in cloud development once the circular patches are introduced.

the red shading is one standard deviation from the mean.

Effects of CBL variability on convective cloud development

Previous studies have shown that variation in CBL thermodynamics influences cloud development. For example, Stirling and Petch (2004) used a cloud resolving model and found that boundary layer fluctuations of moisture and temperature results in earlier onset of deep convection over land. Zhang and Klein (2010)

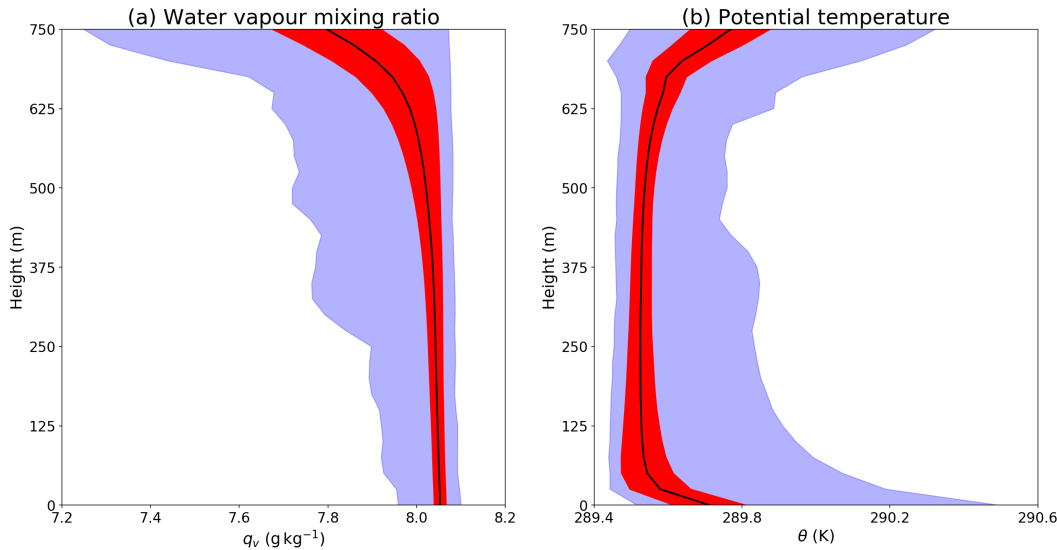


Figure 1.18: Thermodynamic conditions at the end of model spinup for simulation Multi_REF. Panel (a) shows water vapour mixing ratio q_v and panel (b) shows potential temperature θ . The black lines represent horizontally-averaged fields, the red shading represents one standard deviation from the mean? and the blue shading represents the minimum and maximum values.

investigated the transition from shallow to deep convection over land using field observations, and concluded that greater CBL inhomogeneity in terms of thermodynamics, horizontal wind and moist static energy aids in this transition; additionally, boundary layer fluctuations are positively correlated with larger future rainfall amounts and rates. Hirsch et al. (2017) noted using air parcel simulations that pockets of high relative humidity in the middle of the CBL aid in convection initiation, sometimes producing shallow convective clouds on days where typical forecasting methods predict zero cloud cover.

The two clouds in Multi_REF that exhibit the most extreme variation in development are clouds TL and TR, and the evolution of their cloud base mass flux is shown in Figure 1.19(a). Figures 1.19(b) and (c) show the corresponding mean cloud base vertical velocity and cloud base area. It is clear that the large variation in cloud base mass flux between clouds TL and TR is driven primarily by differences in cloud base area rather than mean updraft speeds at cloud base. This chapter explores the physical mechanisms in the CBL which directly influence maximum cloud base area ('nature'), and the indirect effects on cloud development through eventual differences in entrainment and dilution rates ('nurture'). This idea of the competing effects of nature versus nurture was first introduced by Romps and Kuang (2010), who concluded that nurture (in terms of stochastic entrainment) was the important factor for determining the

fate of convective parcels. In simulation Multi_REF, the environmental properties surrounding each of the four clouds is approximately identical, and therefore the rate of cloud dilution will be fundamentally related to the properties at cloud base. In this sense, both nature and nurture are closely related to each other.

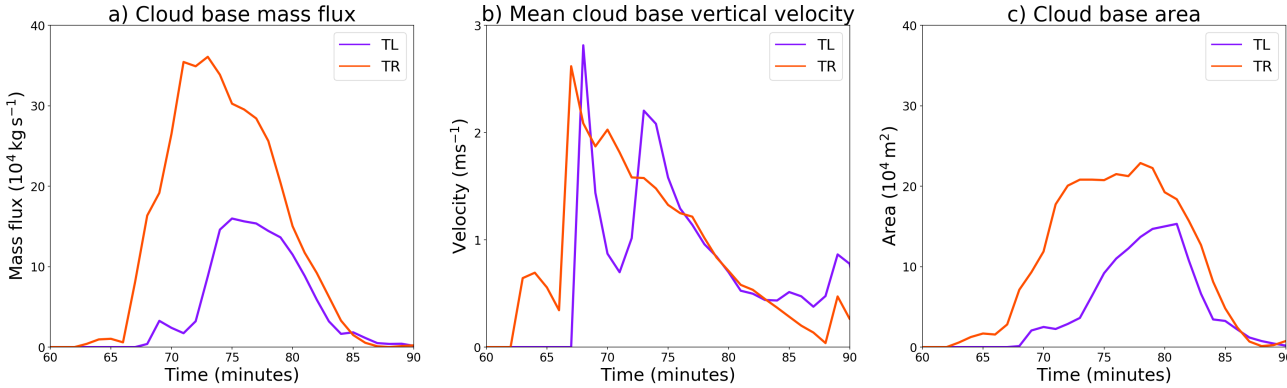


Figure 1.19: Timeseries of (a) cloud base mass flux, (b) mean cloud base vertical velocity and (c) cloud base area for clouds TL (purple) and TR (red).

Research questions

The results from Chapter 1.1 raise some important questions, which will be explored in this chapter. These questions include:

- Which CBL properties determine conditions at cloud base?
- What is the relative importance of the above properties, and are they important on a particular scale?
- How do cloud base properties (and size) determine the development of convective clouds?
- How might knowledge gained from the questions above inform future convective parametrisations?

Chapter overview

This chapter will explore the mechanisms behind the variation in cloud development arising from the Multi_REF simulation. In particular, the main hypothesis that is explored here is that localised variations in CBL dynamic and thermodynamic properties at the end of model spinup influence the maximum cloud base area attained by the four main clouds. The layout of this chapter is as follows:

Section 2 introduces the properties of interest in the boundary layer, and sets out the general methodology. Section 3 presents the results, which are separated into the relative importance of CBL moisture, buoyancy and vertical velocity, as well as the influence of moisture and buoyancy on cloud dilution. Section 4 summarises these results, and discusses how they may be explored further in a more realistic convective environment.

1.2.2 Method

As previously mentioned, the 60 minute spinup period in Multi_REF results in the formation of turbulent structures which lead to localised variations in the CBL. Such variations are known to affect cloud initiation and development, and may explain the differences between the four main clouds (TL, TR, BL and BR). In this chapter, the dynamic and thermodynamic properties of the boundary layer at the end of the spinup period are analysed, to assess whether there is a correlation to maximum cloud base area (and therefore the mass flux) of the four main clouds. The three properties considered are:

- Boundary layer water vapour path,
- Integrated boundary layer buoyancy, and
- Boundary layer updraft strength.

The buoyancy B is related to virtual potential temperature θ_v , a measure which depends on both temperature and moisture. θ_v is defined as

$$\theta_v = \theta(1 + 0.61(q_v - q_l)) \quad (1.4)$$

where θ is potential temperature (K), q_v is the water vapour mixing ratio (kg kg^{-1}) and q_l is the liquid water mixing ratio (kg kg^{-1}). Integrated buoyancy over the depth of the CBL is denoted as \widehat{B} , where the overhat represents a vertical integral, and is defined as

$$\widehat{B} = \int_{z_1}^{z_2} B dz = g \int_{z_s}^{z_c} \frac{\theta_v'}{\theta_v} dz$$

with units of $\text{m}^2 \text{s}^{-2}$. Here, g is gravitational acceleration ($\approx 9.8 \text{ m s}^{-2}$), prime terms denote a deviation from the horizontal mean, $z_s = 0\text{m}$ (the surface) and $z_c = 800\text{m}$. Unless otherwise stated, z_c will henceforth be used to denote the level of cloud base.

Figure 1.20 shows the water vapour path, integrated buoyancy and vertical velocity at a height of 250m over the location of the four circular surface patches at the end of model spinup. Vertical velocity at 250m, approximately a third of the way up the boundary layer, is a measure of boundary layer updraft strength - the motivation for this is discussed in Section 1.2.3.

The analysis of each of these three properties is broadly separated into three sections. First, the distribution of each property is assessed across each domain quadrant, to see whether there are obvious differences that explain the variation in cloud development. The distribution across each quadrant is then compared to the distribution of properties directly over each circular patch, to determine the importance of localised atmospheric properties.

Second, a linear regression quantifies the relationships between each CBL property and maximum cloud base area. Due to the small number of clouds sampled, two extra simulations were run, identical to Multi_REF except that the circular patches were initialised either five minutes earlier or later. These additional simulations (referred to as Multi_-5 and Multi_+5 for patches initialised five minutes earlier or later respectively) provide a further eight clouds which are included in the regression analysis. A full description of all model runs can be found in Table ??, Appendix A.

Third, the relationships between boundary layer thermodynamics (water vapour path and integrated buoyancy) and cloud development is explored in more detail using idealised LES simulations.

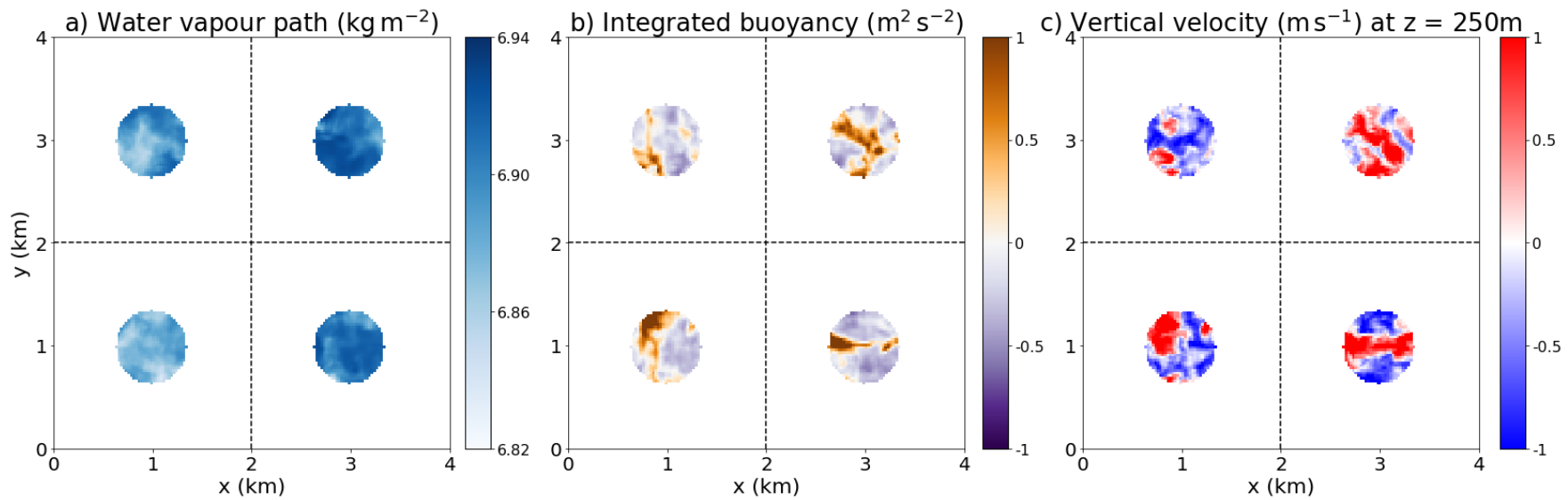


Figure 1.20: Multi_REF boundary layer properties over the location of the four patches at the end of model spinup ($t = 60$ minutes). Panel (a) is water vapour path, panel (b) is integrated buoyancy and panel (c) is vertical velocity 250m above the surface.

1.2.3 Results

Boundary layer water vapour path

Figure 1.21(a) shows the distribution of CBL water vapour path (\widehat{W}_v) across each of the four domain quadrants at the end of model spinup. The distribution is normalised such that the area underneath each curve is equal to 1. It is immediately obvious that there is very little variation across the four quadrants - the distributions all have a slight negative skew and a similar spread of values. In terms of cloud development, Cloud TR exhibits the most extreme differences compared to the other three, however panel (a) does not suggest any relationship to \widehat{W}_v .

In contrast, Figure 1.21(b) shows the corresponding distribution of \widehat{W}_v directly over the location of the four circular patches. In comparison to Figure 1.21(a), the spread of values over each patch has reduced, particularly from the tail ends of the distributions. The most significant tail reduction is observed across patch TR, indicating that the lowest values of \widehat{W}_v in this quadrant are located outside of the circular region. Additionally, the peak of TR's distribution is shifted to the right, demonstrating that the highest values of \widehat{W}_v in (a) are clustered above this circular region. This may be an indication that localised variations in the boundary layer water vapour path play a role in cloud development. On the other hand, clouds BL and BR follow a similar evolution, and yet their \widehat{W}_v distribution in panel (b) are very different from each other - values of \widehat{W}_v over patch BR are generally higher than those over patch BL. It is impossible to say from Figure 1.21 whether there is indeed a relationship between localised \widehat{W}_v and cloud development, since there may be conflicting processes at play. Statistical analysis is used to investigate the link between CBL moisture and cloud size, and in particular to answer the question: is there is a correlation between localised boundary-layer moisture anomalies and the maximum cloud base area a cloud attains?

Before this question is addressed, it is important to define exactly what is meant by the word 'localised'. In Figure 1.21(b), boundary layer conditions were masked directly above the location of convective forcing. This was motivated by the fact that the circular patches of increased heat and moisture fluxes produce thermals, which are known to act as the roots of convective clouds (e.g. Couvreux et al. 2010), therefore it makes sense to presume that the atmospheric conditions through which the thermals rise will have a direct influence on cloud development. However, it could also be argued that the zone of influence includes only a fraction

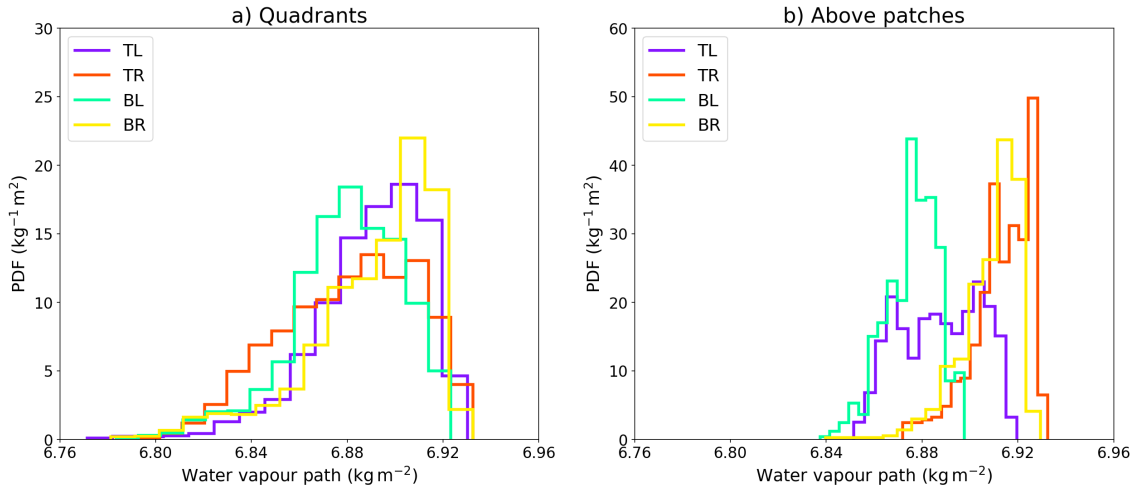


Figure 1.21: Distribution of boundary layer water vapour path from Multi_REF across (a) each quadrant and (b) each circular patch, taken at the end of model spinup.

of the patch, or conversely may include a slightly wider area. When a thermal rises from the surface, it does not move as a homogeneous block of air; instead its motion is influenced by turbulence and pre-existing CBL structures. The air parcels directly feeding into cloud base may therefore originate from beneath the cloud, rather than directly above the circular patches alone. A second option is to assess the atmospheric conditions directly underneath maximum cloud base area, which occurs at slightly different times for each of the four clouds. An example of these two masks used on the \widehat{W}_v field is shown in Figure 1.22. A benefit of this second mask is that it makes analysis easier for larger simulated cloud populations that use more realistic homogeneous surface fluxes.

To investigate the relationship between \widehat{W}_v and maximum cloud base area, a linear regression is performed. The first step is to calculate the domain-average \widehat{W}_v at the end of model spinup, and then calculate the anomalies in the masked region (either directly above the patches, or underneath the maximum cloud base area). The mean anomaly in each masked region is then plotted against the maximum cloud base area, and shown in Figure 1.23(a). The results from simulations Multi_+5 and Multi_-5 are also included, giving a total sample size of 12 clouds. A linear regression is then performed, and the regression line and coefficient of correlation r are shown in the same plot. Figure 1.23(b) additionally shows the results of a linear regression for the fraction of grid boxes in the masked region with a positive anomaly and maximum cloud base area.

Figure 1.23 demonstrates that both average \widehat{W}_v anomalies and the fractional area with a positive \widehat{W}_v anomaly are positively correlated with maximum cloud

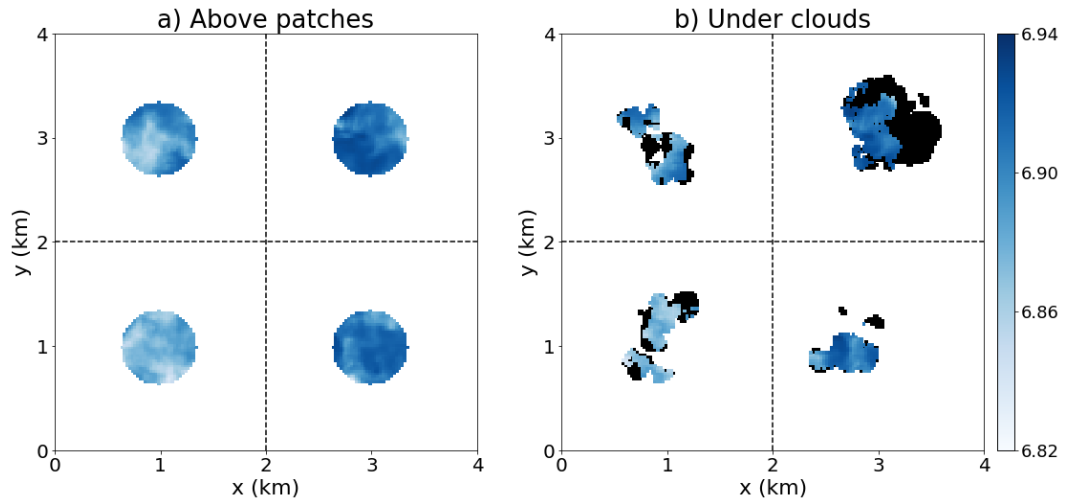


Figure 1.22: Results from simulation Multi_REF showing boundary layer water vapour path (in kg m^{-2}) at end of spinup period. Panel (a) shows the field masked directly over the four patches/heat fluxes (with radius = 350 m). Panel (b) shows the field masked underneath the maximum extent of each cloud (in black) and the corresponding maximum cloud base area (in blue shading).

base area, and therefore to cloud base mass flux. Both masked areas results in a positive trend, however the cloud mask results in the strongest correlation - this may be an indication that clouds develop over pre-existing structures in the CBL as discussed earlier. Despite the positive correlation between mean \widehat{W}_v anomalies beneath the cloud and cloud base area, the coefficient of determination (r^2) is 0.37, meaning that these moisture anomalies explain less than 40% of the variation in maximum cloud base area. Additionally, the sample size is small, making it difficult to draw a firm conclusion; however, the results so far point towards a relationship worth investigating further using idealised LES.

Four new simulations are run, each with an identical setup to simulation Single_C (see Chapter 1.1 for a comprehensive description), but with the exception of the circular patch whose location differs in each simulation. The total five simulations, with centre coordinates of the circular patch given in brackets, are then:

- Single_C ($x = 2\text{km}$, $y = 2\text{km}$)
- Single_TL ($x = 1 \text{ km}$, $y = 3 \text{ km}$)
- Single_TR ($x = 3 \text{ km}$, $y = 3 \text{ km}$)
- Single_BL ($x = 1 \text{ km}$, $y = 1 \text{ km}$)

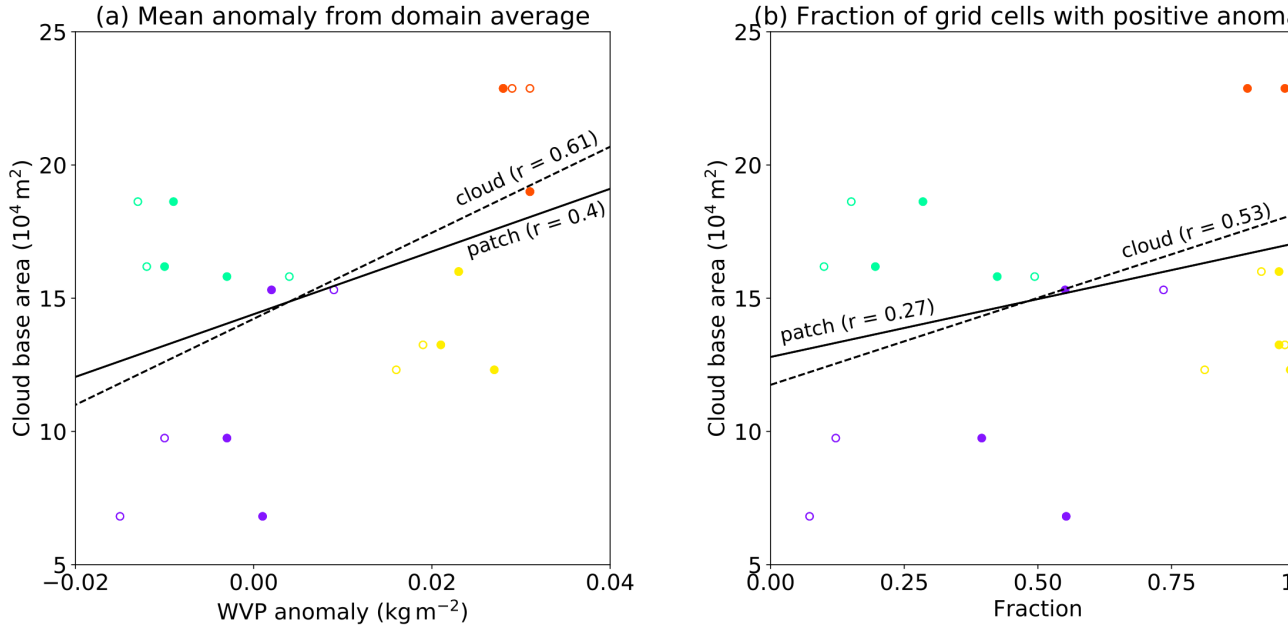


Figure 1.23: Scatterplots of (a) mean \widehat{W}_v anomaly and (b) fraction of grid cells with a positive \widehat{W}_v anomaly, both calculated at the end of model spinup, against the maximum cloud base area of each cloud. The boundary layer has been masked both above the circular patches (denoted by filled circles) and underneath the maximum cloud base area of the four clouds (unfilled circles). Linear regressions and corresponding r are also shown (solid line is for patches, dashed line is for clouds).

- Single_BR ($x = 3 \text{ km}$, $y = 1 \text{ km}$)

An additional five simulations are then run, identical in setup to those described above, but with the inclusion of a localised moisture perturbation at the end of model spinup. These simulations are referred to as Single_X_moist, where X denotes the location of the patch, and are listed in Table ??, Appendix A. The moisture perturbation takes the form of an additional 1 g kg^{-1} of water vapour applied to each grid box within a defined cylindrical region. The cylinder is positioned directly above the circular patch, and has a radius of 350m and a height of 750 m (i.e. it is contained within the boundary layer).

To separate the effect of moisture increasing buoyancy, the temperature inside the cylinder is adjusted to keep the buoyancy unchanged. Recall that buoyancy is a function of virtual potential temperature θ_v , which in turn is a function of potential temperature θ , water vapour mixing ratio q_v and liquid water mixing ratio q_l (see Equation 1.4). It follows therefore that as q_v increases, in order to conserve θ_v , θ must decrease inside the cylinder.

Before the moisture content is increased, the virtual potential temperature in the boundary layer (θ_{v1}) is defined as

$$\theta_{v1} = \theta_1(1 + 0.61q_v), \quad (1.5)$$

where θ_1 is the initial potential temperature. Note that the q_l term from Equation 1.4 disappears as the CBL contains no liquid water. An increase in moisture of 1 g kg^{-1} results in a new virtual potential temperature θ_{v2} . The potential temperature is adjusted by an as yet unknown amount, and is denoted by θ_2 , which gives

$$\theta_{v2} = \theta_2(1 + 0.61(q_v + 0.001)). \quad (1.6)$$

In order to conserve θ_v , Equations 1.5 and 1.6 are set equal to each other, giving

$$\theta_1(1 + 0.61q_v) = \theta_2(1 + 0.61(q_v + 0.001)). \quad (1.7)$$

Rearranging Equation 1.7, and substituting an approximate value of $q_v = 0.008 \text{ kg kg}^{-1}$ in the boundary layer, the decrease in potential temperature is calculated as approximately 0.18 K. An example cross section of a moist cylinder is shown in Figure 1.24 for the cylinder centered at $x = 2 \text{ km}$ and $y = 2 \text{ km}$.

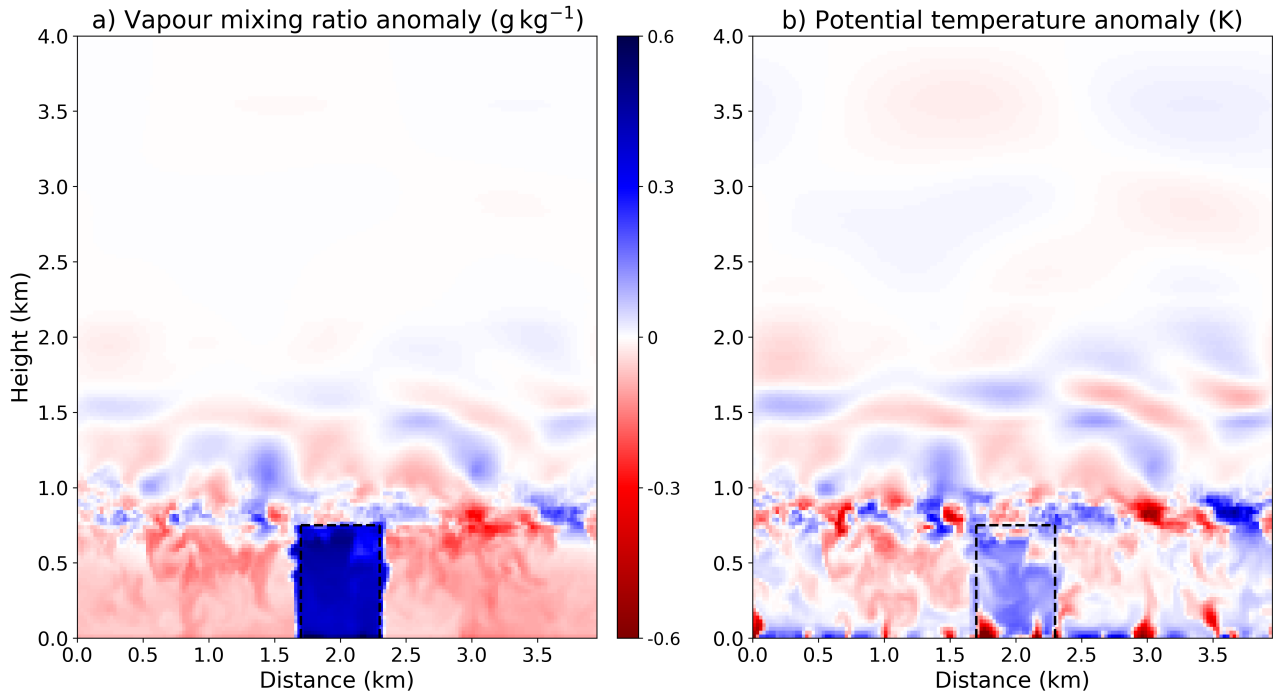


Figure 1.24: Cross sections through a moist cylinder with temperature adjustment at 61 minutes into the simulation, from experiment Single_C_moist. The vapour mixing ratio perturbation from the domain mean is shown in panel (a), measured in g kg^{-1} . The potential temperature perturbation from the domain mean is shown in panel (b). The three black dashed lines show the boundary of the cylinder. Note that these fields are shown one minute after the introduction of the moist cylinder.

The effects of this boundary layer moistening on cloud evolution are shown in Figure 1.25 for the patch centered at $x = 2\text{km}$, $y = 2\text{km}$. Increasing the CBL moisture directly over the localised surface flux produces a cloud earlier, in response to the lowered lifting condensation level. The resulting cloud has a larger mass flux, larger liquid water content, wider cloud base area and reaches a greater height than the cloud produced by the flux alone. The same behaviour is observed for the other four flux/cylinder locations (see Appendix B for figures.)

The addition of a moist cylinder locally increases the moist static energy E of the boundary layer. The total change in E is a result of changes in both latent and sensible heat, as a response to the moistening and cooling respectively. The change in latent heat Q_L is defined as

$$\Delta Q_L = \int_V \rho \Delta q_v L_v dV \quad (1.8)$$

Here, ρ is air density, Δq_v is the increase in water vapour mixing ratio and L_v is the latent heat of vaporisation of water (defined as approximately $2.5 \times 10^6 \text{ J kg}^{-1}$

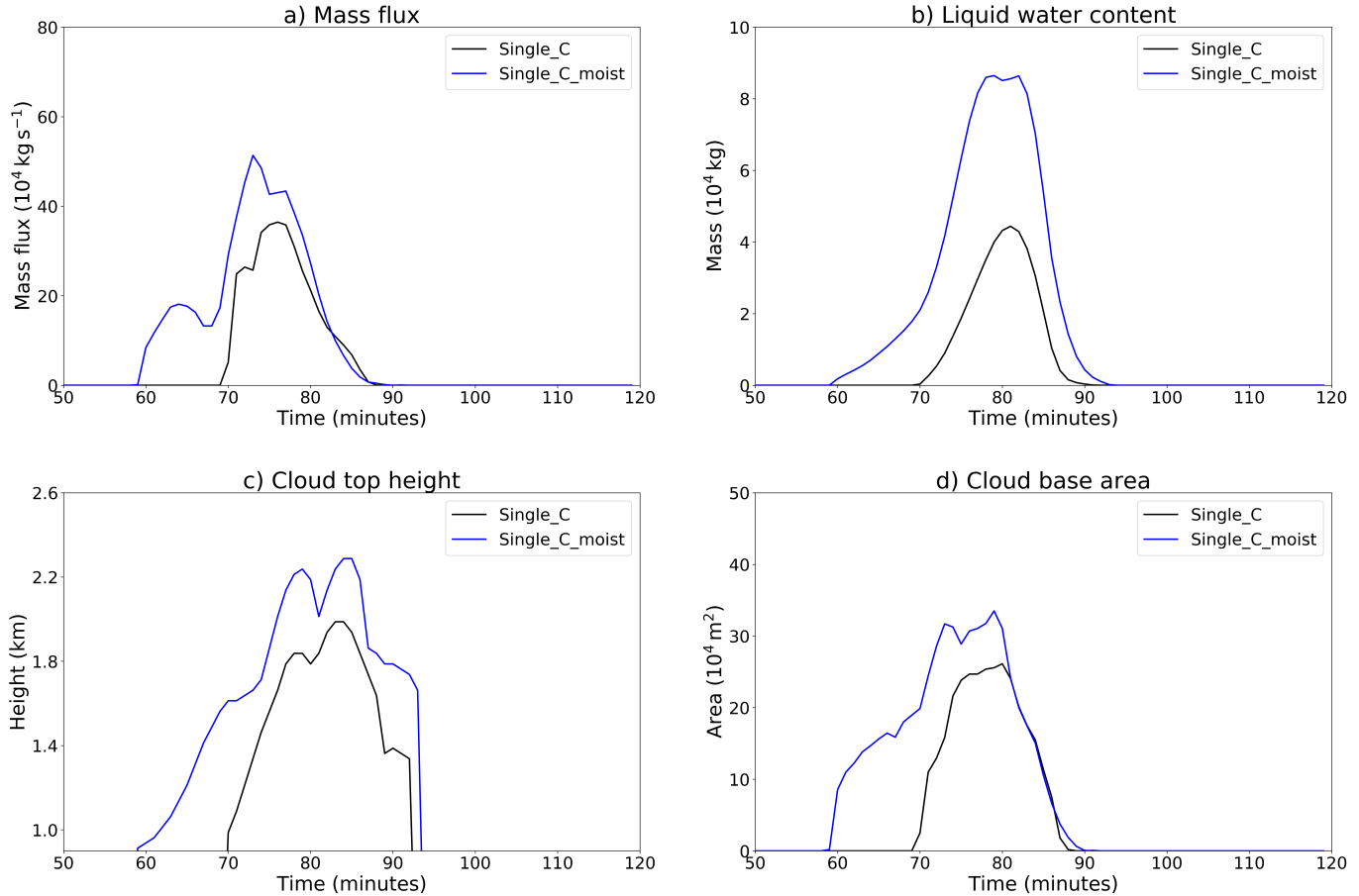


Figure 1.25: Evolution of (a) cloud base mass flux, (b) cloud liquid water content, (c) cloud top height and (d) cloud base area for Single_C (black lines) and Single_C_moist (blue lines).

in MONC). The integrand is the increase in latent heat per grid box, therefore the total increase in CBL latent heat is calculated by integrating over the volume V of the cylinder. Substituting $q_v = 0.001 \text{ kg kg}^{-1}$ and $\rho = 1.1 \text{ kg m}^{-3}$ (the mean air density in the boundary layer) into Equation 1.8, the increase in latent heat is approximately $7.9 \times 10^{11} \text{ J}$.

The change in sensible heat from the temperature reduction in the cylinder is likewise calculated as

$$\Delta Q_S = \int_V \rho c_p \Delta T dV, \quad (1.9)$$

where ΔT is the increase in temperature per grid box and c_p is the specific heat capacity of air ($1005 \text{ J kg}^{-1} \text{ K}^{-1}$). Substituting an approximate value of $\Delta T = -0.18 \text{ K}$, Equation 1.9 results in a sensible heat decrease of $5.6 \times 10^{10} \text{ J}$. The total change in moist static energy is then given by

$$\Delta E = \Delta Q_L + \Delta Q_S = 7.3 \times 10^{-11} \text{ J}. \quad (1.10)$$

The additional boundary layer energy means that air parcels entering cloud base in Single_C_moist are more energetic than those in Single_C. Figure 1.26(a) shows that on average, a grid cell at cloud base five minutes after circular flux initiation experiences an increase in updraft strength by around 0.23 m s^{-1} . Panels (b) and (c) should be ignored for now, but will be referred back to in Section 1.2.3. These more energetic parcels entering cloud base could partly account for the increased mass flux and cloud top height observed in model run Single_C_moist.

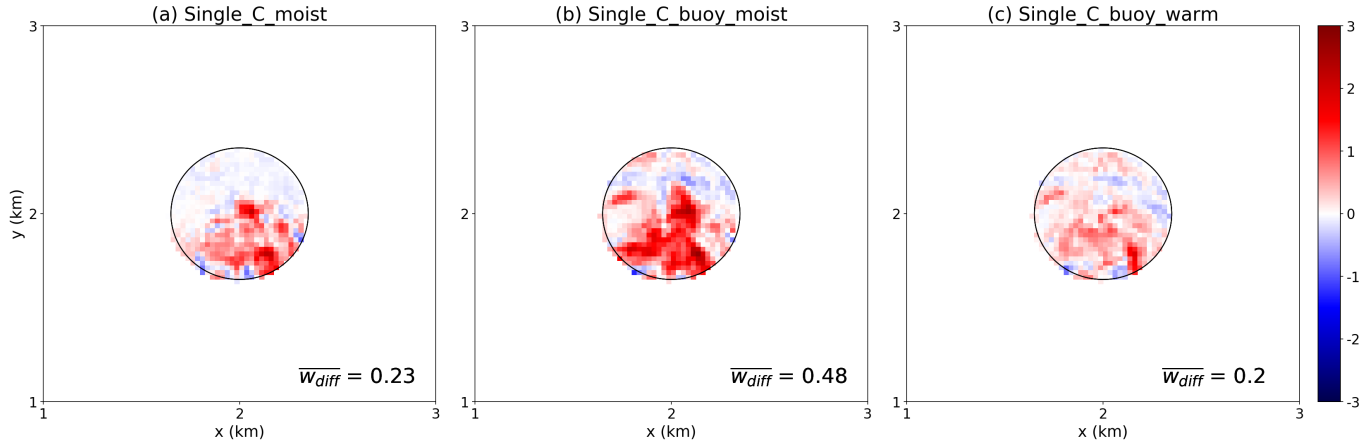


Figure 1.26: The three show the difference in vertical velocity (in $m s^{-1}$) at cloud base between model runs (a) *Single_C_moist*, (b) *Single_C_buoy_moist* and (c) *Single_C_buoy_warm*, as compared to cloud base vertical velocity in reference simulation *Single_C*. Positive values of w_{diff} therefore denote grid cells with increased vertical velocity compared to grid cells in model run *Single_C*. The difference in vertical velocity is calculated five minutes after the main circular flux is initiated, and is denoted by w_{diff} . The mean value of w_{diff} ($\overline{w_{diff}}$) is shown in the bottom right corner of each panel.

Another factor that has already been shown to influence cloud evolution is cloud base area, which is larger for simulation *Single_C_moist*. This is unsurprising, since the additional moisture results in a greater proportion of air parcels that are close to or already at saturation, and hence more likely to produce cloud droplets. As the horizontal area of a cloud increases, its rate of dilution tends to decrease, owing to the well-established inverse relationship between entrainment and cloud radius (see De Rooy et al., 2013). This cloud dilution mechanism is explored later in Section 1.2.3.

Integrated boundary layer buoyancy

Figure 1.27 shows the difference in \widehat{B} (a) across each quadrant and (b) above each patch for simulation *Multi.REF*. There is very little variation in the spread and peak of \widehat{B} across each quadrant. The four distributions are all positively skewed and unimodal, and have a negative modal value; however these large regions of negative buoyancy are balanced by smaller regions of comparatively stronger positive buoyancy, in the form of convective updrafts.

In contrast to the quadrants, the distributions of \widehat{B} across the four patches are slightly more varied. The overall spread of values is similar to the spread across each quadrant; however, there is now more variation in the modal value. Additionally, while the distributions across patches TL, BL and BR remain uni-

modal, the distribution across patch TR is now bimodal, exhibiting a secondary smaller, positive peak. In fact, more than half of the data points over patch TR now have a positive value of \hat{B} , suggesting that vertical motion may be enhanced in this region.

Table 1.1: Fraction of boundary layer with positive integrated buoyancy \hat{B} (a) in each quadrant and (b) above each patch.

	(a) Quadrant	(b) Patch
TL	0.45	0.32
TR	0.40	0.54
BL	0.34	0.47
BR	0.41	0.25

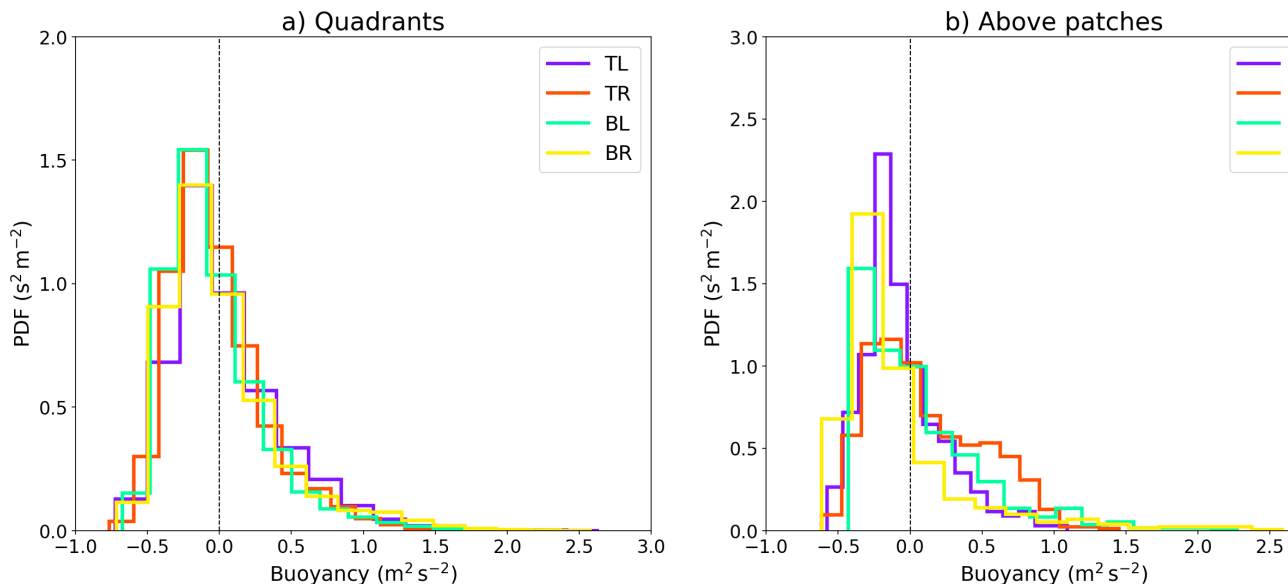


Figure 1.27: Distribution of integrated boundary layer buoyancy from Multi_REF across (a) each quadrant and (b) each circular patch, taken at the end of the spinup period.

As with \widehat{W}_v , the mean \hat{B} anomaly for each of the 12 sample clouds is plotted against the maximum cloud base area, and shown in Figure 1.28. Masking the boundary layer directly above the circular patches indicates positive relationships between average \hat{B} anomalies and cloud base area, as well as the fractional boundary layer area with a positive \hat{B} anomaly and cloud base area. The coefficient of determination r^2 is (a) 0.48 and (b) 0.29, indicating that the buoyancy anomalies in the CBL explain almost half of the variation in maximum cloud base area,

and that the size of these anomalies is more important than the fractional area with a positive anomaly. These positive correlations are not replicated when the boundary layer is masked below maximum cloud base area, which means it may be difficult to test these relationships in a more realistic situation, such as a large cloud population generated by homogeneous surface fluxes.

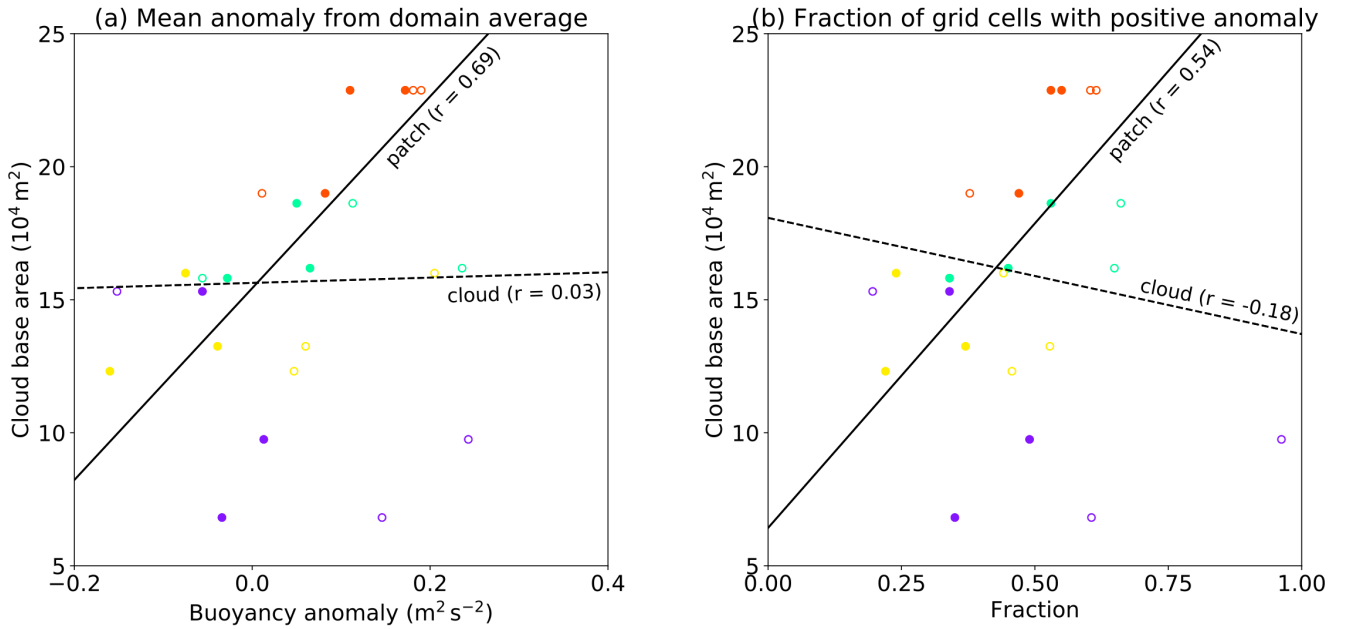


Figure 1.28: Scatterplots of (a) mean integrated boundary layer buoyancy (\hat{B}) anomaly and (b) fraction of grid cells with a positive \hat{B} anomaly, both calculated at $t = 60$ minutes, against maximum cloud base area attained over the lifetime of each cloud. The boundary layer has been masked both above the circular patches (denoted by filled circles) and underneath the maximum cloud base area of the four clouds (unfilled circles). Linear regressions and corresponding r values are also shown (solid line is for patches, dashed line is for clouds.)

Since buoyancy is a measure of both moisture and temperature, the relationship to cloud base area may be controlled by either one or both of these factors. It is therefore important to calculate the relative importance of these factors to maximum cloud base area. The relationship between boundary layer buoyancy and cloud development can be explored further using idealised LES, as was previously done with boundary layer water vapour path. Five simulations are run, identical in setup to the five Single_X_moist model runs, but now the temperature inside the cylinder is not adjusted. This results in a buoyancy increase within the bounds of the cylinders, and an increase in moist static energy in the form of latent heat Q_L , given by Equation 1.8 and calculated as $\sim 7.9 \times 10^{11}$ J. These five simulations are referred to as Single_X_buoy_moist, where X denotes patch

location and ‘moist’ references the fact that buoyancy is increased through additional moisture. A description of these five model runs is given in Table ??, Appendix A.

A further five simulations are run, this time replacing moist cylinders with warm cylinders that have the same buoyancy profile as the moist cylinders. The increase in sensible heat within the cylinder is again given by Equation 1.9 where ΔT is now an unknown quantity.

Since the buoyancy increase in a moist cylinder versus its warm counterpart is identical, this means that the virtual temperature T_v of both cylinder are equal. This gives

$$T(1 + 0.61(q_v + \Delta q_v)) = (T + \Delta T)(1 + 0.61q_v). \quad (1.11)$$

Let us now consider a single grid box within these cylinders. Rearranging and substituting $\Delta q_v = Q_L/mL_v$ and $\Delta T = Q_S/c_p m$ (where m is the mass of the cylinder), Equation 1.11 becomes

$$\frac{Q_L}{Q_S} = \frac{L_v(1 + 0.61q_v)}{0.61 c_p T}. \quad (1.12)$$

An average grid cell in the CBL at the end of spinup has $q_v = 0.008 \text{ kg kg}^{-1}$ and $T = 284 \text{ K}$. Substituting these values into Equation 1.12 gives a ratio of $Q_L/Q_S \sim 14$, resulting in an average $Q_S = 5.6 \times 10^{10} \text{ J}$. This means that, for a given buoyancy increase, additional moisture will result in a much larger increase in moist static energy than additional heating.

These five simulations are referred to as Single_X_buoy_warm, where X denotes patch location and ‘warm’ references the fact that buoyancy is increased through additional heating. An example of a cross section through (a) a warm cylinder and (c) a corresponding moist cylinder is shown in Figure 1.29 for model run Single_C_buoy_warm. The respective buoyancy cross sections, shown in (b) and (d), are identical within the bounds of the cylinder (the dashed lines).

There are now five pairs of simulations, in which integrated boundary layer buoyancy \widehat{B} is increased through two separate mechanisms: increased moisture and increased heat. The effect of these two mechanisms on cloud evolution for a single pair of simulations is shown in Figure 1.30, along with the results from Single_C and Single_C_moist for comparison. Corresponding plots for other flux/cylinder locations can be found in Appendix B.

An increase in \widehat{B} results in earlier formation of cloud, an effect which is replicated in the other four pairs of simulations - this is due to boundary layer air parcels gaining additional energy, giving them more momentum to overcome the negatively buoyant CIN layer and reach the LCL earlier. It is expected that increasing buoyancy through additional moisture would result in earlier cloud initiation than through additional heating, since the LCL in the former case is lowered and the air parcels are more energetic, however this only occurs in two of the five simulations.

An increase in \widehat{B} consistently results in wider, taller clouds that transport more mass vertically. Greater CBL buoyancy increases the likelihood of air parcels reaching the LCL and condensing, thereby producing a wider cloud base. Wider clouds are able to transport more mass vertically and, because the entrainment rate into their cores is reduced, are able to reach greater heights. The overall increase in cloud size and vertical transport is consistently more pronounced when buoyancy is increased via additional moisture, which can be explained by two mechanisms. The first is that boundary layer air parcels in the moist simulations gain a greater amount of energy than those in the warm simulations. The second is that the increase in boundary layer water vapour increases the potential for latent heat release, providing additional buoyancy to the resulting cloud.

The relative effects of increased CBL buoyancy on cloud development are quantified by calculating the total latent heat released by the cloud. This is approximated by multiplying the maximum cloud liquid water mass (in kg) with the latent heat of vaporisation of water (in J kg^{-1}). The results are given in Table 1.2.

Table 1.2 shows that increasing boundary layer buoyancy consistently results in an increase in latent heat released by the cloud, an effect that is consistently more pronounced when buoyancy is increased via additional moisture rather than heat. However, recall that a moist cylinder provides approximately $7.9 \times 10^{11} \text{ J}$ additional moist static energy, whereas a warm cylinder with identical buoyancy increases moist static energy by approximately $5.6 \times 10^{10} \text{ J}$. With respect to the additional energy imparted to the system, the increase in latent heat release by

Table 1.2: The first column lists each circular patch location by its (x,y) centre coordinates in km. The second, third and fifth columns are the cloud latent heat (LH) release in Joules for the flux-only, moist cylinder and warm cylinder simulations. The third and fifth columns also include (in brackets) the increase in LH from the corresponding flux-only simulation. The fourth and sixth columns give this LH increase as a percentage of additional input energy via the moist (7.9×10^{11} J) or warm (5.6×10^{10} J) cylinders.

Location	LH - flux only	LH - moist cylinder	NLH increase as a % of input	LH - warm cylinder	NLH increase as a % of input
(2,2)	1.1×10^{11}	5.0×10^{11} ($3.9 \times 10^{11} \uparrow$)	49%	3.8×10^{11} ($2.7 \times 10^{11} \uparrow$)	482%
(1,1)	4.1×10^{10}	3.0×10^{11} ($2.5 \times 10^{11} \uparrow$)	32%	2.7×10^{11} ($2.3 \times 10^{11} \uparrow$)	411%
(1,3)	4.2×10^{10}	3.8×10^{11} ($3.3 \times 10^{11} \uparrow$)	42%	2.4×10^{11} ($2.0 \times 10^{11} \uparrow$)	357%
(3,1)	6.3×10^{10}	4.1×10^{11} ($3.4 \times 10^{11} \uparrow$)	43%	2.0×10^{11} ($1.3 \times 10^{11} \uparrow$)	232%
(3,3)	1.3×10^{11}	4.5×10^{11} ($3.1 \times 10^{11} \uparrow$)	41%	3.6×10^{11} ($2.3 \times 10^{11} \uparrow$)	411%

the clouds in the warm cylinder simulations is a factor of 10 larger, whereas the increase in the moist cylinder simulations is less than half of the initial input. Therefore increasing boundary layer buoyancy results in a comparatively larger increase in cloud latent heat release if the buoyancy is increased via additional heat instead of moisture.

Dilution of cloud core

It is desirable to assess how the rate of cloud dilution varies between the idealised cylinder model runs in Sections 1.2.3 and 1.2.3. A dimensionless surface tracer flux with a value scaled to $1.0 \text{ m}^{-2} \text{ s}^{-1}$ is initialised in the following simulations:

- Single_C
- Single_C_moist
- Single_C_buoy_moist
- Single_C_buoy_warm

The tracer scales in time and space with the circular patches of increased sensible and latent heat fluxes. The surface tracer mixes with the boundary layer air, and some of it is transported into the cloud layer through thermals and turbulent motions. The movement of the tracer is visualised in Figure 1.31, which shows the relationship between tracer concentration (in black contours) and cloud liquid water (in blue shading). Five minutes after tracer initiation, the tracer rises with the thermal through the CBL. After ten minutes, some of the tracer is transported into the cloud layer. Panels (c) and (d) show the formation of cloud, and the

areas of highest liquid water content are observed to coincide with the areas of highest tracer concentration. It is possible to connect these regions of high liquid water content backwards into the sub-cloud layer by following the tracer contours. Tracer concentration is therefore a useful tool to visualise an area of cloud, and to connect the cloud to boundary layer structures.

Domain-mean tracer concentration The evolution of domain-mean tracer for the Single_C model run is shown in Figure 1.32. The high tracer concentration at the surface persists between 60-70 minutes as the tracer flux is continually released. Buoyant air rises, transporting the region of higher tracer concentration away from the surface. As the rising air meets the stable region at the top of the CBL, some of the tracer spreads laterally outwards forming the region of high concentration observed around z_c . Some tracer enters the cloud layer, and is transported upwards in the cloud as it rises. Eventually the cloud overshoots the level of neutral buoyancy. As the cloud begins to evaporate, the remaining tracer concentration is detrain into the environment around $z = 1500\text{m}$.

Figure 1.33 shows the variation in domain-mean tracer concentration between the single flux model run and the corresponding simulations with moist or buoyant cylinders. The two detrainment layers observed in Figure 1.32 are clearly replicated at similar heights in the model runs with additional moisture or buoyancy, however there is increased variation in the relative tracer concentrations. Simulations with additional boundary layer moisture or buoyancy produce more energetic thermals, which transport greater tracer concentrations upwards to the higher detrainment layer. This effect is most pronounced in Single_C_buoy_moist, the model run with the largest boundary-layer energy increase. Figure 1.26 shows the various increases in updraft strength at cloud base for simulations with moist or buoyant cylinders, which is greatest for Single_C_buoy_moist.

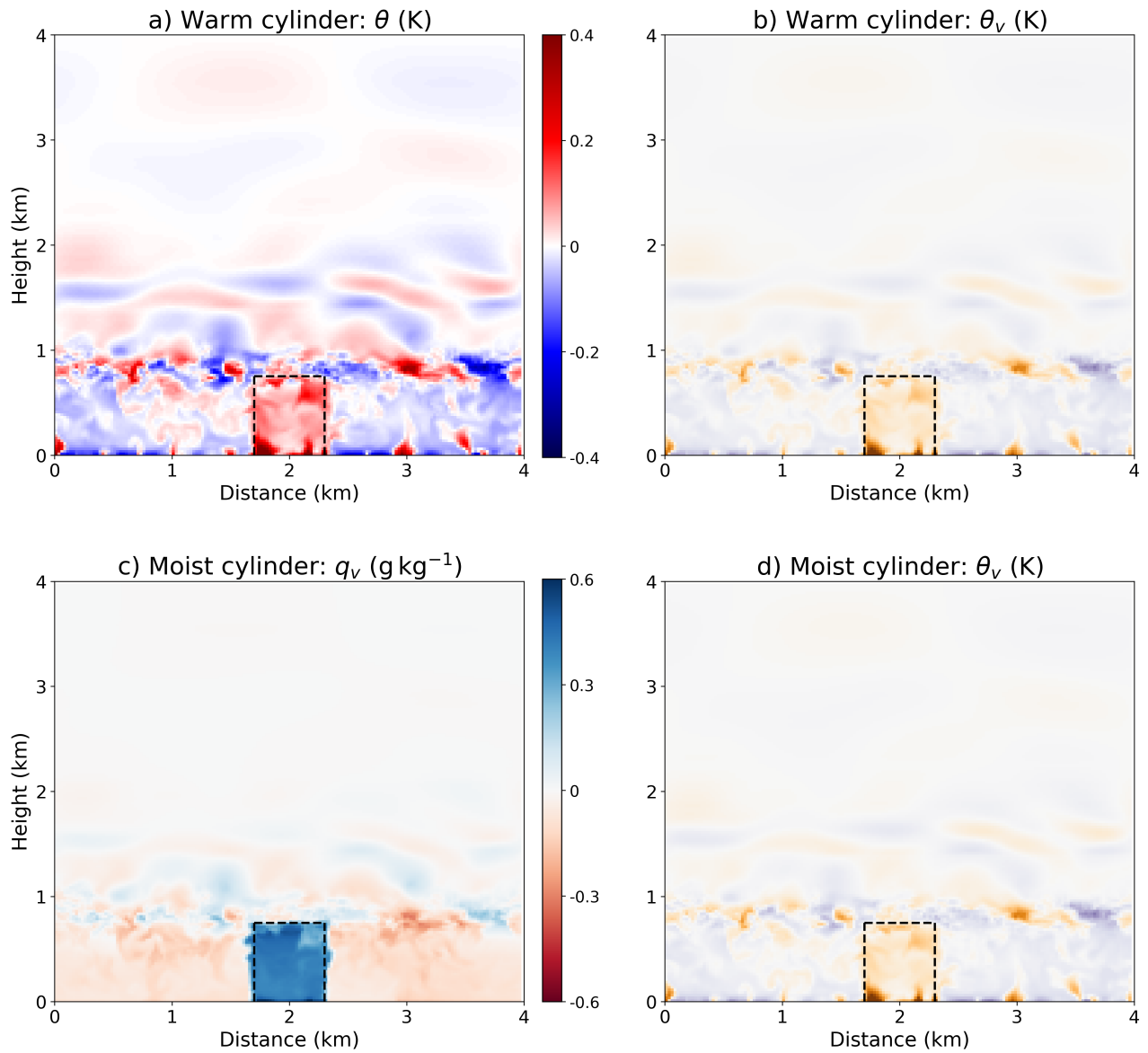


Figure 1.29: *X-Z cross sections through the centre of the cylinders for model runs Single_C_buoy_warm (top row) and Single_C_buoy_moist (bottom row), taken at the first model output time that they appear (61 minutes). The cylinders are bounded by the three black dashed lines. Panels (a) and (c) show the perturbations in potential temperature and water vapour mixing ratio respectively. Panels (b) and (d) show the resulting perturbations in θ_v (a proxy for buoyancy), which have increased by an identical amount in both cases.*

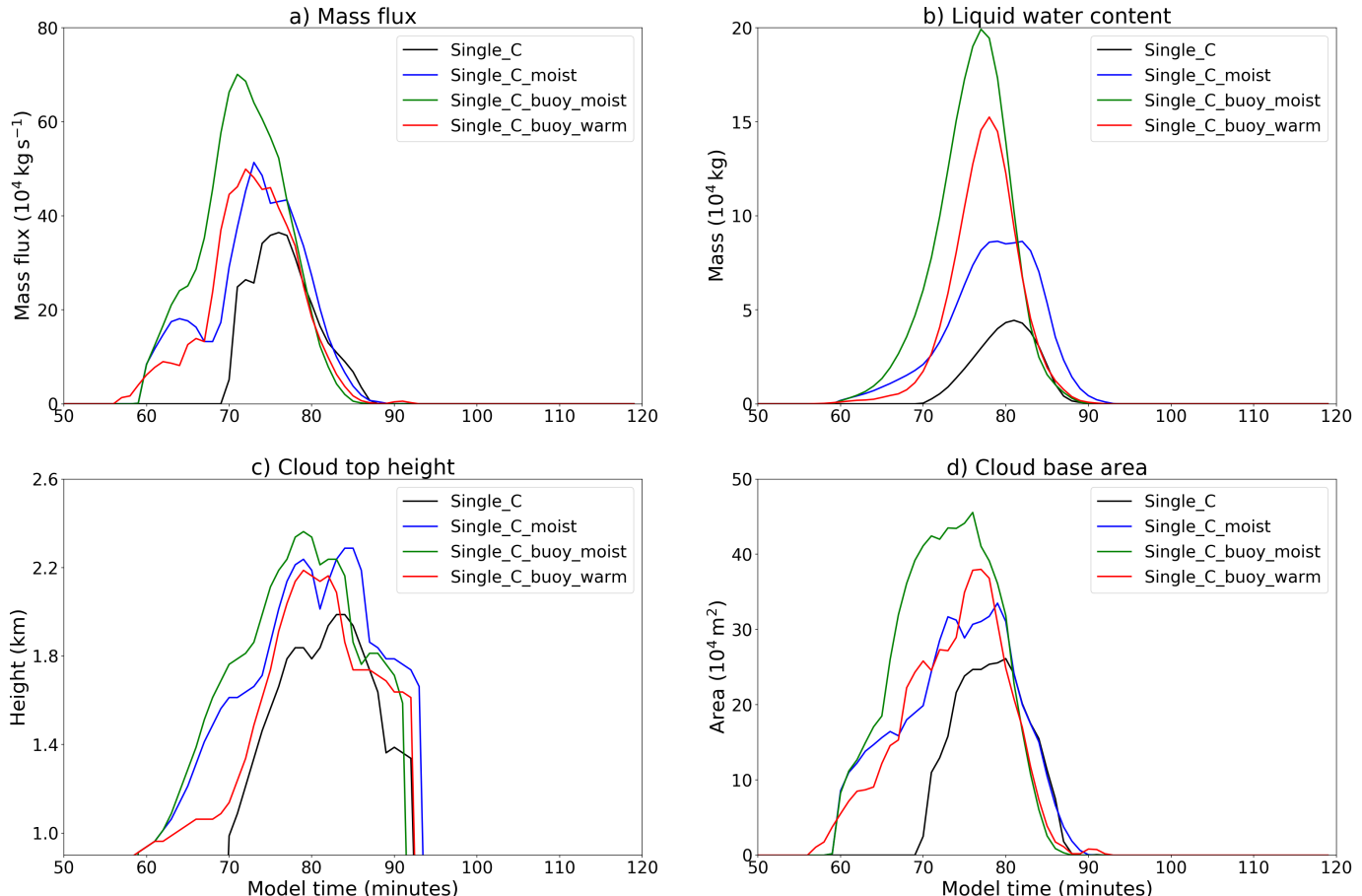


Figure 1.30: Results for model runs with a single circular patch. Plot shows evolution of (a) cloud base mass flux, (b) cloud liquid water content, (c) cloud top height and (d) cloud base area for Single_C (black lines), Single_C_moist (blue lines), Single_C_buoy_moist (green lines) and Single_C_buoy_warm (red lines).

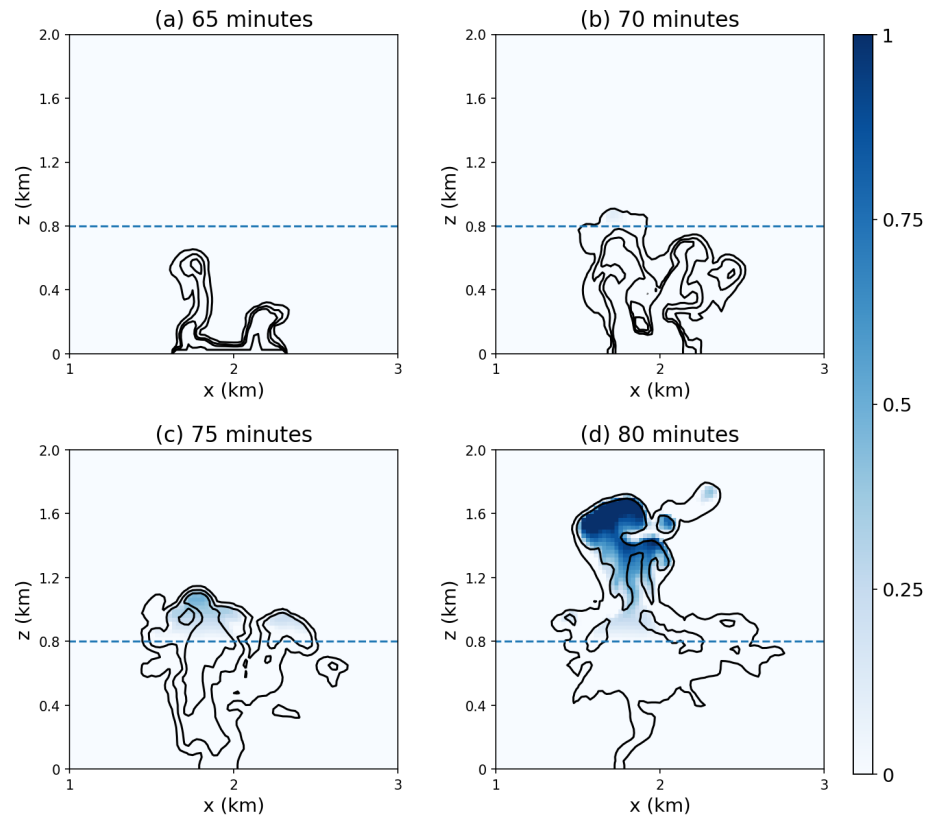


Figure 1.31: Cross section of tracer concentration and cloud liquid water, along the transect $y = 2\text{km}$, taken at (a) 65, (b) 70, (c) 75 and (d) 80 minutes into the Single_C simulation. The black contours are tracer concentration at intervals of 0.1, 0.5, 1.0 and 5.0. The blue shading is liquid water mixing ratio (in g kg^{-1}). The blue horizontal dashed line denotes the approximate level of cloud base.

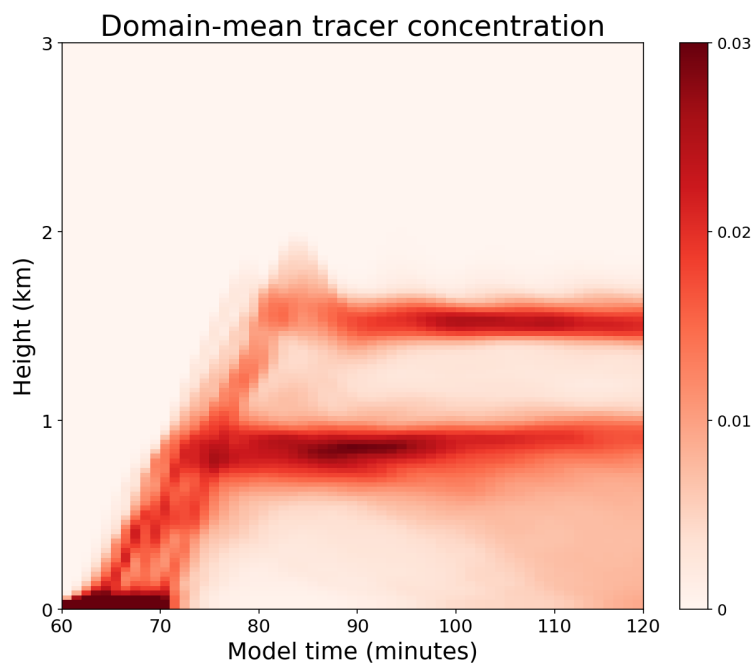


Figure 1.32: Horizontally-averaged domain tracer concentration between 60 and 120 minutes.

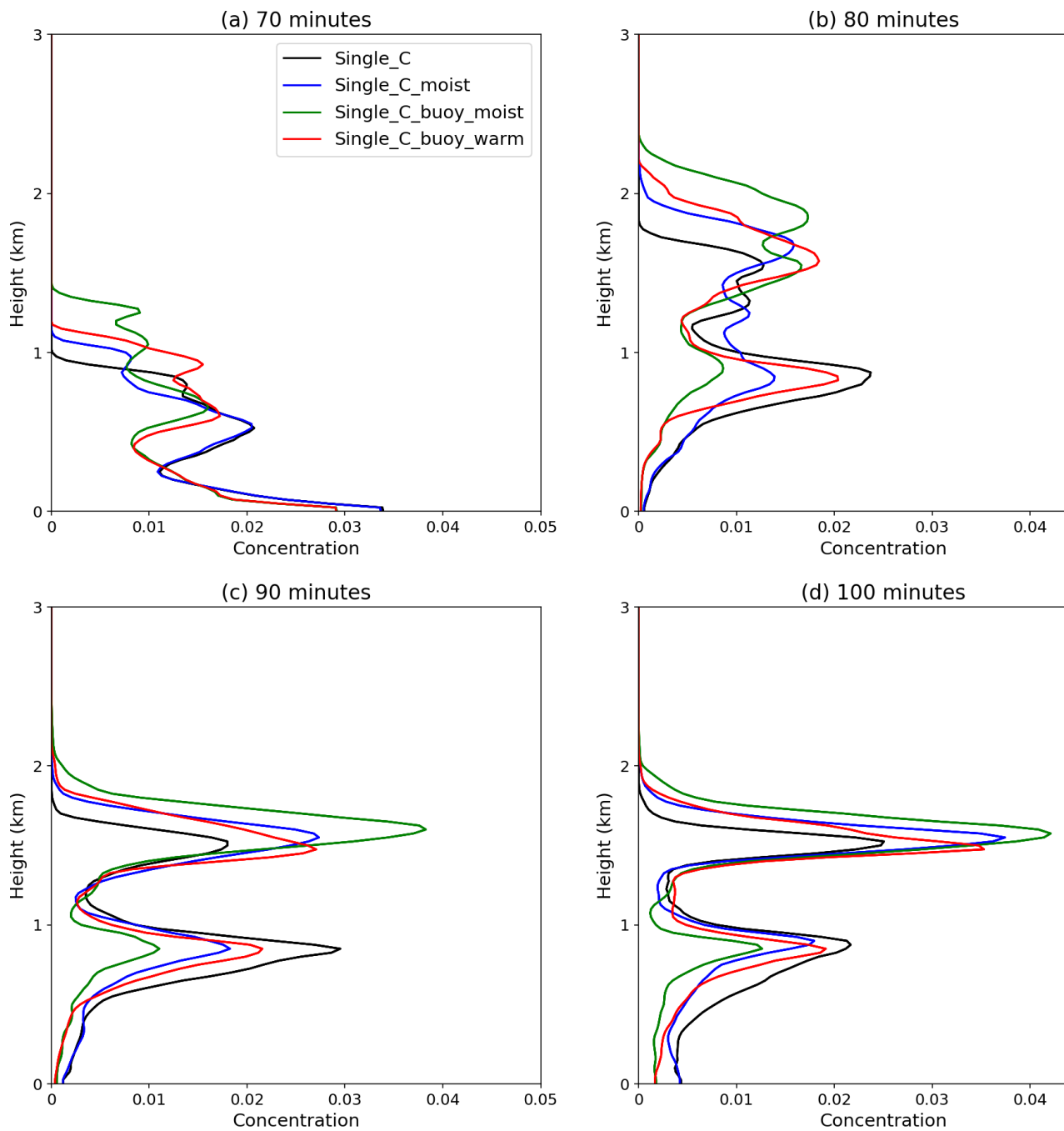


Figure 1.33: Profiles of horizontally-averaged domain tracer concentration at (a) 70 minutes, (b) 80 minutes, (c) 90 minutes and (d) 100 minutes.

In-cloud tracer concentration The dilution of a cloud may be characterised by some measure of tracer concentration (γ) decrease inside the cloud core. The cloud core here is defined as the region in which purity tracer concentration $p > 10^{-3}$, liquid water specific humidity $q_c > 10^{-5}\text{kg kg}^{-1}$ and vertical velocity $w > 0.5\text{m s}^{-1}$.

A vertical profile of self-weighted cloud core tracer concentration ($\tilde{\gamma}$) at a single timestep t is defined as

$$\tilde{\gamma}(z, t) = \frac{\overline{\gamma_c(x, y, z, t)^2}}{\overline{\gamma_c(x, y, z, t)}}. \quad (1.13)$$

Here, γ_c is the tracer concentration inside the cloud core, and is found by masking the tracer field over the relevant regions. Using γ_c^2 in the numerator gives a greater weighting to higher values. The evolution of $\tilde{\gamma}$ can be used as a metric of mean cloud core tracer concentration in order to infer cloud dilution. Figure 1.34(a) shows the cloud core concentration at cloud peak time using the metric $\overline{\tilde{\gamma}^2}/\overline{\tilde{\gamma}}$. Differences between simulations are observed, implying that there are differences in mean tracer concentration; however it is also interesting to observe differences in extreme values as well as the mean.

Increasing the power of both the numerator and denominator in Equation 1.2.3 by the same amount gives a greater weighting to regions of higher tracer concentration. Panel (b) shows cloud core concentration using the metric $\overline{\tilde{\gamma}^4}/\overline{\tilde{\gamma}^3}$. As the power terms are increased towards infinity, Equation effectively selects the grid box with the highest tracer concentration. This is sometimes referred to as the ‘least diluted parcel’ or LDP, and the corresponding curves are shown in panel (c). In the bottom third of the cloud layer, the maximum and mean tracer concentrations are similar, however the differences between the curves becomes magnified. This implies that the variety in LDPs is larger than the variety between the average tracer concentrations. In the top third of the cloud layer, the mean tracer concentration for Single_C_buoy_warm is much greater than for Single_C_buoy_green, however the concentration of the LDP in the latter is greater than the former. Measurements of both the mean and maximum tracer concentration are therefore useful when it comes to analysing differences in cloud dilution.

The dilution of a cloud is determined by large-scale (dynamical) and small-scale (turbulent) mixing between the cloud and the environment. The rate of dynamical mixing is commonly defined as inversely proportional to the cloud radius, therefore cloud core radius is a useful metric for determining regions of increased

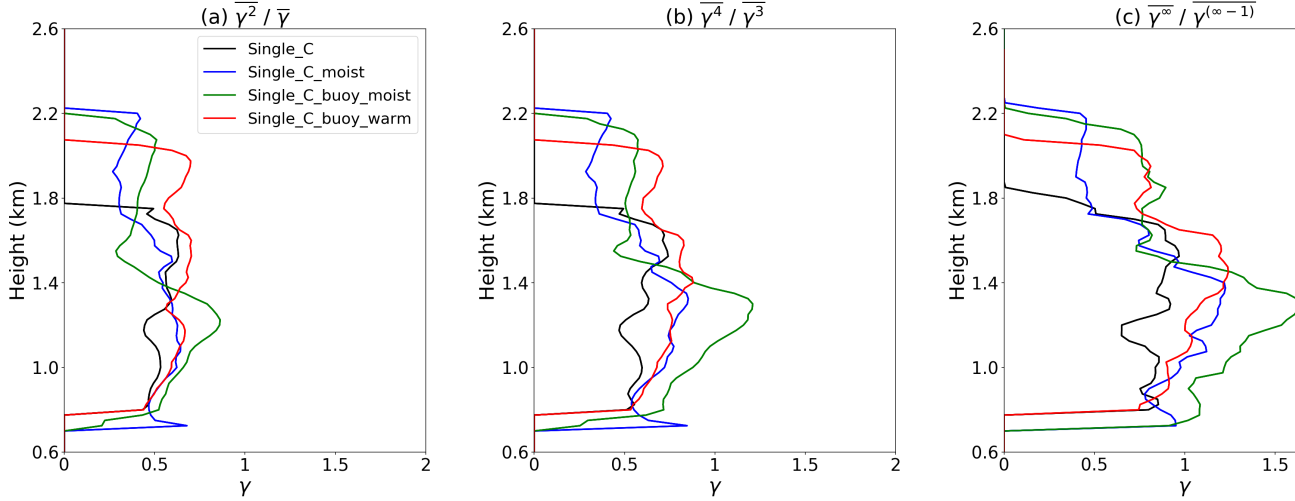


Figure 1.34: Tracer concentrations at cloud ‘peak’ time using three different metrics: (a) $\bar{\gamma}^2 / \bar{\gamma}$, (b) $\bar{\gamma}^4 / \bar{\gamma}^3$ and (c) $\bar{\gamma}^\infty / \bar{\gamma}^{(\infty-1)}$, i.e. the least diluted parcel (LDP).

dilution. Since these clouds do not have a uniformly circular cross section, an effective radius r_e is defined as

$$r_e = \sqrt{\frac{a}{\pi}},$$

where a is the cloud core cross-sectional area.

Turbulent mixing at the cloud boundary also leads to dilution of the cloud. A useful metric to diagnose such mixing is the turbulent kinetic energy (TKE) in the cloud shell. TKE is defined as:

$$\frac{1}{2} \times \left((u_s')^2 + (v_s')^2 + (w_s')^2 \right) \quad (1.14)$$

where u_s , v_s and w_s are the x , y and z components of the momentum vector over the cloud shell, and prime terms denotes a deviation from the horizontal mean. TKE therefore has units of $\text{m}^2 \text{s}^{-2}$. Since the focus is on lateral mixing, vertical fluctuations in the shell are irrelevant and therefore the third term in the brackets in Equation 1.14 may be ignored.

Figure 1.35 shows the cloud core tracer concentration (as measured by both the mean and maximum) during three phases of the cloud lifecycle, along with the corresponding time frames of cloud core effective radius and cloud shell horizontal TKE. The black curves (Single-C) are the baseline by which the other three curves are compared. During the growing phase of a cloud, the black curves in panel (a) show that cloud core tracer concentration is initially greatest near cloud base and generally decreases with height away from the source. Over time, the tracer

is mixed vertically through the atmosphere; it is also laterally mixed into the environment, partly due to turbulent mixing at the cloud edges and partly due to dynamic entrainment and detrainment. As cloud evolution progresses, the profiles of mean and maximum $\tilde{\gamma}$ become more homogeneous with height as the cloud layer becomes well mixed, and the variation between the mean and maximum $\tilde{\gamma}$ decreases.

Additional boundary layer moisture (blue curve, Single_C_moist) results in a lowered LCL. During the growing phase of the blue cloud, both its mean and maximum $\tilde{\gamma}$ show only subtle differences compared to the black cloud. As the cloud begins to peak, the blue cloud has grown in size relative to the black cloud, which would be expected to result in higher $\tilde{\gamma}$ - both the mean and the maximum $\tilde{\gamma}$ profiles are slightly increased for the blue cloud. By the time both clouds are decaying, despite the fact that the blue cloud is still much larger than the black cloud, both the mean and maximum $\tilde{\gamma}$ are extremely similar to the black cloud. This is due to the fact the blue cloud shell TKE increased by a large amount during its lifetime, aiding its dilution through turbulent entrainment.

Clouds resulting from additional boundary layer buoyancy (green curve, Single_C_buoy_moist; and red curve, Single_C_buoy_warm) initially result in both a higher mean and maximum $\tilde{\gamma}$ compared to the black cloud. Both the red and the green cloud are larger and exhibit more cloud shell TKE than the black cloud, and this effect is generally more pronounced for the green cloud. During the growing phase of the clouds, up to around 1.2km, the cloud shell TKE is similar for both red and green clouds; however, the green cloud is slightly larger than the red cloud, and therefore the dilution of the red cloud is greater than the green. Above 1.2km however, although the green cloud remains larger than the red, its cloud shell TKE becomes so great that it begins to dilute at a faster rate than the red cloud, as shown by a reduced mean and maximum $\tilde{\gamma}$ compared to the red cloud. By the time both clouds are decaying, even though the green cloud is still much larger than the red cloud, it has diluted by a similar amount due to its increased shell TKE.

The overall picture seems to be one of energetic boundary layer thermals initially punching through the CIN layer with more ease and forming cloud which initially grows at a rapid rate compared to a baseline case; however, the initial increase in cloud size and energy is eventually offset by the diluting effects of increased turbulence at its edges, resulting in similar cloud lifetimes across all simulations.

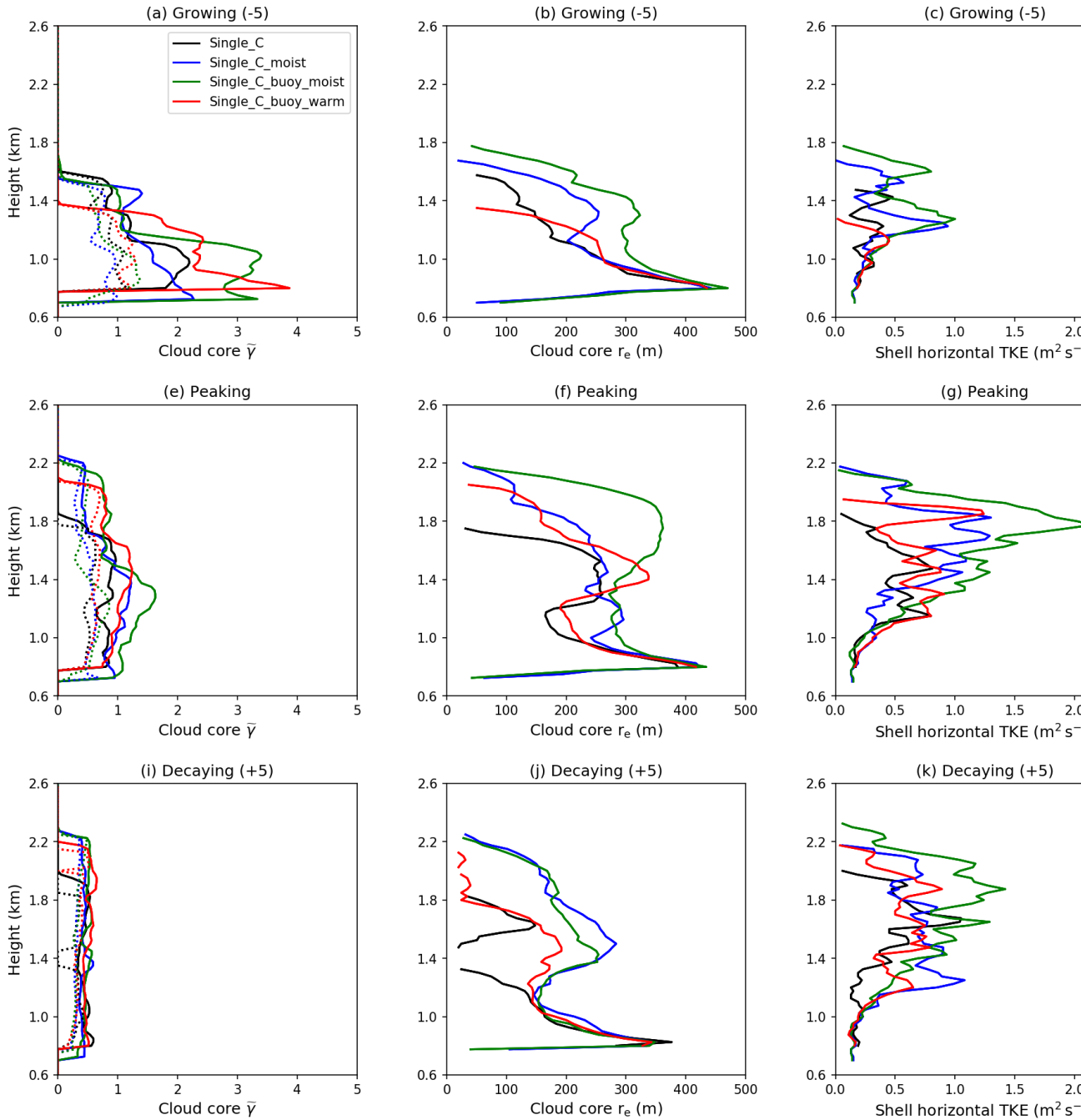


Figure 1.35: Profiles of (first column) cloud core tracer concentration $\bar{\gamma}$ (self-weighted), (second column) cloud core effective radius and (third column) cloud shell sub-grid horizontal turbulent kinetic energy. The middle row corresponds to the peak time of each cloud, defined as the time in which total cloud liquid water reaches its maximum; the top and bottom row ('growing' and 'decaying') correspond to -5/+5 minutes either side of this peak time respectively. The tracer concentration is defined both using $\bar{\gamma}_c^2/\bar{\gamma}_c$ (dotted lines) and the least diluted parcel (solid lines).

Boundary layer vertical velocity

The sensible surface heat flux during spinup produces thermals that accelerate upwards through the CBL. As they approaches the stable, negatively buoyant region above the CBL, the thermals begin to decelerate. Research by Couvreux et al. (2010) found that thermals have a maximum vertical velocity close to the middle of the boundary layer. The height at which the thermals in Multi_REF attain maximum vertical velocity is found by plotting the profile of mean vertical velocity variance. The variance is used instead of the mean value, as conservation of momentum dictates that horizontal-mean w will be zero at each model level. The variance of w , σ_w^2 , at a single horizontal model level is defined as

$$\sigma_w^2 = \frac{1}{N} \sum_{n=0}^N (w - \bar{w})^2, \quad (1.15)$$

where \bar{w} is the horizontal mean of w , and N is the number of grid boxes in a horizontal cross section. σ_w^2 therefore has units of $\text{m}^2 \text{s}^{-2}$.

Figure 1.36 shows the profile of horizontally-averaged σ_w^2 at the end of model spinup, with a maximum clearly observed around 250m above the surface. This indicates that the updraft speed of boundary layer thermals peak around a third of the way up the boundary layer, in contrast to the results of Couvreux et al. (2010). The vertical velocity field at this level is denoted hereafter as w_{250} .

The distribution of w_{250} at the end of model spinup from simulation Multi_REF is shown in Figure 1.37. There is little variation between quadrants, with the modal value always negative. Since vertical motion is conserved on each model level, these widespread regions of descent must be balanced by more localised regions of stronger ascent. The distributions directly above each patch are more varied than their quadrant counterparts, with the modal values over patches TL and TR becoming more negative and more positive respectively. The area fractions of positive and negative w_{250} values are given in Table 1.3 and show that, while quadrant TR overall experiences more downward than upward motion in the bottom third of the CBL, over 70% of the region directly over the circular patch has positive w_{250} . Quadrant TL experiences more downward than upward motion at this level, and this pattern is amplified directly over the circular patch.

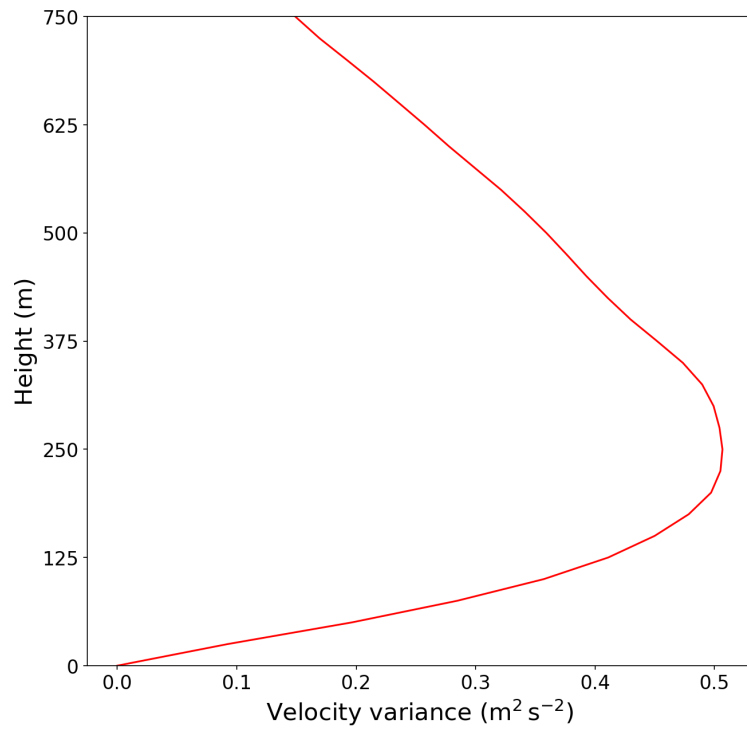


Figure 1.36: Horizontally-averaged vertical velocity variance (in $\text{m}^2 \text{s}^{-2}$) within the boundary layer at the end of model spinup. A maximum is observed at approximately 250m.

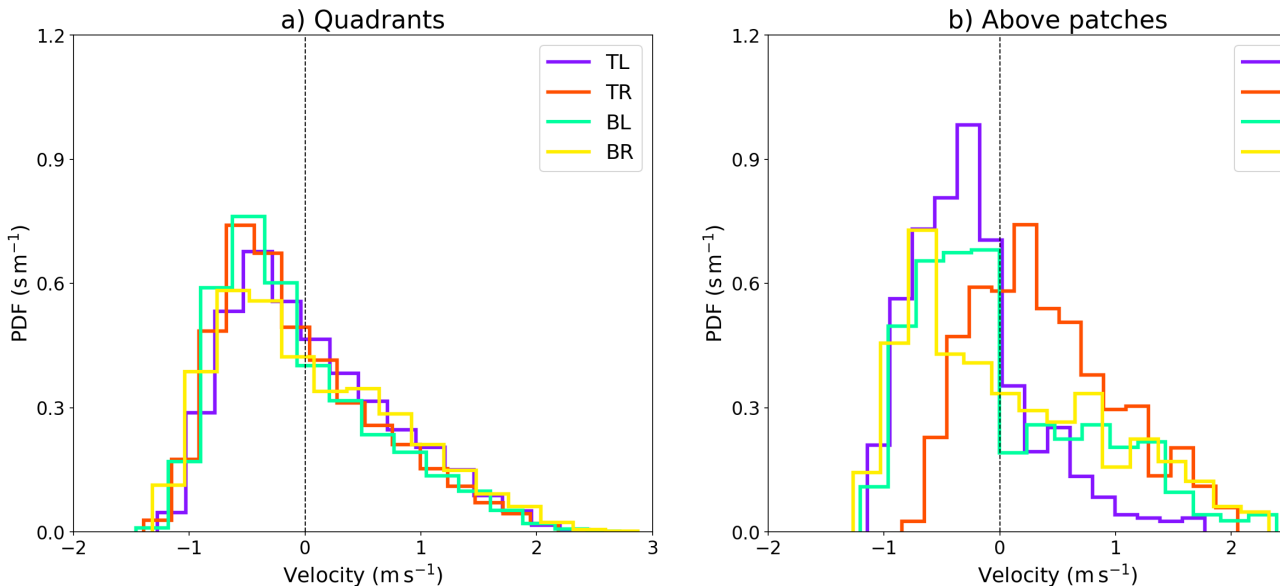


Figure 1.37: Distribution of vertical velocity w at a height of 250m (w_{250}) from Multi_REF across (a) each quadrant and (b) each circular patch, taken at the end of the spinup period.

Table 1.3: Fraction of boundary layer with positive vertical velocity w at a height of 250m (a) in each quadrant and (b) above each patch.

	(a) Quadrant	(b) Patch
TL	0.46	0.24
TR	0.40	0.71
BL	0.37	0.37
BR	0.46	0.46

Relationship to maximum cloud base area Since the horizontal domain average vertical velocity is zero, the w_{250} anomaly from the mean is equal to w_{250} itself. Therefore the mean value \bar{w}_{250} is plotted against maximum cloud base area, and shown in Figure 1.38. There is a strong positive relationship between the updraft strength at 250m directly over the location of surface forcing and maximum cloud base area, which is shown in panel (a) to explain around 65% of the variation in cloud base area. The percentage area with a positive w_{250} is also strongly positively correlated with cloud base area. These two relationships both hold for boundary layer air directly below maximum cloud base area, although the strength of the relationships decreases a little.

These positive correlations suggest that the stronger the updraft in the bottom third of the CBL, the wider and therefore deeper the resulting cloud is expected to be. This can be explained by the fact that a parcel of air with a large upwards momentum is more likely to push through the boundary layer inversion and condense than a parcel with comparatively less momentum. A condensed parcel of air with increased momentum will also travel further vertically upwards before decelerating; it is also less likely to mix with surrounding air (Neggers et al., 2002), and will therefore dilute at a reduced rate.

It is difficult to test these results further using idealised LES methods such as those described in Sections 1.2.3 and 1.2.3, since imposed areas of convergence are handled poorly by the MONC pressure solver. However, since there appears to a positive correlation between updraft strength at 250m directly below cloud and cloud base area, this relationship may be tested more thoroughly using a large population of clouds generated by a homogeneous heat flux. This will be explored further in Chapter *[insert chapter 3 here]*.

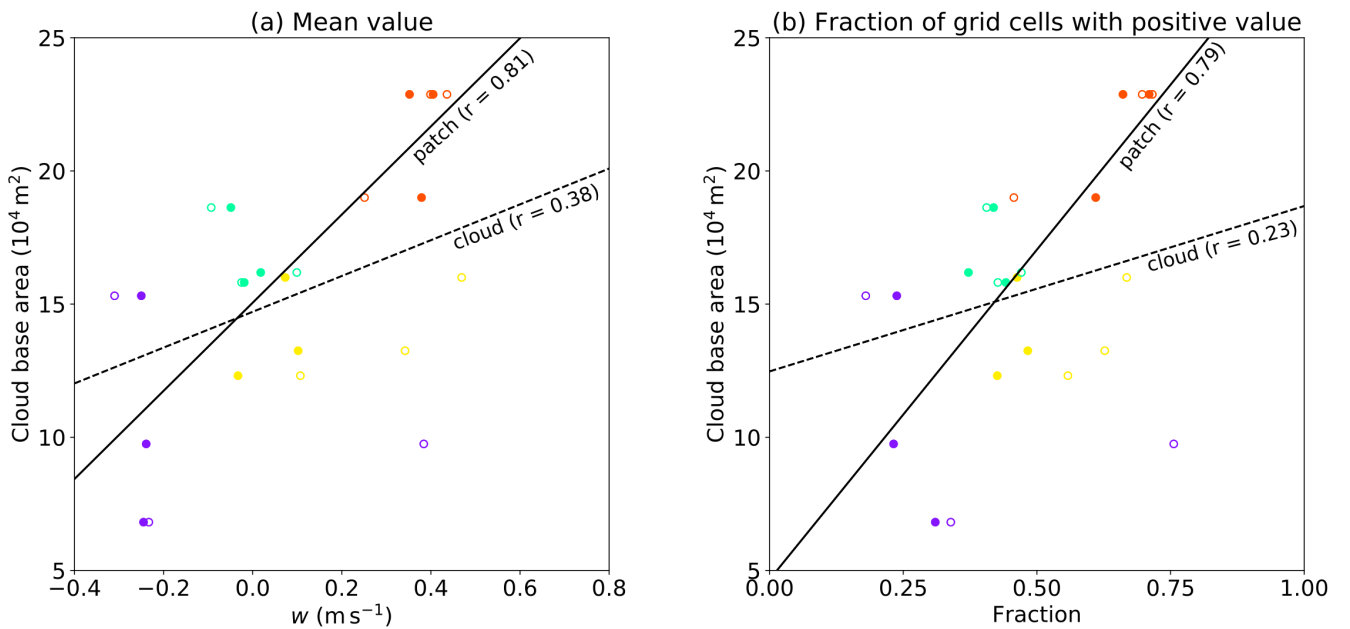


Figure 1.38: Scatterplots of (a) \bar{w}_{250} and (b) fraction of grid cells with positive \bar{w}_{250} , both calculated at $t = 60$ minutes, against maximum cloud base area attained over the lifetime of each cloud. The boundary layer has been masked both above the circular patches (denoted by filled circles) and underneath the maximum cloud base area of the four clouds (unfilled circles). Linear regressions and corresponding r values are also shown (solid line is for patches, dashed line is for clouds.)

1.2.4 Conclusions

This is currently in note form.

1.3 Above cloud: The effect of convectively-generated gravity waves on cloud initiation and development

1.3.1 Motivation

This is currently in note form.

1.3.2 Visualisation of gravity waves

The presence of gravity waves can be observed in vertical velocity, potential temperature and height displacement fields. Figures 1.39 and 1.40 show the time evolution of the vertical velocity and height displacement fields at different heights along the line $y = 3000\text{m}$, a transect which cuts through the centres of clouds TL and TR. A tracer with concentration H_T is initialised at the start of the simulation, which scales vertically with domain height; the height displacement (H_D) is then a measure of the vertical displacement from this initial height (H_I). Mathematically,

$$H_D = H_T - H_I. \quad (1.16)$$

Therefore, a positive value of H_D represents air that has been moved from a higher to lower level, and vice versa.

Both sets of Hovmöller diagrams show the presence of wave-like structures, with clouds overlaid in white and outlined in black. Waves begin to form during the spinup period, with a period of roughly 10 minutes, and the amplitude of these waves increases over time. Similar behaviour is observed for other transects along $y = 1000\text{m}$ (clouds BL and BR), $x = 1000\text{m}$ (clouds BL and TL) and $x = 3000\text{m}$ (clouds BR and TR). The waves initially form close to the level of cloud base, and propagate horizontally.

Vertical Hovmöller diagrams of vertical velocity and height displacement, through the centre of each circular patch, additionally reveal that these waves propagate vertically over time. An example of the vertical velocity field is shown in Figure 1.41, which demonstrates how the amplitude and vertical propagation of the waves increases with time. Interference in the wave pattern appears to develop after the introduction of the circular patches at 60 minutes, and is particularly noticeable in Figure (b), starting around $z = 1500\text{m}$ and rising with height. The wave interference is likely caused by the interaction between the existing wave field and convectively-generated waves emanating from the main cloud. The wave interference is explored further later in this chapter.

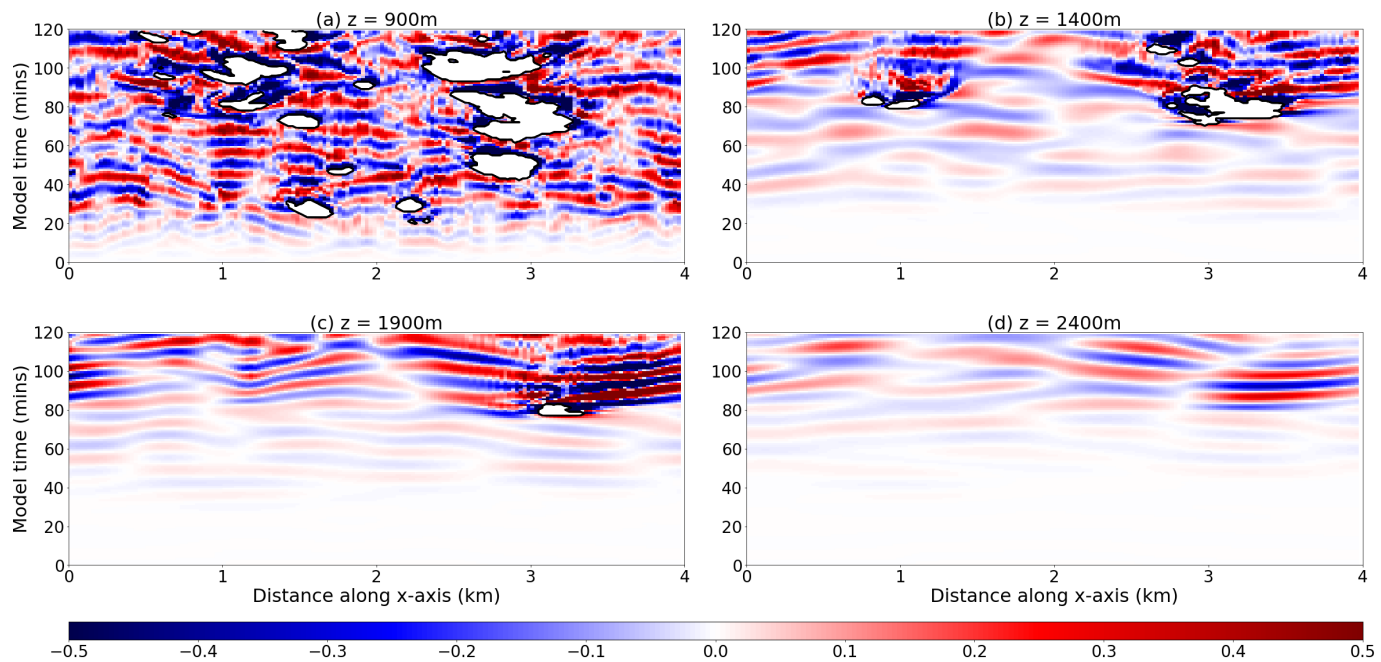


Figure 1.39: Hovmöller diagrams of vertical velocity (in $m s^{-1}$) along the transect $y = 3000m$, shown at (a) $z = 900m$, (b) $z = 1400m$, (c) $z = 1900m$ and (d) $z = 2400m$. Clouds are shown as white areas with black outlines.

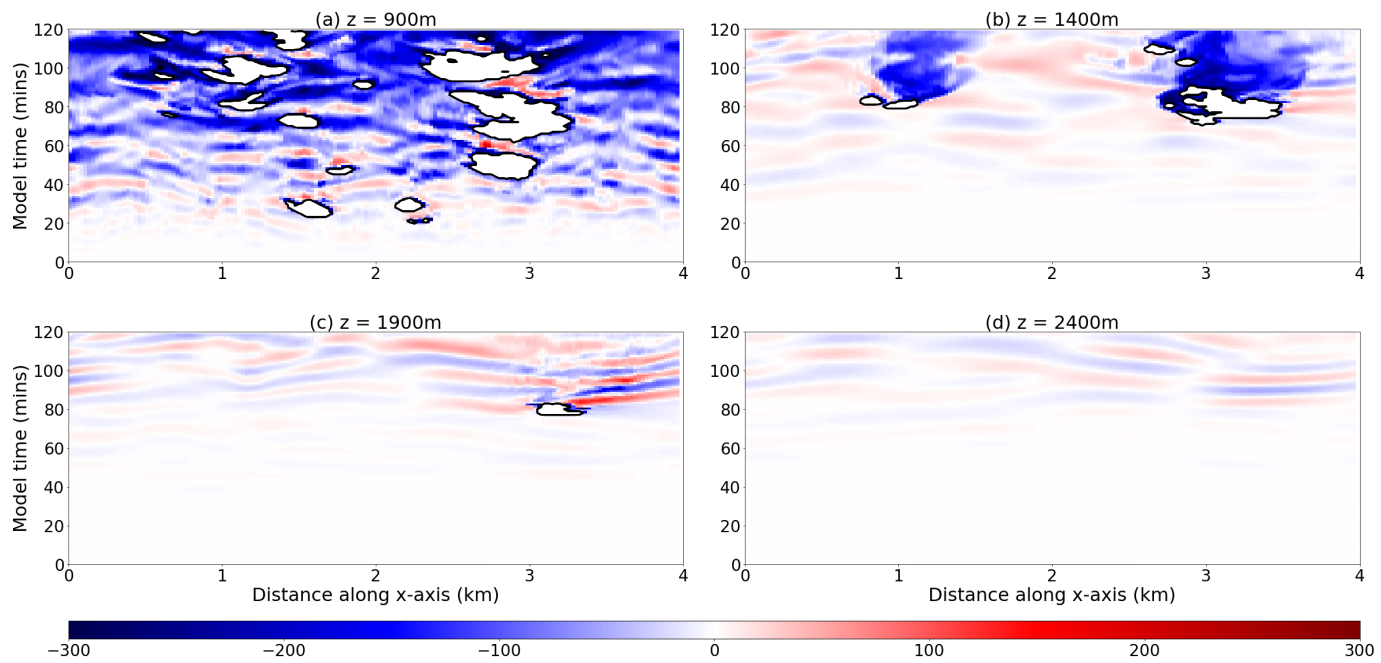


Figure 1.40: Hovmöller diagrams of height displacement (in m) along the transect $y = 3000m$, shown at (a) $z = 900m$, (b) $z = 1400m$, (c) $z = 1900m$ and (d) $z = 2400m$. Clouds are the white areas outlined in black.

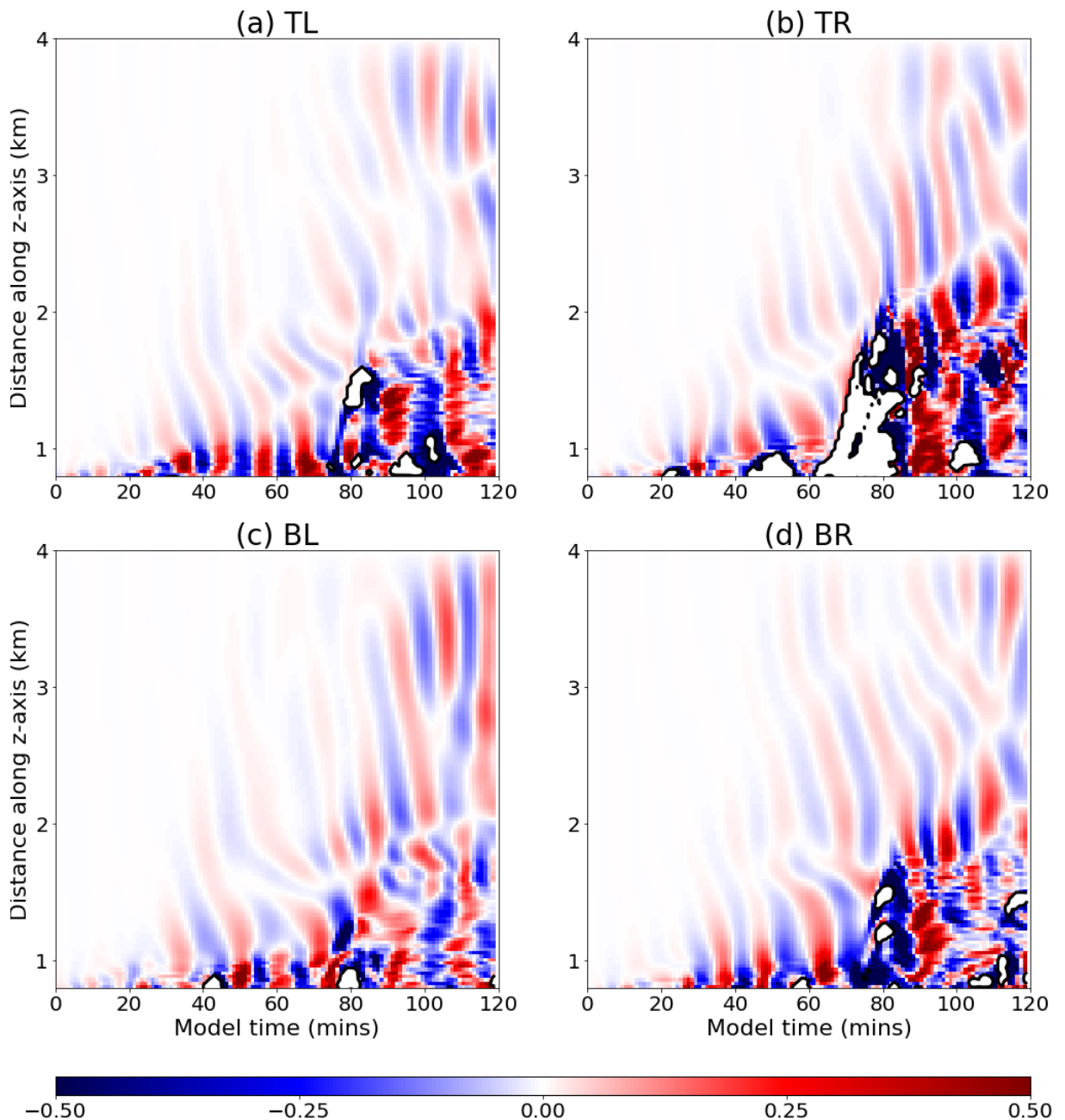


Figure 1.41: Hovmöller diagrams of vertical velocity (in m s^{-1}) along a vertical transect through the centre of each circular patch: (a) TL ($x = 1000\text{m}$, $y = 3000\text{m}$), (b) TR ($x = 3000\text{m}$, $y = 3000\text{m}$), (c) BL ($x = 1000\text{m}$, $y = 1000\text{m}$) and (d) BR ($x = 3000\text{m}$, $y = 1000\text{m}$). The wave field is shown in the cloud layer (above $z = 800\text{m}$) only. Clouds are the white areas outlined in black.

1.3.3 Wave period

Internal gravity waves form in statically stable environments. Atmospheric stability can be assessed using profiles of virtual potential temperature θ_v . If θ_v increases, decreases or is constant with height, this represents a stable, unstable or neutral atmosphere respectively.

Figure 1.42 shows the evolution of horizontal-mean θ_v for simulation Multi_REF. The boundary layer is initially statically neutral as a result of the imposed constant profiles of θ and q_v . During model spinup, a shallow unstable layer forms near the surface in response to the sensible heat flux. Due to the additional surface heating, the boundary layer profile in general initially becomes slightly unstable. However, as shallow convection begins to release latent heat, the top of the boundary layer warms and becomes statically stable over time. Why does the rest of the boundary layer stay mostly neutral?

I think also the circulations pull down stable warmer air from above the boundary layer.

The atmosphere above the boundary layer remains statically stable throughout the simulation, which means that internal gravity waves may exist at all times and are most likely to manifest in this region. Virtual potential temperature continues to decrease up to the top of the model domain at 4000m.

Seems to be, get heating at top and warm air from above dragged down, and the middle bit of the profile stays the same. eventually it gets well mixed and the profile becomes closer to homogeneous again, as the whole profile warms.

Figures 1.39 and 1.40 reveal the presence of gravity waves which amplify over time, and suggest a fairly constant wave period of around 10 minutes. The Brunt-Väisälä frequency N is related to the atmospheric stability, and is defined as

$$N = \sqrt{\frac{g}{\theta_v} \frac{\partial \theta_v}{\partial z}} \quad (1.17)$$

in units of rad s^{-1} , where g is gravitational acceleration in m s^{-2} and z is altitude in m. Substituting the mean profile of θ_v in the cloud-free environment into Equation 1.17, the corresponding profile of internal buoyancy wave frequency is shown in Figure 1.43(a). Using the relation between wave period P and frequency F ,

$$P = \frac{1}{2\pi F}, \quad (1.18)$$

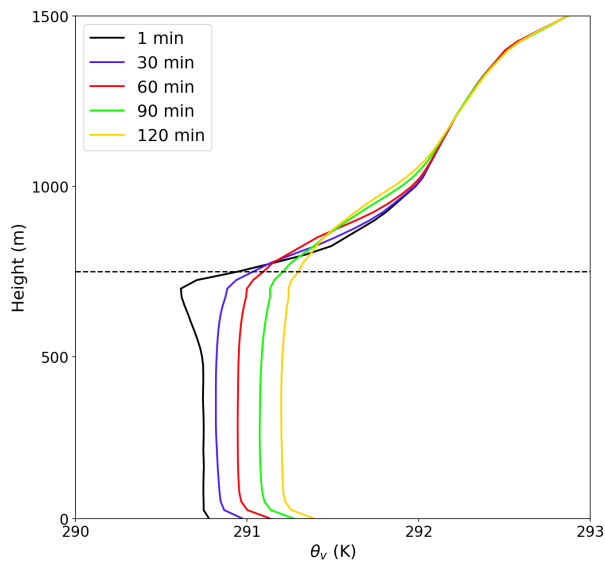


Figure 1.42: Domain-mean virtual potential temperature. The black dashed line denotes the boundary layer top at 750m.

the corresponding wave period is shown in Figure 1.43(b), which shows the possible range of wave periods in the cloud layer is between 7-20 minutes.

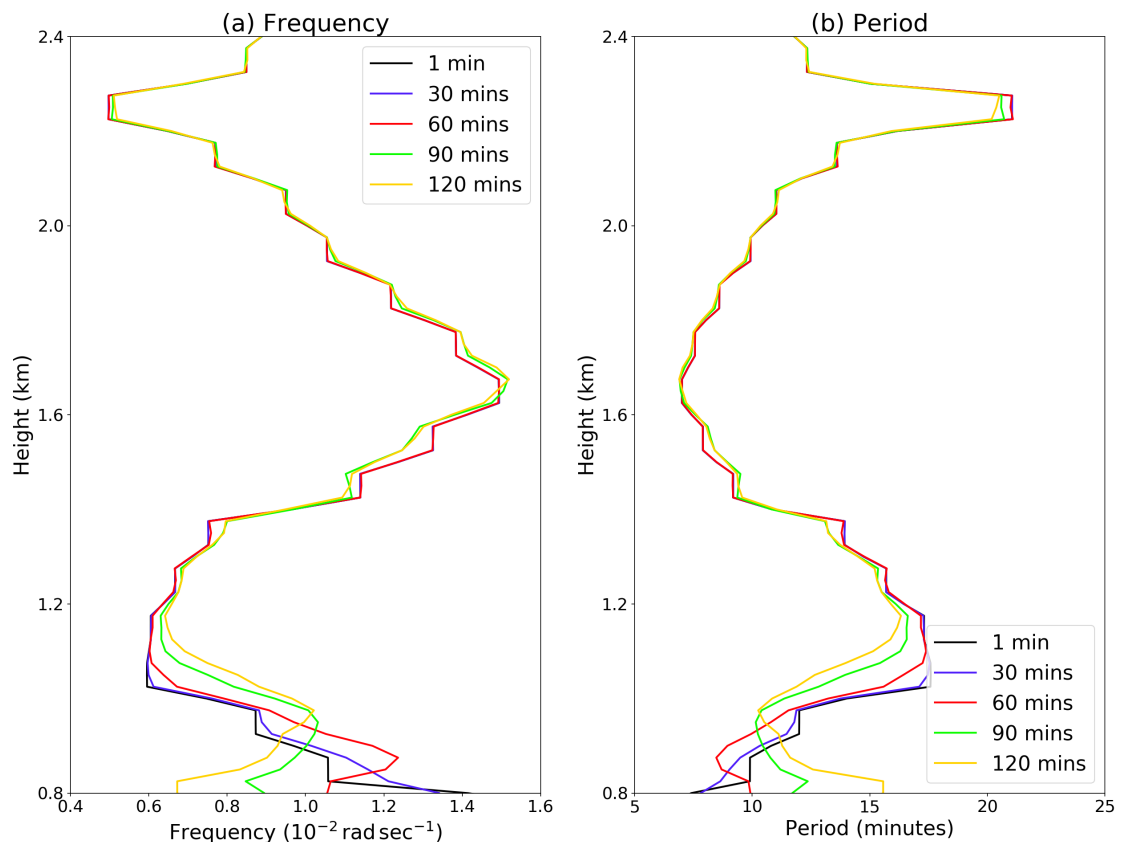


Figure 1.43: Evolution of internal gravity wave properties in ambient air: (a) is wave frequency in $10^{-2} \text{ rad sec}^{-1}$ and (b) is wave period in minutes.

1.3.4 Convectively generated waves

The gravity waves in Figures 1.39(b) and (c) appear to increase in intensity not only with time, but also as a ripple outwards from clouds TL and TR. In order to disentangle the frequencies of the various waves in the domain, a 2-dimensional Fourier transform is applied to cross sections of vertical velocity data at each timestep. Since MONC has periodic boundaries in the x and y directions, the Fourier transform is applied to horizontal rather than vertical cross sections, along the transect $z = 1000\text{m}$.

A Gaussian filter $G(x,y)$ is applied to the filtered vertical velocity fields at each timestep, in order to smooth the data and filter different wavelengths:

$$G(x, y) = e^{-\left(\frac{\hat{x}^2 + \hat{y}^2}{2\sigma^2}\right)} \quad (1.19)$$

Here, \hat{x} and \hat{y} are the distances from the centres of the x and y planes respectively, and the standard deviation of the Gaussian distribution $\sigma = 30$. Once the transformed data has been smoothed, the transform is reversed, and the real part of the solution is shown in Figure 1.44(a). The remainder of the original vertical velocity field is shown in panel (b) as noise, and confirms the presence of convectively-generated waves, as evidenced by the higher amplitude waves primarily emanating from clouds TL and TR.

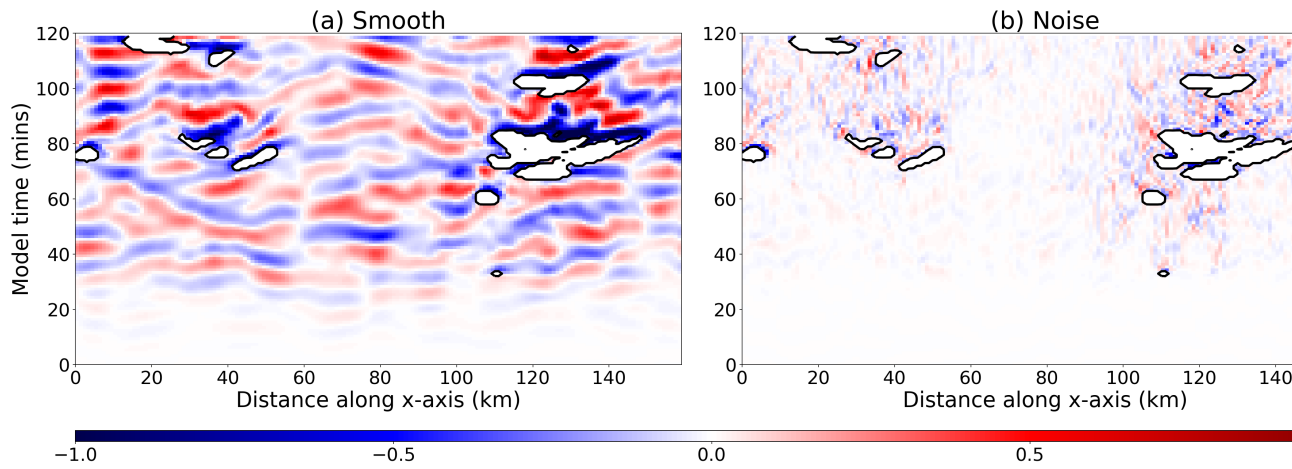


Figure 1.44: Hovmöller of the filtered vertical velocity field at $z = 1000\text{m}$, along the transect $y = 3000\text{m}$. A Gaussian filter is used, with $\sigma = 30$. Figure (a) shows the smoothed field, and (b) shows the residual noise. Clouds are the white areas outlined in black.

1.3.5 Gravity wave phase controls on cloud development

Figure 1.45 shows the evolution in cloud base mass flux in simulation Multi_REF. The two most noticeable features are the difference in mass flux between Cloud TR and the other three clouds, as well as the resurgence of Cloud TR after 90 minutes.

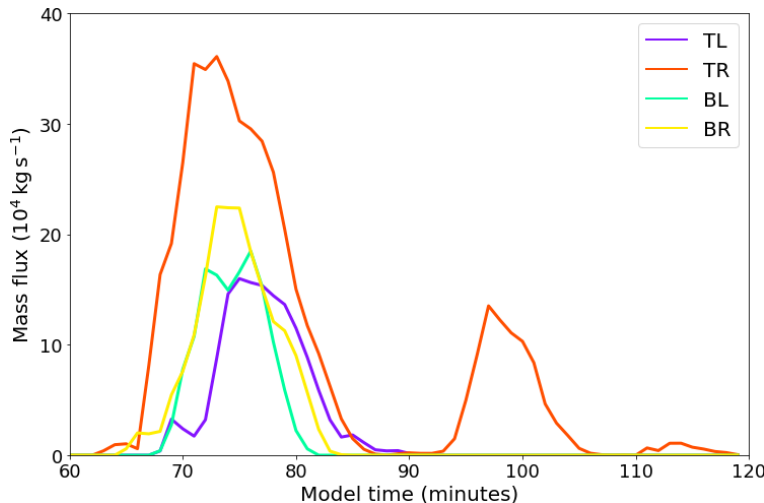


Figure 1.45: Timeseries of cloud base mass flux from the Multi_REF simulation. Clouds TL, TR, BL and BR are shown in purple, red, green and yellow respectively.

The previous chapter explored the relationship between pre-existing boundary layer conditions and cloud development, and suggested that small, localised variations in boundary layer properties can affect the mass flux profile via changes to cloud base area and the energetic properties of parcels entering cloud base. The regeneration of cloud TR is surprising, as the large-amplitude surface forcing is switched off after 70 minutes, and the comparatively shallow surface forcing does not result in the regeneration of the other three clouds. A possible mechanism for regeneration is the coupling of a weak updraft with a pre-existing gravity wave. Lane and Zhang (2011) found that the interaction of a convective cloud with the positive phase of a gravity wave may result in renewed convective activity.

The effect of gravity wave phase on convective cloud development is explored through shifting the timing of the circular patches. Figure 1.43 demonstrated that the period of typical gravity waves in Multi_REF is approximately 7-20 minutes. Therefore if the timing of the circular patches is brought forward or back by five minutes (as demonstrated in simulations Multi_+5 and Multi_-5), a rising thermal is likely to encounter markedly different wave phases. The benefit of shifting the patches by such a small time period is that atmospheric conditions

should not change significantly over this timescale. To confirm this, an additional simulation Multi_nopatch is run. The setup of Multi_nopatch is identical to Multi_REF, except that the four circular patches are not included; instead, the sensible heat flux of 50 Wm^{-2} is applied for the duration of the model run. Figure 1.46 demonstrates that the horizontally-averaged thermodynamic profiles do not vary significantly between 55 and 65 minutes.

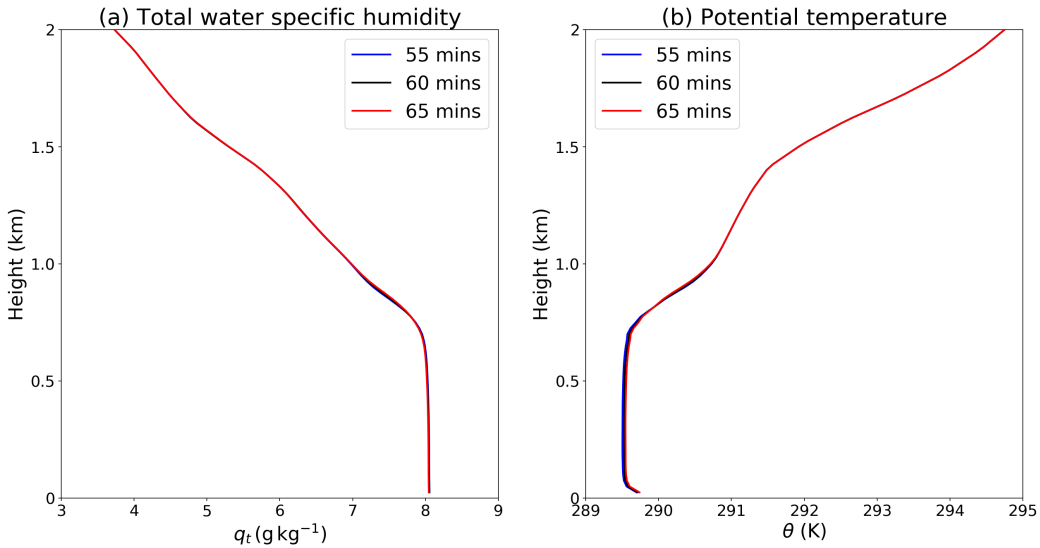


Figure 1.46: Mean profiles up to 2km of (a) total water specific humidity and (b) potential temperature at 55 (blue), 60 (black) and 65 (red) minutes, from the Multi_nopatch simulation.

Figure 1.47 shows the results of the time-shifted circular patches on cloud base mass flux. The x-axis is shifted by plus or minus five minutes in the Multi_+5 and Multi_-5 simulations to allow a direct cloud comparison.

For Cloud TR, the relative timing of initiation is similar between the three simulations. In contrast, clouds TL, BL and BR exhibit significant differences in the timing of initiation as the timing of the circular patches is shifted. For example, the initiation of Cloud TL varies up to around 10 minutes, and Cloud BL in the Multi_-5 simulation actually initiates before the circular patches are introduced, forming on the back of a pre-existing shallow cumulus cloud. There is also notable variety in the development of clouds, both in terms of the mass flux peak and the pattern of evolution. For example, in Multi_REF, Cloud BL exhibits a broadly singular mass flux peak before decaying; however both the shifted flux simulations result in a cloud that initially decays before reforming at a later time. Similarly, both shifted flux simulations result in a Cloud TR that does not experience a regeneration after 90 minutes. This may indicate that

both the initial and secondary peaks in the mass flux profile are influenced by the phase of internal gravity waves.

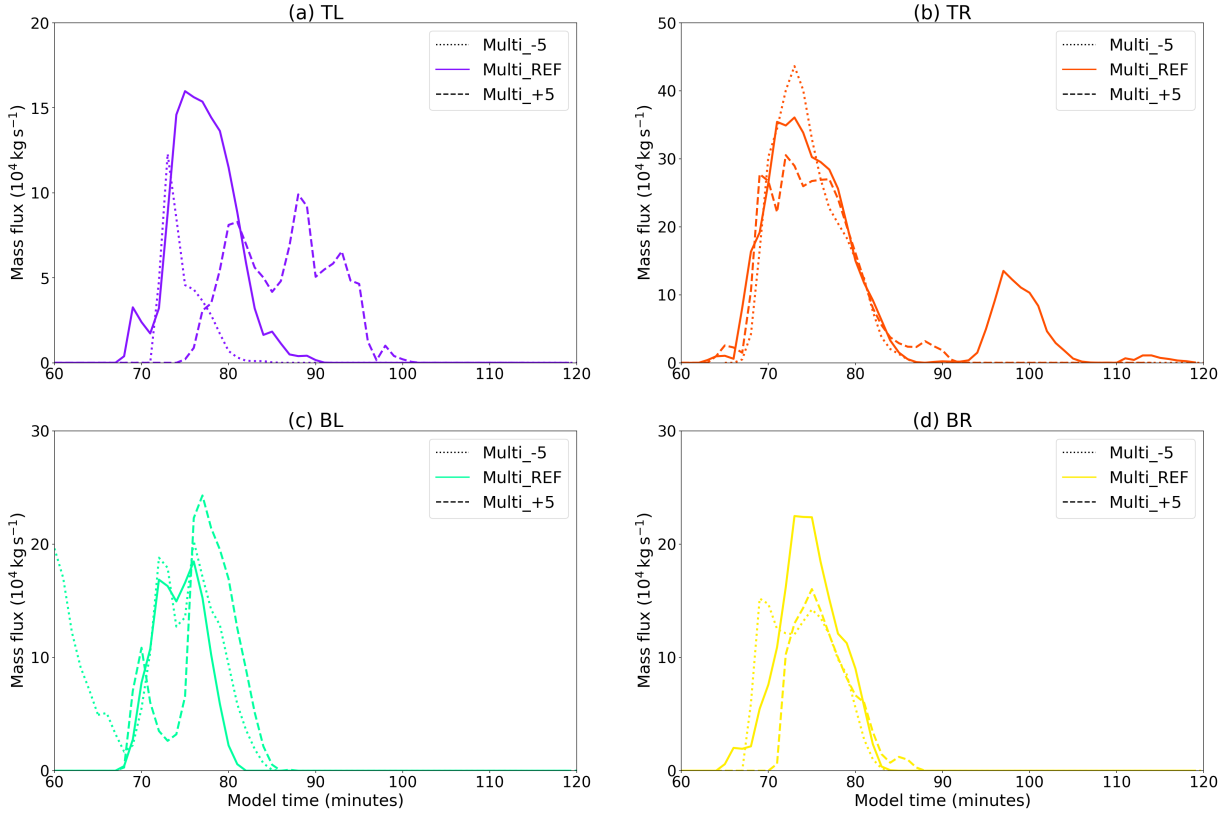


Figure 1.47: Evolution of cloud base mass flux for the four main clouds: (a) TL, (b) TR, (c) BL and (d) BR. The solid lines are for Multi_REF, the thick dashed lines are for Multi_+5 and the thinner dashed lines are for Multi_-5. The x-axis is shifted by plus or minus five minutes for the latter two simulations respectively. Note the different y-axes for each plot.

If we look at cloud tr only, i suppose you could argue that maybe the reason you odn't see regeneration is because the localised thermodynamics in the boundary layer are just right? but also ther eis no big updraft coinciding here. There are shallow updrafts though. Look a tthe secondary mass flux peak - is it still much greater than those you'd see of a shallow cumulus clouds? Could it just be that?

The initiation of Cloud TR does not vary much between the three simulations, but a noticeable difference is the lack of cloud resurgence in both Multi_+5 and Multi_-5. The average thermodynamic profiles at 90 minutes (95 and 85 in Multi_+5 and Multi_-5 respectively) in this quadrant do not vary much between each simulation, as shown in Figure 1.48, which implies that the thermodynamics do not explain the likelihood of cloud resurgence. Instead it is more probable that the phase of the existing gravity waves influence the regeneration of Cloud TR.

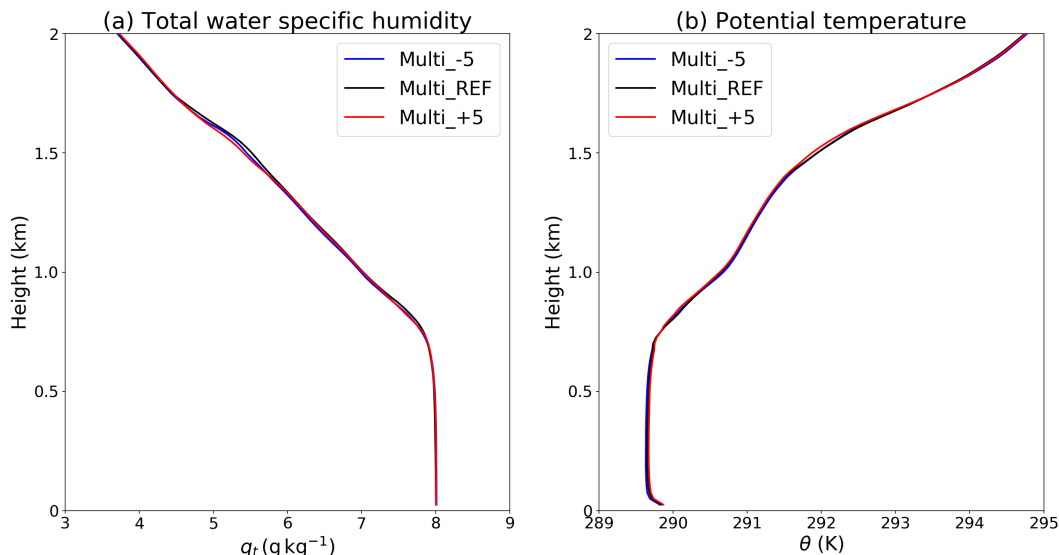


Figure 1.48: Mean profiles in quadrant TR up to 2km of (a) total water specific humidity and (b) potential temperature from Multi_-5 (blue), Multi_REF (black) and Multi_+5 (red) at 85, 90 and 95 minutes respectively.

Current theories, to prove later:

- Coincidence of preferential convective properties with the phase of a gravity wave can affect both the timing of initiation and the strength of resulting convection
- Further resurgence of a cloud is also affected by the coincidence of a gravity wave peak

Gravity wave interactions between multiple clouds

The results from Multi_-5 and Multi_+5 showed that varying the timing of all the circular patches by a small amount resulted in varied differences in cloud initiation and development. This next section explores the role of interactions between gravity waves from the four clouds in cloud initiation and development.

Four additional simulations are ran, in which the timing of a single circular patch is given a five minute headstart. These are:

- Multi_TL
- Multi_TR
- Multi_BL
- Multi_BR

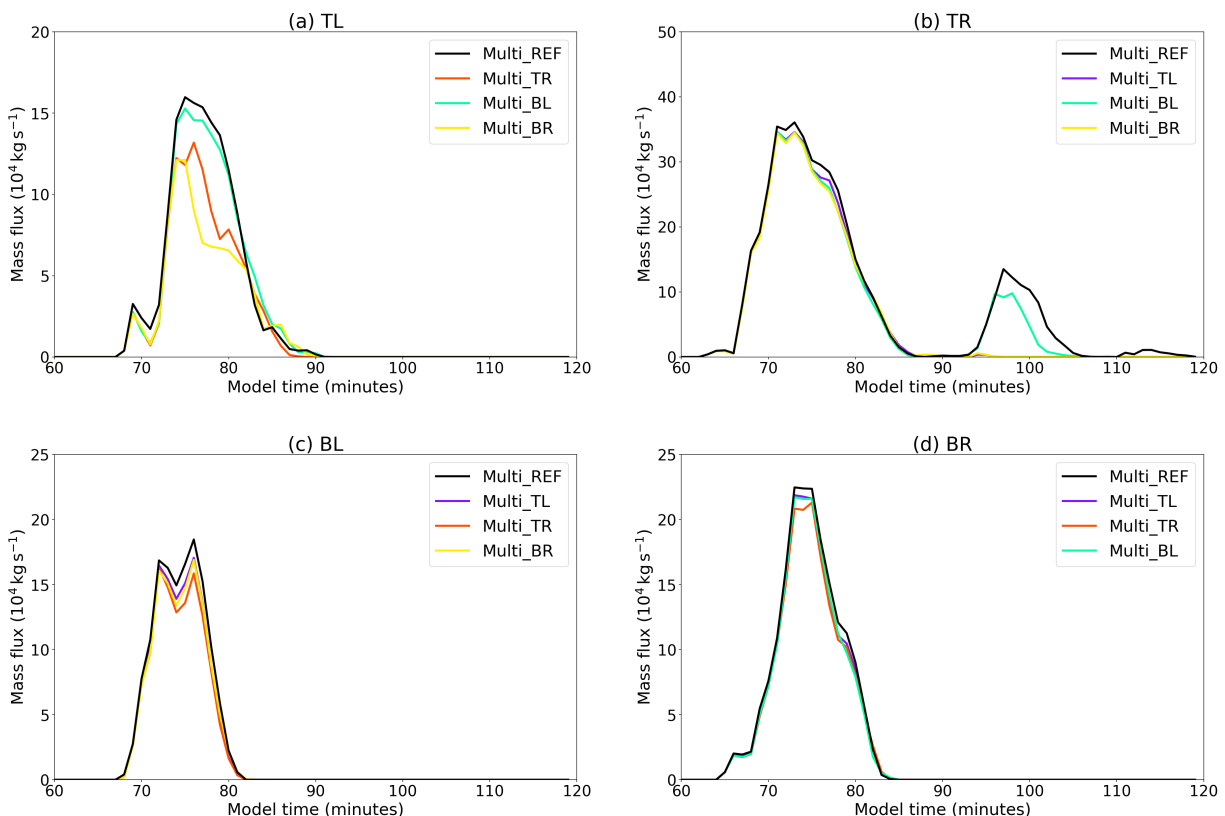


Figure 1.49: Evolution of cloud base mass flux for clouds (a) TL, (b) TR, (c) BL and (d) BR. The black solid lines show the result from Multi_REF. The coloured solid lines show the result when one of the other circular patches is given a headstart. Note the different y-axes for each plot.

THIS IS ALL IN NOTE FORM

Giving a single cloud a headstart - what effect does it have on other clouds? Giving a single cloud a headstart seems to generally dampen the other three clouds, by lowering the mass flux. Not always by a lot, but the most noticeable dampening occurs when TR is given a headstart. Is this because the gravity waves from this larger cloud are more likely to interfere with the development of the others? The clouds generally seem to form in the same way - initialise at the same time, and follow a similar evolution curve, they just don't seem to quite hit the peak. However, the pattern is quite different for Cloud TL - TL seems to be quite a bit more sensitive to headstart in TR or BR. Not so much for BL given a headstart - perhaps the gravity wave interference doesn't reach TL as fast?

When BR and TL are given a headstart, we no longer see the resurgence in TR. These two clouds are closest, so perhaps their waves meet TR earlier. Perhaps also their waves are stronger, so the wave interference is stronger? Perhaps the waves from BL are in a similar phase to TR, aiding the updraft and resurgence.

What can I look into in more detail? panel (a) seems the most sensible to focus on in terms of dampening effect, and panel (b) the most sensible to look at regeneration effect.

I think that initialising a single cloud leads to a damped effect on the other clouds because 1) the waves travel further and interfere? Maybe they change the thermodynamic conditions at cloud base of TL? Would the gravity wave from TR really reach the sphere of influence of TL in 5 minutes though? test this with the TR headstart case. Look at hovmollers - do the convectively generated gravity waves spread out further?

ooh, look at case where we ONLY initialise Cloud TR. do the waves make it into the TL quadrant?p

Four clouds generate more environmental subsidence (irregardless of cloud shell) than one does. Perhaps the subsidence is generated in the form of gravity waves? Environmental thermodynamics are similar.

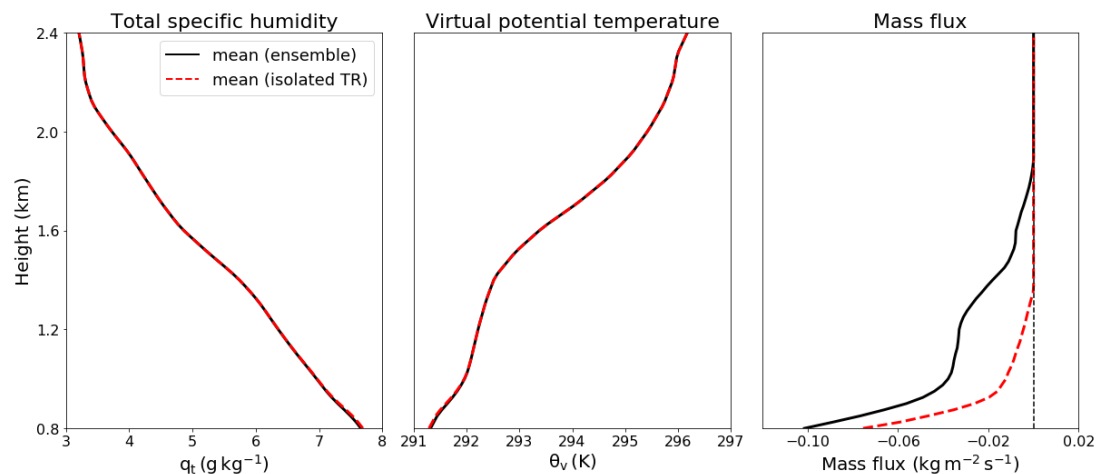


Figure 1.50: ...

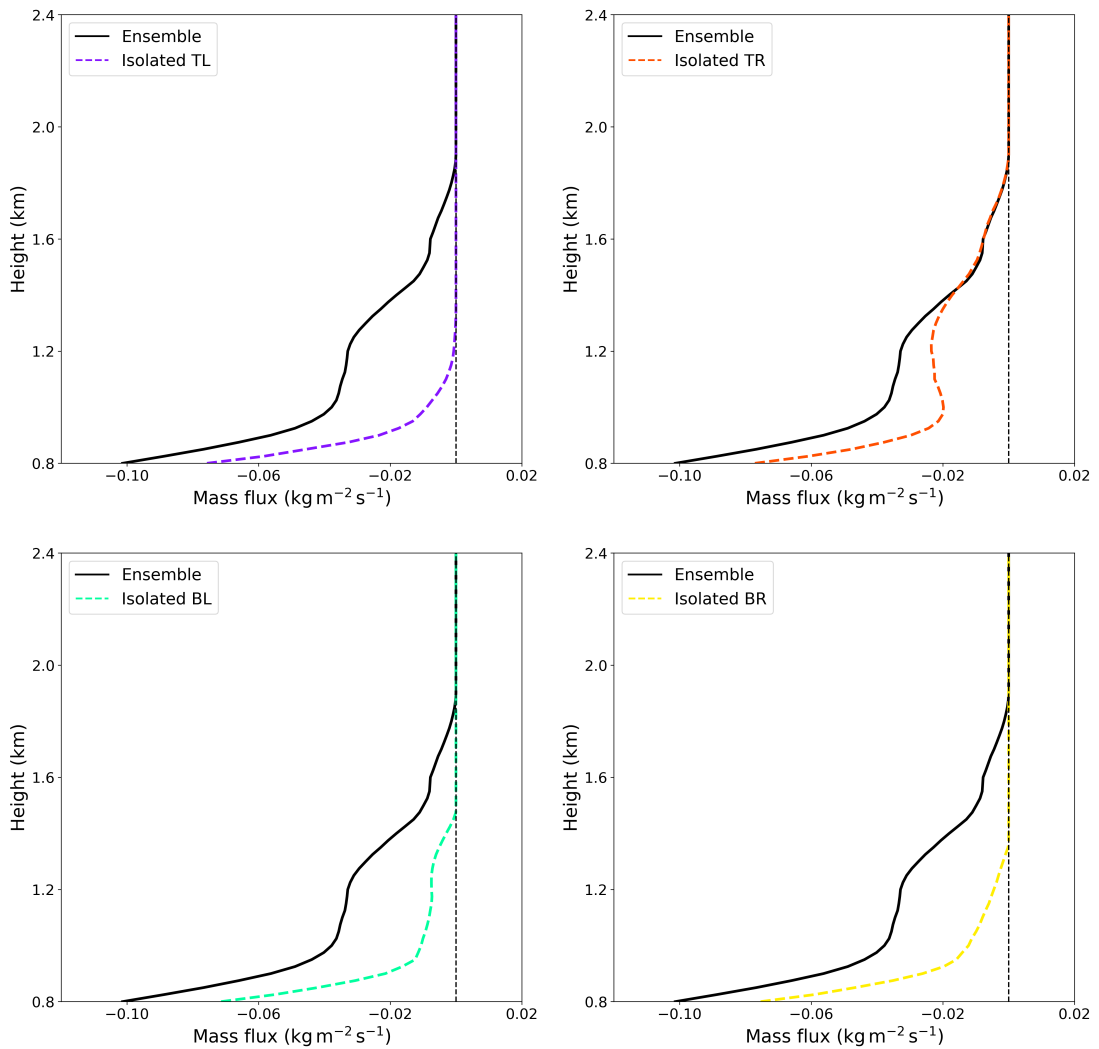


Figure 1.51: ...

1.3.6 Further analysis using idealised LES simulations

Theory is that the coincidence of a thermal with the phase of a gravity waves affects its development. We can test this using warm bubble, one in the centre of the domain, and initialising extra bubbles at different radii/phases of gravity wave from it. Need to make sure there is no thermodynamical mixing (using tracers)

Want to include work that looks at vertical hovmöllers, and shows that by shifting the fluxes, we can get wave interference which may influence cloud development. This is more looking at the mechanisms by which gravity wave affect cloud development. What about cloud initiation?

1.3.7 Discussion

Summary

Bibliography

- Böing, S. J., Jonker, H. J., Nawara, W. A., and Siebesma, A. P. (2014). On the deceiving aspects of mixing diagrams of deep cumulus convection. *Journal of the Atmospheric Sciences*, 71(1):56–68.
- Böing, S. J., Jonker, H. J., Siebesma, A. P., and Grabowski, W. W. (2012). Influence of the subcloud layer on the development of a deep convective ensemble. *Journal of the Atmospheric Sciences*, 69(9):2682–2698.
- Couvreux, F., Guichard, F., Redelsperger, J.-L., Kiemle, C., Masson, V., Lafore, J.-P., and Flamant, C. (2005). Water-vapour variability within a convective boundary-layer assessed by large-eddy simulations and ihop_2002 observations. *Quarterly Journal of the Royal Meteorological Society: A journal of the atmospheric sciences, applied meteorology and physical oceanography*, 131(611):2665–2693.
- Couvreux, F., Hourdin, F., and Rio, C. (2010). Resolved versus parametrized boundary-layer plumes. part i: A parametrization-oriented conditional sampling in large-eddy simulations. *Boundary-layer Meteorology*, 134(3):441–458.
- Dawe, J. and Austin, P. (2012). Statistical analysis of an les shallow cumulus cloud ensemble using a cloud tracking algorithm. *Atmospheric Chemistry and Physics*, 12(2):1101–1119.
- De Rooy, W. C., Bechtold, P., Fröhlich, K., Hohenegger, C., Jonker, H., Mironov, D., Siebesma, A. P., Teixeira, J., and Yano, J.-I. (2013). Entrainment and detrainment in cumulus convection: An overview. *Quarterly Journal of the Royal Meteorological Society*, 139(670):1–19.
- Grabowski, W., Bechtold, P., Cheng, A., Forbes, R., Halliwell, C., Khairoutdinov, M., Lang, S., Nasuno, T., Petch, J., Tao, W.-K., et al. (2006). Daytime convective development over land: A model intercomparison based on lba observations. *Quarterly Journal of the Royal Meteorological Society: A journal*

- of the atmospheric sciences, applied meteorology and physical oceanography*, 132(615):317–344.
- Heus, T., Jonker, H. J., Van den Akker, H. E., Griffith, E. J., Koutek, M., and Post, F. H. (2009). A statistical approach to the life cycle analysis of cumulus clouds selected in a virtual reality environment. *Journal of Geophysical Research: Atmospheres*, 114(D6).
- Heus, T. and Seifert, A. (2013). Automated tracking of shallow cumulus clouds in large domain, long duration large eddy simulations. *Geoscientific Model Development*, 6(4):1261.
- Heus, T., Van Dijk, G., Jonker, H. J., and Van den Akker, H. E. (2008). Mixing in shallow cumulus clouds studied by lagrangian particle tracking. *Journal of the Atmospheric Sciences*, 65(8):2581–2597.
- Hirsch, E., Koren, I., Altaratz, O., Levin, Z., and Agassi, E. (2017). Enhanced humidity pockets originating in the mid boundary layer as a mechanism of cloud formation below the lifting condensation level. *Environmental Research Letters*, 12(2):024020.
- Jiang, H., Xue, H., Teller, A., Feingold, G., and Levin, Z. (2006). Aerosol effects on the lifetime of shallow cumulus. *Geophysical Research Letters*, 33(14).
- Kang, S.-L. and Bryan, G. H. (2011). A large-eddy simulation study of moist convection initiation over heterogeneous surface fluxes. *Monthly weather review*, 139(9):2901–2917.
- Lane, T. P. and Zhang, F. (2011). Coupling between gravity waves and tropical convection at mesoscales. *Journal of the atmospheric sciences*, 68(11):2582–2598.
- Miltenberger, A. K., Field, P. R., Hill, A. A., Rosenberg, P., Shipway, B. J., Wilkinson, J. M., Scovell, R., and Blyth, A. M. (2018). Aerosol–cloud interactions in mixed-phase convective clouds—part 1: Aerosol perturbations. *Atmospheric Chemistry and Physics*, 18(5):3119–3145.
- Morrison, H. (2016). Impacts of updraft size and dimensionality on the perturbation pressure and vertical velocity in cumulus convection. part i: Simple, generalized analytic solutions. *Journal of the Atmospheric Sciences*, 73(4):1441–1454.

- Neggers, R., Siebesma, A., and Jonker, H. (2002). A multiparcel model for shallow cumulus convection. *Journal of the Atmospheric Sciences*, 59(10):1655–1668.
- Patton, E. G., Sullivan, P. P., and Moeng, C.-H. (2005). The influence of idealized heterogeneity on wet and dry planetary boundary layers coupled to the land surface. *Journal of the Atmospheric Sciences*, 62(7):2078–2097.
- Plant, R. et al. (2008). Statistical properties of cloud lifecycles in cloud-resolving models. *Atmospheric Chemistry and Physics Discussions*, 8:20537–20564.
- Rieck, M., Hohenegger, C., and van Heerwaarden, C. C. (2014). The influence of land surface heterogeneities on cloud size development. *Monthly Weather Review*, 142(10):3830–3846.
- Romps, D. M. and Kuang, Z. (2010). Nature versus nurture in shallow convection. *Journal of the Atmospheric Sciences*, 67(5):1655–1666.
- Siebesma, A. P., Bretherton, C. S., Brown, A., Chlond, A., Cuxart, J., Duynkerke, P. G., Jiang, H., Khairoutdinov, M., Lewellen, D., Moeng, C.-H., et al. (2003). A large eddy simulation intercomparison study of shallow cumulus convection. *Journal of the Atmospheric Sciences*, 60(10):1201–1219.
- Stirling, A. and Petch, J. (2004). The impacts of spatial variability on the development of convection. *Quarterly Journal of the Royal Meteorological Society: A journal of the atmospheric sciences, applied meteorology and physical oceanography*, 130(604):3189–3206.
- van Heerwaarden, C. C. and Guerau de Arellano, J. V. (2008). Relative humidity as an indicator for cloud formation over heterogeneous land surfaces. *Journal of the Atmospheric Sciences*, 65(10):3263–3277.
- Zhang, Y. and Klein, S. A. (2010). Mechanisms affecting the transition from shallow to deep convection over land: Inferences from observations of the diurnal cycle collected at the arm southern great plains site. *Journal of the Atmospheric Sciences*, 67(9):2943–2959.
- Zhao, M. and Austin, P. H. (2005). Life cycle of numerically simulated shallow cumulus clouds. part i: Transport. *Journal of the Atmospheric Sciences*, 62(5):1269–1290.